Ultrahigh Resolution Optical Coherence Tomography for Non-invasive Imaging of Outer Retina Degeneration in Rat Retina

by

Sepideh Hariri

A thesis
presented to the University of Waterloo
in fulfillment of the
thesis requirement for the degree of
Doctor of Philosophy
in
Physics

Waterloo, Ontario, Canada, 2013

AUTHOR'S DECLARATION

I hereby declare that I am the sole author of this thesis except where explicitly noted. This is a true copy of the thesis, including any required final revisions, as accepted by my examiners.

I understand that my thesis may be made electronically available to the public.

Abstract

This project initiated with the aim for improving the ultrahigh resolution optical coherence tomography (UHR-OCT) system performance by considering the limitations to the axial OCT resolution for *in vivo* imaging of human and animal retina. To this end, a computational model was developed to simulate the effect of wavelength-dependant water absorption on the detected spectral shape of the broad-bandwidth light source used in UHR-OCT at 1060nm wavelength region, which effectively determines the axial OCT resolution in the retina. For experimental verification of the computational model, a custom built light source with a re-shaped spectrum (Superlum Inc.) was interfaced to the state-of-the-art UHR-OCT system. About 30% improvement of the axial OCT resolution in the rat retina and ~12% improvement of the axial OCT resolution in the human retina was achieved compared to the case of the almost Gaussian shaped spectrum of the standard, commercially available SLD. Although water absorption in the 1060nm spectral region strongly affects the sample beam, selecting a suitable light source with specific spectral shape can compensate for the undesired water absorption effect and thus result in significantly improved axial resolution in *in vivo* OCT retinal images.

To demonstrate the advantages of the state-of-the-art OCT technology for non invasive retinal imaging, an established animal model of outer retina degeneration (sodium iodate ($NaIO_3$)-induced retina degeneration) was employed for longitudinal monitoring of the degeneration and investigation of possible early and dynamic signs of damage undetected by other imaging modalities.

The long-term (up to 3 months) and short-term (up to 12 hours) effect of sodium iodate toxicity on the layered structure of retina was monitored longitudinally and *in vivo* for the first time using OCT. An initial acute swelling of the retina, followed by progressive disruption and degeneration of outer retina was observed as a result of sodium iodate-induced damage. Changes in the thickness and optical reflectivity of individual retinal layers were extracted from the OCT images to quantify the changes occurring at different stages of the disease model.

Results from this project present the theoretical and practical limits to the highest axial OCT resolution achievable for retina imaging in the 1060nm spectral range both in small animals and

humans, and provided a framework for future development of novel light sources. Furthermore, UHR-OCT imaging was shown to be an effective and valuable modality for *in vivo*, non invasive investigation of retina degenerative disease.

Acknowledgements

I would like to sincerely thank

Dr. Kostadinka Bizheva for being a great supervisor and a caring and understanding friend;

My committee members, Dr. Melanie Campbell, Dr. Donna Strickland and Dr. Natalie Hutchings for their continuous support and guidance during my four years of Ph.D studies;

Dr. Rainer Leitgeb for reviewing this work;

Dr. Vivian Choh for her patient guidance in statistical data analysis and histology;

Nancy Gibson and Martin Ryan for their help with animal care and handling;

Harmenn van der Heide and Krunomir Dvorski from the Science Shop for assistance with machining and electronics;

Dr. Shelley Boyd for her helpful suggestions related to the sodium iodate animal model used in this study;

I would specially like to thank Dr. Melanie Campbell for her generous support and her invaluable guidance for improving the overall quality of this thesis.

Co-op students at Biomedical Imaging Lab, David Lee, Eun Sun Song, Patrick Lee, Saad Shakeel and Daryl Chulho Hyun for assistance with imaging and data processing.

The contribution of different co-authors and collaborators are discussed at the beginning of each related chapter.

This work was supported financially and in kind by NSERC, CIHR doctoral fellowship, Ontario Centers of Excellence, University of Waterloo start up grant, Superlum Inc. and Sensors Unlimited Inc.(Goodrich).

Dedication

To my wonderful parents, my heroes, Bahiyeh and Esfandiar, for teaching me the ways of life and supporting me always, in every way possible.

To my beloved husband and best friend, Alireza, for walking with me every step of the way.

To my amazing siblings, Behrouz, Sahar and Behzad, for sharing with me countless joyful moments.

To my lovely friends, for bringing warmth to my heart in challenging times.

Table of Contents

List of Abbreviations

OCT	optical coherence tomography
FWHM	full width at half maximum
TdOCT	time domain OCT
FdOCT	Fourier domain OCT
IFT	inverse Fourier transform
sdOCT	spectral domain OCT
ssOCT	swept source OCT
SNR	signal to noise ratio
PSF	point spread function
UHR-OCT	ultrahigh resolution OCT
AMD	age-related macular degeneration
RPE	retinal pigment epithelium
cSLO	confocal scanning laser ophthalmoscope
FA	fluorescence angiography
FAF	fundus autofluorescence
NA	numerical aperture
AO	adaptive optics
GA	geographic atrophy
CNV	choroidal neovascularization
RP	retinitis pigmentosa
IV	intravenous
CL	collimating lenses
DC	dispersion compensation unit
NDF	neutral density filter
FOI	fiber optic isolator
M	mirror

PC	polarization controllers
SLD	superluminescent diode
TS	translation stage
CL	collimating lens
DG	diffraction grading
FL	focusing lense
FOV	field of view
PBS	phosphate buffered saline
ANOVA	analysis of variance
NFL	nerve fiber layer
GCL	ganglion cell layer
IPL	inner plexiform layer
INL	inner nuclear layer
OPL	outer plexiform layer
ONL	outer nuclear layer
ELM	external limiting membrane
IS	inner segment
OS	outer segment
CC	choriocapillaris
LRL	low reflective layer
PR	photoreceptor
$NaIO_3$	sodium iodate
H&E	hematoxylin and eosin
CCD	charge coupled device
TUNEL	terminal deoxynucleotidyl transferase
ERG	electroretinography

List of Figures

List of Tables

Chapter 1

Introduction and Background

1.1 Overview and Motivation

Optical coherence tomography (OCT) is a novel imaging modality that has brought about revolutionary changes to the field of biomedical imaging and especially in ophthalmology. OCT has made possible unprecedented *in vivo*, non invasive, cross-sectional evaluation of the detailed retinal structure with high precision. Such an evaluation is essential for the better understanding of the mechanisms and dynamic changes in healthy and diseased retina[1].

OCT imaging in the 1060 nm wavelength region has recently gained popularity for ophthalmic applications due to its multiple advantages as compared to OCT retinal imaging at shorter wavelengths (800 nm). The high axial resolution of ophthalmic UHR-OCT systems designed for retinal imaging is a key factor for visualization of small morphological details in the human or animal retina, which can serve as diagnostic or therapeutic markers for many retinal diseases.

This project investigates the effectiveness of spectral shaping as a method for improving the axial resolution in the retina for UHR-OCT systems designed for the 1060 nm wavelength region. Subsequently, the high speed UHR-OCT system with improved axial resolution was used to investigate *in vivo*, outer retina degeneration in the rodent retina, induced by administration of sodium iodate in rats.

This thesis is organized in a paper-based format. However, since the same UHR-OCT system, imaging procedure and data analysis were used in all studies, a separate chapter is dedicated to describing methods in order to avoid repetition. Likewise, the paper introduction materials which were already covered more extensively in the literature review chapter in this thesis, were omitted for the reader's convenience. The co-author contributions are discussed at the opening of each chapter.

The thesis chapters are organized as follows:

- Chapter 1 introduces the OCT fundamental concepts and applications for retina imaging. Other methods for *in vivo* retina imaging are briefly introduced.
- Chapter 2 presents a literature review of outer retina degeneration with an in-depth focus on the sodium iodate-induced animal model used in this project.
- Chapter 3 describes the UHR-OCT system, imaging probe, calculations and procedures used to generate the results described in the subsequent chapters.
- Chapter 4 describes a theoretical model and the experimental verification of a novel approach based on spectral shaping, for improving the OCT axial resolution for *in vivo* retinal imaging in the 1060 nm wavelength region.
- Chapters 5 and 6 present the long-term and the short-term effects of sodium iodate on the rat retina. Changes of the structure and optical properties of the retina layers were observed *in vivo* and quantified for the case of sodium iodate-induced outer retina degeneration in rats.
- The overall discussion and conclusion of the thesis follows next.
- Appendix A is a manuscript that demonstrates experimentally the improvement of the OCT axial resolution in healthy human retina, by utilizing the spectral shaping approach.
- Appendix B contains the journal and co-author permissions for reproduction of the material used in this thesis.

1.2 Optical Coherence Tomography (OCT)

1.2.1 OCT Fundamentals of Operation

OCT is a relatively new imaging technology that enables *in vivo*, non invasive, high resolution cross-sectional imaging of biological tissue[1]. It's principle of operation is based on low coherence interferometry where the magnitude and the echo time delay of backscattered light are measured[2]–[4]. In a Michelson-type interferometer, the imaging beam is divided into a sample and a reference beam with a beam splitter [Fig.1.1]. The sample beam is directed to the imaged object while the reference beam reflects off a mirror. The back-scattered/back-reflected light from both arms are superimposed as they pass through the beam splitter and produce an interference pattern from which a one-dimensional OCT image is generated (an A-scan, which represents the depth-dependent reflectivity profile of the imaged object).

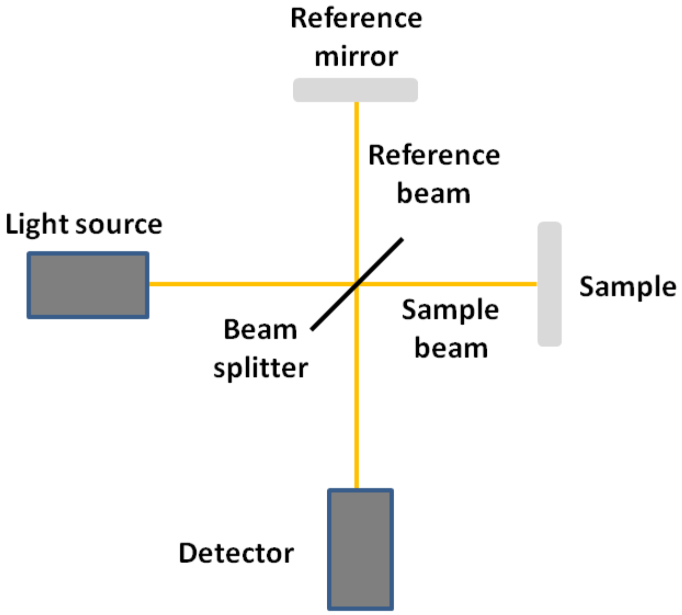

Figure 1.1: schematic diagram of a typical interferometer.

The interference pattern is observed only if the path length difference between the sample and reference arms (ΔL) is within the coherence length of the light source. The coherence length, l_c, is inversely proportional to the spectral bandwidth, Δk, of the light source. Therefore, for a highly coherent source (narrow spectral bandwidth), interference occurs over large range of path length differences. In contrast, a low coherent light (broad spectral bandwidth) source yields interference fringes only for short ΔL and is applied in OCT to gain information from a short axial length within the sample.

The electric field of the interference signal is a vector sum of the back-reflected reference (E_R) and sample (E_S) fields:

$$E_{Detector} = E_R + E_S$$

(1.1)

The detector however, measures the intensity of the signal ($I(k)_{Detector}$) which is proportional to the square of the total electric field:

$$I(k)_{Detector} = \frac{\rho}{2}\left(\left|E_R\right|^2 + \left|E_S\right|^2 + 2E_R E_S \cos(2k\Delta L)\right)$$

(1.2)

where k is the wave number, ρ is the detector responsivity and the factor 1/2 indicates the second pass of the sample and reference beams through the 50/50 beamsplitter[1]. As seen in Eq.1.2., the detector signal intensity consists of three terms. The first two terms represent constant values of the back-reflected light intensity from the reference and sample arms respectively. The third term is the desired OCT signal resulting from interference between the back-reflected sample and reference beams. As mentioned before, using the interferometric method allows for measuring the echo time delay of electromagnetic waves. The third term of Eq.1.2 points to another advantage of this technique. The multiplication of E_S by E_R implies that a strong reference signal can be used to amplify a weak sample signal in the case of weekly back-reflecting samples (e.g. biological tissue) hence making very weak signals detectable.

1.2.2 OCT Resolution

The axial resolution of an OCT system is determined by the source coherence length[1]. It is the full width at half maximum (FWHM) of the field autocorrelation function, $\gamma(z)$, which is equivalent to the inverse Fourier transform (IFT) of the power spectrum $S(k)$.

$$S(k) \xrightarrow{IFT} \gamma(z)$$

(1.3)

The spectral bandwidth, Δk, is the FWHM of the power spectrum while the coherence length, l_c, is the FWHM of the autocorrelation function. Fig.1.2 illustrates the relation between these parameters for a Gaussian spectral distribution.

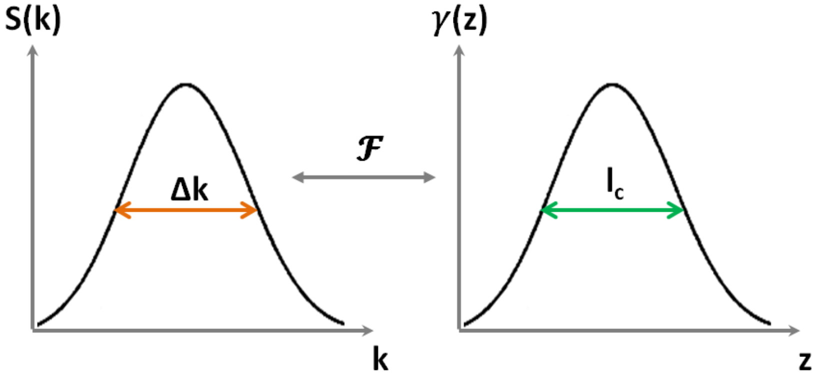

Figure 1.2: A Gaussian power spectrum $S(k)$ and its corresponding autocorrelation function $\gamma(z)$ are related via the Fourier transform. Δk and l_c represent the spectral bandwidth and the coherence length respectively.

In the case of a Gaussian beam, the OCT axial resolution, Δz, in free space is determined by Eq.1.4:

$$\Delta z = l_c = \frac{2\sqrt{\ln(2)}}{\Delta k} = \frac{2\ln(2)}{\pi}\frac{\lambda_0^2}{\Delta\lambda}$$

(1.4)

where Δk and $\Delta\lambda$ are the FWHM of the source spectrum in terms of wavenumber and wavelength respectively while λ_0 is the central wavelength[5]. As seen in Eq.1.4 the OCT axial resolution is inversely proportional to the spectral bandwidth of the light source and therefore, broad bandwidth spectra are required to achieve high axial resolution in OCT images[5].

One very interesting aspect of OCT is that the axial and transverse (lateral) resolutions are independent. OCT transverse resolution (Δx), is the same as in standard optical microscopy. It is defined by the radius of the spot size (Airy disk) of the focused beam on the sample which is inversely proportional to the numerical aperture (NA) of the imaging lens:

$$\Delta x = \frac{4\lambda_0}{\pi}\left(\frac{f}{d}\right) = 0.61\frac{\lambda_0}{NA}$$

(1.5)

where f is the first focal length of the system, d is the beam diameter on the lens and λ_0 is the central wavelength[6]. Hence, using a high NA will result in high transverse resolution. Equation 1.5 calculates the diffraction limited transverse resolution for a Gaussian incident beam and does not account for aberrations.

When the imaging beam propagates through a medium with refractive index higher than 1, the effective wavelength is the wavelength in free space (vacuum) divided by the material refractive index. In this case, the axial resolution is calculated using this effective wavelength.

The OCT transverse resolution is related to the depth of focus or confocal parameter b:

$$b = 2z_{\text{Rayleigh}} = \frac{\pi\Delta x^2}{\lambda_0} = \frac{2\pi\omega_0^2}{\lambda_0}$$

(1.6)

where z_{Rayleigh} is the Rayleigh range and ω_0 is the Gaussian beam waist radius ($\Delta x = \sqrt{2}\omega_0$)[6]. As a result of this dependence, there is a trade-off between high transverse resolution and large depth of focus as shown in Fig.1.3.

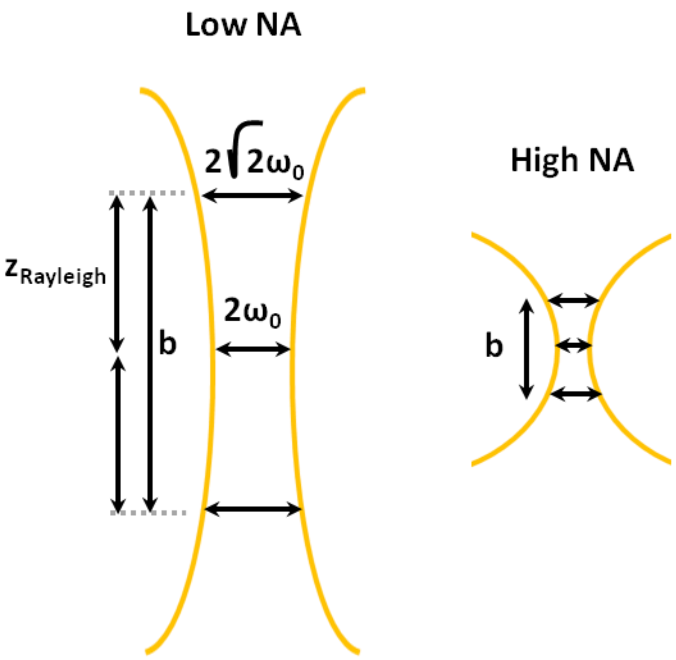

Figure 1.3: Numerical aperture determines the OCT lateral resolution and depth of field. ω_0 is the beam waist radius, b is the depth of field and z_{Rayleigh} is the Rayleigh range.

In order to perform cross sectional OCT imaging a low NA is desirable ($b \gg \Delta z$) to create a uniform and large depth of focus (Eqs.1.5 and 1.6). A high NA would result in a non-uniform spot size and power distribution at different axial locations in the sample hence, negatively affecting the OCT image quality, specifically, the image contrast as a function of depth within the imaged object.

1.2.3 Fourier Domain OCT

In the early designs of OCT systems, information from different depths of the sample was obtained by scanning the reference arm mirror to change the optical path length. An axial scan (A-scan) was then generated by measuring the amount of back-reflected/back-scattered light, originating from various axial positions within the imaged object. This system design is known as Time domain OCT (TdOCT)[7], [8].

An alternative OCT system design is known as Fourier domain OCT (FdOCT)[9]–[11]. In FdOCT the reference mirror is stationary and the interference pattern is measured as a function of wavelength. The broad bandwidth spectrum of the source contains many wavelength components. The interference pattern results from the simultaneous interaction of all the wavelengths in the reference beam reflecting from a single reflector with the sample beam reflecting from different depths within the sample. Hence, information from the sample is encoded in the spectral fringe pattern. In the case of multiple reflectors in the sample arm, the detector signal, $I(k)_{Detector}$, can be written as:

$$I(k)_{Detector} = \frac{\rho}{4}\left[S(k)\left[R_R + \sum_{n=1}^{N} R_{sn}\right]\right] + \frac{\rho}{2}\left[S(k)\sum_{n=1}^{N}\sqrt{R_R R_{sn}}\left(\cos\left[2k\left(z_R - z_{sn}\right)\right]\right)\right] + \frac{\rho}{4}\left[S(k)\sum_{n\neq m=1}^{N}\sqrt{R_{sn}R_{sm}}\left(\cos\left[2k\left(z_{sn} - z_{sm}\right)\right]\right)\right]$$

(1.7)

Where R_R, R_{sn} and R_{sm} are the reflectivity of the reference mirror and the n^th^ and m^th^ sample reflector respectively, k is wavenumber, z_R is the reference arm position and z_{sn} and z_{sm} are the n^th^ and m^th^ sample reflector position yielding path length differences $(z_R - z_{sn})$ and $(z_{sn} - z_{sm})$.

Performing inverse Fourier transform (IFT) on Eq.1.7 and using convolution and sifting property, one can convert the data from the frequency domain to the spatial domain and reconstruct the sample reflectivity profile as a function of depth (A-scan)[1].

$$IFT\left[I(k)_{Detector}\right] = A - scan = i(z)_{Detector} = \frac{\rho}{8}\gamma(z)\left[R_R + \sum_{n=1}^{N} R_{sn}\right]$$

$$+\frac{\rho}{4}\left(\sum_{n=1}^{N}\sqrt{R_R R_{sn}}\left[\gamma\left[2\left(z_R - z_{sn}\right)\right] + \gamma\left[-2\left(z_R - z_{sn}\right)\right]\right]\right)$$

$$+\frac{\rho}{8}\left(\sum_{n\neq m=1}^{N}\sqrt{R_{sn} R_{sm}}\left[\gamma\left[2(z_{sn} - z_{sm})\right] + \gamma\left[-2(z_{sn} - z_{sm})\right]\right]\right)$$

(1.8)

Where $\gamma(z)$, the autocorrelation function, is the IFT of the power spectrum, $S(k)$.

As shown in Eq.1.8 the resulting A-scan is composed of three different terms. The first one is the large artifact DC term at zero path length which is the IFT of the intensity reflected from reference arm plus the sum of the sample reflector signals. If the reference arm power reaching the detector is much higher than that of the sample arm, or in other words the reference reflectivity is much larger that the sample reflectivity ($R_R \gg R_S$) which is true in the case of soft tissue imaging), this artifact can be eliminated by subtracting the background (reference arm signal) from the total signal. The second term is the cross-correlation term which is the result of the interference between the sample and reference signals. This term contains the data we are interested in. The third term is the autocorrelation term that is the result from the interference signal coming from different reflectors within the sample itself. This term gives rise to artifacts located close to the zero path length in the A-scan since the sample is usually relatively thin and the path length difference between the different reflecting particles is very short. This artifact is taken care of by setting the reference arm power to a value much larger than that of the reference arm. Since $I(k)_{Detector}$ is composed of real values measured by the photodetector, the IFT results in a symmetrical A-scan (Hermitian symmetric) containing a mirror image. This is called the complex conjugate artifact. If the axial range of the OCT system is long enough so that the whole sample could be kept on one side of the zero path length (z = 0), this artifact can be taken care of by using only half of the A-scan. However, for thicker samples the actual and the mirror images overlap. In this case, combinations of hardware and software techniques are employed to remove the complex conjugate artifact and to utilize the entire axial range[12]–[15]. Figure 1.4 is a schematic sample FdOCT A-scan depicting the different terms explained above

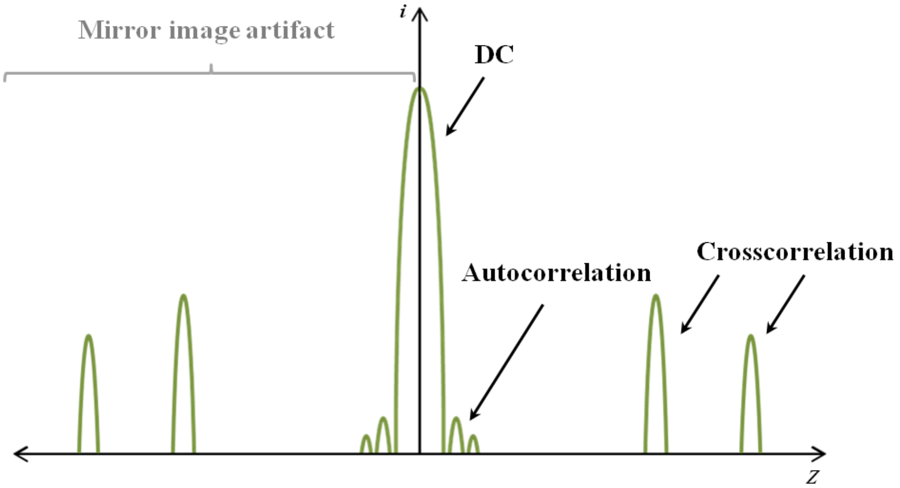

Figure 1.4: schematic of a sample FdOCT A-scan.

FdOCT comes in yet two different designs. The first one is known as spectral domain OCT (sdOCT) in which a low coherence light source is used at the input of the OCT system and the interference pattern is detected with a combination of a spectrometer and a linear array camera[16].

The second method is called swept source OCT (ssOCT) in which a frequency-swept laser is used as the light source at the input of the OCT system and the interference signal is detected by a single photo detector as a function of time[10], [17]. In other words, data to reconstruct an A-scan is acquired by recording the fringe pattern corresponding to a complete sweep cycle of the light source.

An obvious advantage of FdOCT over TdOCT is the improved imaging speed since the reference arm is fixed and the information from the entire sample depth is collected simultaneously within one camera read out (sdOCT) or one frequency sweep of the tunable laser (ssOCT). Recently, with improvements in new line scan cameras, high speed sdOCT systems with A-scan rates of 500 KHz[18] (dual high-speed line scan CMOS cameras, 850 nm central wavelength, 8 µm axial resolution), 244KHz[19] (CCD line camera, 840 nm central wavelength, 5.7 µm axial resolution), 312KHz[20] (CMOS line camera, 850 nm central wavelength, 9 µm axial resolution) and 92

KHz[21]–[23] (CCD line camera, 1020 nm central wavelength, 5 µm axial resolution) are available. With improvements in swept light sources, ssOCT systems with A-scan rates of 512KHz[24] (830 nm central wavelength,18µm axial resolution), 249 kHz[25] (1060 nm central wavelength,8µm axial resolution) 400 KHz[26] (1050 nm central wavelength, 5.3 µm axial resolution) and 1.37 MHz[27] (1050 nm central wavelength, 19µm axial resolution) were reported.

Another important advantage of FdOCT is its improved signal to noise ratio (SNR)[9]–[11]. In general, SNR is defined as

$$SNR = \frac{\langle I_{Detector} \rangle^2}{\delta^2}$$

(1.9)

where $\langle I_{Detector} \rangle^2$ is the signal power and δ^2 is the variance of the noise. For TdOCT this value is

$$SNR_{TdOCT} = \frac{\rho S_{TdOCT} R_s}{2eB_{TdOCT}}$$

(1.10)

Where ρ is detector sensitivity, $S_{TdOCT} R_s$ is the power returning from the sample, e is the electron charge and B_{TdOCT} is the detection bandwidth. SNR for FdOCT is

$$SNR_{FdOCT} = \frac{\rho S(k_m)_{FdOCT} R_s}{2eB_{FdOCT}} \frac{M}{2}$$

(1.11)

where ρ is detector sensitivity, $S(k_m)_{FdOCT} R_s$ is the power returning from the sample for each detection channel, e is the electron charge and B_{FdOCT} is the detection bandwidth. In this case, the factor M is to account for the number of detection channels which is the number of camera pixels in sdOCT and number of detector readouts for a complete sweep cycle in ssOCT. The $\frac{1}{2}$ coefficient in Eq.1.11 is due to the fact that IFT used in FdOCT data processing is applied on the real data gathered from the detector and hence results in a symmetrical A-scan (Hermitian symmetric) containing a mirror image. Therefore, only half of the data is used to construct FdOCT images. For similar $\frac{\rho S R_s}{B}$ for both TdOCT and FdOCT and a square shaped spectrum in which all frequencies have equal power, the relationship between the SNR values is

$$SNR_{FdOCT} = SNR_{TdOCT} \frac{M}{2}$$

(1.12)

For a Gaussian spectrum the FdOCT SNR is reduced by an extra factor of 2. In application, Fourier domain detection improves the SNR of OCT system by a factor of ~100 (20 dB)[1].

It is important to note that Eq.1.10 and Eq.1.11 are correct when a shot noise limited detection criterion is satisfied. The reference arm power must be high enough so that the shot noise dominates other noise present [1].

1.2.4 Major Limitations to FdOCT System Performance (Sensitivity Fall-Off, Maximum Scanning Range and Dispersion)

In real-world applications, the finite spectral resolution and sampling points of the detection system pose limitations to FdOCT system performance. The detection system has limited spectral resolution which is determined by the instantaneous line width of the source in ssOCT and by the finite spectrometer resolution and camera pixel spacing in sdOCT. This finite spectral resolution can be modeled by a Gaussian function with its $FWHM = \delta k$ as the spectral resolution in terms of wavenumber. This affects on the spectral measurement can be taken into account by convolving the ideal interference signal $I(k)_{Detector}$ by the Gaussian resolution function

$$I(k)_{Detector} \otimes \exp\left(\frac{-4\ln(2)k^2}{\delta k^2} \right)$$

(1.13)

Applying IFT on Eq.1.13 will result in the ideal A-scan $i(z)$ to be multiplied by a Gaussian "fall-off" function which is the inverse Fourier transform of the Gaussian resolution function

$$i(z)\times\exp\left(\frac{-z^2\delta k^2}{4\ln(2)}\right)$$

(1.14)

Hence, the sensitivity decreases exponentially with imaging depth z (i.e. larger depths in the A-scan)[1].

The maximum scanning range in FdOCT, $z_{\max}$, is determined by the number of sampling data channels M which relates the spectral resolution of the detection system, δk, and the bandwidth of the effective light source spectrum, Δk through equation 1.15.

$$\Delta k = M\delta k$$

(1.15)

The one sided maximum depth of the A-scan is given using the Nyquist criterion as

$$z_{\max} = \frac{\pi}{2\delta k} = \frac{1}{4}\frac{\lambda_0^2}{\delta\lambda}$$

(1.16)

where $\delta\lambda$ is the spectral resolution of the detector in terms of wavelength and λ_0 is the central wavelength of the light source detected by the detector[1].

The axial pixel resolution of an OCT tomogram is determined by the maximum depth ($z_{\max}$) and the number of pixels ($\frac{M}{2}$) in the A-scan.

$$Axial\ \ pixel\ \ resolution = \frac{z_{\max}}{M/2}\times 2 = \frac{4z_{\max}}{M}$$

(1.17)

Where the factor $\frac{1}{2}$ in $\frac{M}{2}$ indicates that an A-scan in the tomogram uses only half of the pixels due to the presence of the mirror image artifact. The factor 2 indicates that there needs to be 1 pixel between the two resolved pixels according to the Nyquist sampling theorem.

The lateral OCT image pixel resolution depends on the physical scanned length on the sample (L_{B-scan}) and the number of A-scans $N_{A-scans}$ in a B-scans. The factor 2 in this case is also the result of the Nyquist sampling theorem.

$$Lateral\ \ pixel\ \ resolution = \frac{2L_{B-scan}}{N_{A-scans}}$$

(1.18)

Material dispersion both within the imaging system and the imaged object, leads to dispersion mismatch between the sample and reference beams and introduces a frequency dependant phase $\phi(\omega)$ in which $\omega = 2\pi\upsilon$ is the angular frequency. Dispersion reduces the axial resolution by broadening the point spread function (PSF). Since the total signal received by the detector is conserved, the height of the PSF is reduced as the axial resolution decreases (i.e. as the PSF broadens) hence reducing the SNR[1]. Dispersion can be compensated physically[28] and computationally[16], [29], [30]. To physically compensate this effect, dispersion in the reference and sample arms must be matched as well as possible by using suitable materials in both arms. The remaining dispersion is then compensated computationally by multiplying the complex conjugate of dispersion phase shift $\phi(\omega)$ by the interference data in frequency space

$$W(\omega)_{comp.} = W(\omega)_{disp.} \times \exp(-j\phi(\omega))$$

(1.19)

where $W(\omega)_{disp.}$ and $W(\omega)_{comp.}$ are the spectral data before and after numerical dispersion compensation respectively.

Moreover, since dispersion is both material and wavelength dependant, it is possible to find the most suitable wavelength region for specific OCT applications (e.g. ~1 µm in the case of soft tissue which mostly contains water[31]) to minimize the depth dependant axial resolution broadening due to dispersion effects in the sample beam propagation within the sample.

1.3 OCT in *In Vivo* Retinal Imaging

One of the most important and exciting biomedical applications of OCT is in the ophthalmic field for high resolution, volumetric imaging of the posterior segment of the eye (the retina). The first biological application of low coherence interferometry was to measure the eye length[32] and the first *in vivo* human retina OCT images were presented in 1993[33], [34].

OCT provides non-invasive, non contact, high resolution, *in vivo*, cross sectional images of the biological tissue and hence is well suited for probing the retina and the choroid. With the advent of ultrahigh resolution OCT (UHR-OCT)[35]–[37] the axial resolution of retinal OCT images has improved from ~10 µm (in standard commercial OCT systems) to ~2-3 µm, enabling visualization of the multilayered structure of retina *in vivo* in healthy and diseased subjects[38]–[40]. Clinical studies have demonstrated the effectiveness of UHR-OCT for 3D visualization of retinal structural changes in pathologies such as macular holes[41], central serous chorioretinopathy[42], age-related macular degeneration(AMD)[43], glaucoma[44], diabetic retinopathy[45], [46], foveomacular dystrophies[47], Stargardt's dystrophy[48] and retinitis pigmentosa(RP)[49]. These studies have improved our understanding of the origin, mechanisms and progression of such retinal diseases, as well as their response to therapy. In fact, UHR-OCT makes available more structural detail of the multilayered retinal tissue than any other *in vivo* imaging technique.

Animal models, especially rodents, are used widely to investigate healthy and diseased retinas[50]–[55]. UHR-OCT provides detailed cross sectional images of animal retina depicting all intra-retinal layers. This method enables longitudinal, repeated measurements on the same animal and allows for tracking the disease progression more accurately, investigating the intra-animal variability, and significantly reducing the number of animals used per study, as compared to invasive methods using histology.

Originally, the first retinal OCT images were acquired in the 800 nm region due to optical clarity of ocular media (low water absorption and scattering), as well as tissue safety considerations. Broad bandwidth spectra at this region allow for very high axial resolution and hence unprecedented high quality images of the retinal structure *in vivo*. However, OCT imaging in this wavelength region has limited depth penetration in the eye beyond the retinal pigment epithelium (RPE). Melanin, the main chromophore with high concentration in the RPE layer, is highly scattering and absorbing in the 800 nm region and hence attenuates the imaging light intensity. Therefore, in the OCT images acquired at this spectral region, the choriocapillaris and the choroidal structure of the human eye are not visualized. Furthermore, the OCT image quality is severely affected at this region by any opacities in the intraocular media such as cataract and corneal haze which strongly attenuate the incoming and outgoing beam[56]. These factors limit the retinal OCT imaging in the 800 nm wavelength region.

The optical properties of melanin (refractive index, scattering and absorption) are strongly wavelength dependent and decrease as the wavelength increases. Similar behavior is also observed in the scattering properties of the ocular opacities[57]. On the other hand, the intraocular media mainly consists of water and water absorption increases significantly at wavelengths longer than 1200 nm [58], [59]. Since the OCT imaging beam travels a double pass through this media, water absorption attenuation poses strict limitations to *in vivo* OCT imaging at longer wavelengths.

Considering all mentioned factors, another optimal window for retinal imaging is located at 1050 nm where there is a local minimum in the water absorption coefficient. The permissible safe optical imaging power at this region is higher than that of the 800 nm region according to the ANSI standard[60]. OCT images at this region show great improvement in depth penetration below the RPE, visualizing choroidal features. This is very important for clinical applications since the earliest site of pathology in some retinal diseases such as neovascular AMD is below the RPE layer (i.e. RPE/choroid interface)[61]. Studies have demonstrated superior OCT image contrast and penetration in patients with ocular opacities at 1050 nm region[62]. Another advantage is that photoreceptors are not sensitive to this wavelength region hence allowing OCT to be used for probing the response of retina to external stimuli[63]–[65].

Despite all these advantages, according to Eq.1.4 , a longer central wavelength of the imaging beam leads to reduced axial and lateral resolution in the 1050 nm region compared to the 800 nm region for an equivalent bandwidth. Therefore, it is important to choose a suitable spectral range for retinal imaging depending on the features of interest.

1.4 Other Methods for *In Vivo* Retina Imaging

Other modalities such as fundus photography, confocal scanning laser ophthalmoscope (cSLO), fundus autofluorescence (FAF), fluorescein angiography (FA), Indocyanine green (ICG), are also used in *in vivo* retinal imaging.

In fundus photography, a single flash illuminates the whole retina simultaneously and the back reflected light is detected by a 2D CCD camera. The low intensity of the back-reflected light and the fact that this reflection comes from all different ocular layers (i.e. cornea, crystalline lens, retina and choroid) limit the quality of the images.

A more advanced imaging technique is cSLO which uses low power lasers to raster-scan the tissue surface and applies confocal gating to suppress the reflections from out of focus layers hence resulting in higher image contrast and resolution and allows for depth scanning by changing the focal plane within the sample[66]. cSLO axial and transverse image resolution are determined mainly by the beam diameter and the power of the focusing lens. The cSLO lateral resolution is the radius of the spot size of the focused beam on the retina (Eq.1.5) and the axial resolution is determined by the confocal parameter (Eq.1.6). These are both inversely proportional to the NA. To gain high resolution high NA is desirable. In the case of human eye, this could be achieved by increasing the beam diameter according to

$$NA \propto \frac{D}{f}$$

(1.20)

Where D is the beam diameter in the entrance pupil and f is the eye's first focal length. However, for beam diameters larger than ~3mm the eye's aberrations will degrade the resolution on the human retina[38]. Equations 1.5 and 1.6 show that the diffraction limited lateral and axial resolutions are ~5.4 µm and ~115 µm respectively, for 3 mm pupil size, 800 nm central wavelength and 60 dioptres of power in the human eye. Since the OCT lateral resolution is the same as that of cSLO, it is also affected by the aberrations and limited to the maximum value of ~5.4 µm in *in vivo* human retinal imaging.

All three major retinal imaging modalities (i.e. fundus photography, cSLO and OCT) can be combined with adaptive optics (AO) for improved performance[67]–[69]. Adaptive optics uses a larger pupil, wavefront sensor and a corrector (usually a deformable mirror) to correct the wave front coming from the sample to compensate for the aberrations caused by the optics of the eye and the imaging instrument. AO increases the image contrast and improves spot size on the retina (and also transverse resolution) to ~2.3 µm in the human eye (for 800 nm central wavelength and 7 mm pupil size)[70] and permits cellular resolution imaging[71]. cSLO combined with OA results in axial resolution of about ~40 µm (human)[72]. In the case of small eyes, the higher NA allows for better cSLO diffraction limited lateral and axial (confocal parameter) resolution at the retina when the aberrations are corrected for using AO. For instance, using Eq.1.5 and Eq.1.6, the diffraction limited lateral and axial resolutions are ~1.3 µm and ~5.2 µm in the rat retina respectively for 1020 nm central wavelength, 3 mm pupil size and 300 dioptres of power in the rat eye.

Among the methods mentioned above, unlike OCT that is sensitive only to the back-scattered coherent photons, both fundus photography and cSLO techniques can be used to detect fluorescence photons emitted from the tissue. This advantage allows for extracting additional information from the retina and choroid. However, using cSLO imaging has the advantage of improved image contrast and resolution and suppression of the off-focus emission when compared to fundus cameras.

Fundus autofluorescence (FAF) is mainly used to monitor the RPE layer. The RPE layer is a monolayer located between the sensory retina and the choroid, which contains the blood network [73]. This layer plays a fundamental role in maintaining the photoreceptors' health and function by regulating the transition of nutrients from the choroid to the retina and the waste from the retina to the choroid. In particular, RPE cells constantly perform phagocytosis (digestion) of the shed membrane disks in the photoreceptor's outer segment. RPE contains granular lipid-containing pigments called lipofuscin. Excess lipofuscin accumulation, observed in the form of drusen in some retinal degenerative diseases such as dry AMD, is caused by incomplete digestion of the photoreceptor outer segment discs and incomplete disposal of the waste material[74], [75]. Lipofuscin is the main source of retinal autofluorescence with an excitation range of 300-600 nm and emission range of 480-800 nm (peaks at ~600 nm). It has been shown that autofluorescence increases with RPE dysfunction and decreases in regions with RPE loss. Therefore, FAF is used to assess the metabolic integrity of the RPE-photoreceptor complex[76].

FA and ICG angiography use fluorescent dyes for monitoring blood vessel distribution as well as detection of abnormalities such as vessel atrophy, abnormal vessels, neovascularization and leakage in the retina and choroid[77]. A fluorescent dye is injected into the blood stream and the emission is detected after illuminating the posterior segment using a suitable light frequency of ~490 nm and ~800 nm in FA and ICG angiography respectively. The infrared fluorescence emission in ICG angiography (peak at 830 nm) has the advantage of being less attenuated by the melanin pigment and the possible opacities in the anterior segment, hence allowing for improved visualizing of choroidal vasculature[78].

Modalities discussed above along with OCT are considered complimentary since each provides useful but different information from the posterior segment. Therefore, combined systems have been developed for simultaneous, multimodal data acquisition[69], [72]. cSLO provides a large angle *en face* view of the retina and detects some large scale abnormalities while adaptive optics corrected cSLO provides a smaller field but higher resolution. OCT provides cross-sectional high resolution images with micrometer scale detailed information of individual retinal layers. FAF provides a topographical map of the lipofuscin in the RPE layer, as well as other fluorophores that might occur due to pathology. Angiography in FA and ICG angiography on the other hand, provide detailed information about blood vessels and capillaries within the retina and choroid.

Chapter 2

Outer Retina Degeneration

2.1 Human Outer Retina Degenerative Disease

Outer retina degenerative diseases such as AMD and retinitis pigmentosa (RP) are the leading cause of blindness in developed countries. The mechanism and pathway of these diseases are not yet fully understood and hence there are usually no effective prevention and treatment methods available.

AMD is a chronic progressive disease with both genetic and environmental factors involved. It is often observed in the elderly population and is one of the major causes of vision impairment in people over 50 years of age[79]. As is mentioned in the name, AMD affects the macula which is located in the central retina and is responsible for our small detail vision. The early stage of the disease usually manifests by the appearance of focal hyper and hypo-pigmentation and accumulation of cellular debris below the RPE layer known as drusen[80]. There are two outcomes as the AMD develops to its advanced stage; geographic atrophy (GA) and choroidal neovascularization (CNV). GA also known as late stage "dry" AMD, is characterized by wide-spread loss of RPE cells in the macular region accompanied by atrophy and loss of photoreceptor body and nuclei[81]–[83]. There is currently no effective treatment protocol for GA. In CNV, also known as exudative or "wet" AMD, vision loss is usually due to abnormal blood vessels growth (neovascularization) in the choroid with leakage into the sub-retinal space damaging the outer retina[84], [85]. Treatments methods such as photodynamic therapy and anti-VEGF drugs are often used in wet AMD patients[86].

RP, also called tunnel vision, is a set of inherited retinal dystrophies affecting the photoreceptor and RPE complex, that lead to progressive peripheral vision loss followed by central vision loss. The earliest observed morphological change is shortening of the rod and cone outer segments. In later stages, rod photoreceptor loss affects the peripheral retina while cone loss later affects the macula[87]–[89]. There is currently no effective treatment for RP.

Clinical studies using different modalities are used to monitor the progression of disease and their response to therapy. However, studies often miss the onset of the disease since patients are usually diagnosed and referred when they have already developed some later stage of the disorder. In addition, the slow rate of disease progression typically renders longitudinal studies very time consuming and costly, while it is very difficult to control and monitor all factors affecting the pathology in different individuals. Needless to say that new trial treatment procedures and drugs cannot be tested on human subjects, unless they have been proven sufficiently safe through extensive prior animal studies. All these factors point to the necessity of conducting animal studies to fill the gap in ophthalmic research.

2.2 Animal Models of Outer Retina Degeneration

Animal models of human disease are extensively employed to monitor the onset and mechanism of disease development, as well as testing novel pharmaceutical and genetic therapies. Although these models are often somewhat different from the actual disease they are supposed to mimic, they bear similarities to the disease characteristics and therefore can provide useful information as to the origins and pathways of the disease progression.

Animal models especially rats and mice with light induced, drug induced and inherited retinal degenerations have been developed to investigate outer retina degeneration. In these models, the disease onset and progression is generally faster (days, weeks or months) as compared to the human counterpart (years or decades), and the onset occurs within an expected time interval enabling longitudinal follow-up of all staged of the disease. Furthermore, the environment and other important variables can be controlled and monitored easily. In addition, novel treatment methods can be tested on laboratory animals before their application in clinical trials.

Photoreceptor apoptosis (programmed cell death) is characteristic to outer retina degeneration and is observed in many animal models as well as human diseases. Therefore, animal models can be useful to develop treatments to block this final pathway and inhibit apoptosis, in order to rescue the photoreceptor cells[90], [91].

In light induced retinal degeneration, focal high intensity light exposure results in localized photoreceptor apoptosis within a few hours to a few days[92], [93]. OCT images acquired from mice have recently revealed areas of edema (fluid accumulation) in the sub-retinal space as a result of light induced damage[53]. High power laser pulses are also used to rupture the Bruch’s membrane below the RPE (photocoagulation) causing light induced choroidal neovascularization to model wet AMD[94], [95].

Genetically altered animals (especially mice) are used to investigate photoreceptor and RPE degeneration[54], [96], [97] as well as treatment methods such as gene therapy[98] and stem cell therapy[99]. These models could be categorized into different groups based on the type of abnormality such as defects in the photo-transduction cascade, RPE function (visual cycle and outer segment disc phagocytosis), RPE pigmentation, structure of the outer segment, protein transport to the outer segment and photoreceptor development[96]. Studies have confirmed that photoreceptor cell death occurs through apoptosis in various underlying gene defects[96], [100].

Many chemicals and drugs are also known to cause retinal toxicity, dysfunction and degeneration. Animal models are very valuable to assess the effect and safety of new drugs on retina. Furthermore, chemical compounds such as iodoacetic acid[101], hemicholinium-3 (HC-3)[102], N-ethylmaleimide (NEM)[103], N-methyl-N-nitrosourea (MNU)[104], urethane[105], and sodium iodate[106] are used to induce photoreceptor or RPE disruption leading to outer retina degeneration.

As mentioned above, rodents especially mice and rats are the most popular models used to study human retinal disease. These small animals are easy to handle and inexpensive to house. There are many transgenic models available and the disease progression is relatively fast. However, the low cone/rod ratio and absence of fovea makes rodent models less useful for human disease involving cone photoreceptors. In this case other animals such as swine, prove to be more suitable.

2.3 Sodium Iodate Model of Outer Retina Degeneration

Sodium iodate is a strong oxidizing agent used to induce outer retina degeneration. This substance is selectively toxic to RPE cells[107]. The RPE provides multiple physical and biochemical functions supporting and regulating photoreceptors such as: blood-retinal barrier, adhesion of the neuro-sensory retina, decreasing light scattering, protection against oxidative stress, phagocytosis of shed photoreceptor outer segments, vitamin A recycling, storage, and transport to photoreceptors, synthesis and maintenance of the inter-photoreceptor matrix, synthesis and secretion of growth factors[108]. All these functions are critical to the photoreceptor survival and disruption in any of them can lead to photoreceptor degeneration. Therefore, RPE dysfunction and death in sodium iodate toxicity results in secondary photoreceptor degeneration[106].

Sodium iodate was originally used in Germany during the 1920s as the main ingredient in an antibacterial preparation called "Septojod". The first observation of its toxic effect was reported in 1941 by Sorsby as rapid loss of visual acuity and blindness after intravenous administration to treat puerperal sepsis[109]. Subsequent animal studies conducted on rabbits, cats, dogs, sheep, rats and mice, showed immediate changes to the *in vivo* visually evoked electrical activity of the retina, measured with electroretinography (ERG), as well as structural changes in the outer retina (*ex vivo histological analysis*) confirming the toxic effect of sodium iodate[110]–[115].

2.3.1 Short-Term Effects of Sodium Iodate on Retina

So far, different methods have been used to study the acute effects of sodium iodate (within the first 24 hours) on the retina structure and visual function. Studies on rats and mice have shown severe loss of visual acuity 2 hours post 50mg/kg intravenous (IV) drug administration. 24 hours after drug injection, electron microscopy images have shown vacuolation and degeneration of RPE and disorganization of photoreceptor outer segment while there was no observable qualitative reduction in photoreceptor nuclei[116]. Light microscope images of C57BL/6 mice retinas at 24 hours showed disorganization of the outer and inner segments of photoreceptors with flattened individual RPE cells devoid of nuclei[107]. H&E stained sections from C57BL/6 mice injected with 50 mg/Kg (IV) sodium iodate showed ~50% increase in photoreceptor body (inner and outer segment) thickness at day 1 suggesting swelling. This thickness was back to normal on day 3 followed by a gradual decrease until day 28 (~80% thickness reduction)[117].

Histological cross-sections acquired 6 hours post 60 mg/Kg (IV) drug injection in Sprague Dawley rats showed no change in the thickness and count of ONL nuclei. However, the photoreceptor outer segments were disorganized[114].

Electron and light microscopy images acquired from ICR (albino) and C57BL mice after receiving 100mg/kg intraperitoneal (IP) injection showed hyper-chromatic nuclei and karyolysis and swollen cytoplasmic organelles in RPE cells at 6 hours followed by decreased number of RPE cells at

12 hours post injection. Further decrease in RPE cell number and increased cell destruction (indicating necrosis) accompanied by disorganized photoreceptor inner and outer segments with some condensed photoreceptor cell nuclei (indication of apoptosis) were observed at 24 hours post drug administration. At this time karyolysis, loss of apical microvilli and numerous vacuoles indicate RPE cell necrosis. TUNEL (Terminal deoxynucleotidyl transferase) staining was used to identify apoptotic cell nuclei. TUNEL-positive photoreceptor cells were detected as soon as 6 hours, increased gradually at 12 and 24 hours and reached their maximum at day 3 post drug injection indicating that photoreceptor cell death is through apoptosis. In the case of RPE however, the cell ultra-structural changes (starting as early as 6 hours) as well as negative TUNEL signal confirm that necrosis is the pathway for RPE cell death. The same results were obtained in male and female mice, as well as albino and pigmented mice used in this study[106].

Another similar study also looked at the early effects of 40mg/Kg (IV) sodium iodate on ICR mice 2, 4 and 24 hours post injection. Electron microscope images showed normal RPE and outer segment 2 hours after injection. At 4 hours, RPE cells showed swollen organelles, disarranged basal infoldings at this stage most of the outer segments seemed normal. At 24 hours, RPE cells were irregular in shape and reduced in height with many granular materials and vacuoles in the cytoplasm. Some photoreceptor outer segments had disorganized outer segments indicating damage extending to the neurosensory retina[118].

ICG angiography performed on pigmented rabbits receiving 20 mg/kg sodium iodate in the ear vein showed many spots of hyper-fluorescence scattered over the retinal posterior pole 3 hours after injection indicating leakage from the choriocapillaris. Electron microscopy showed damage in RPE cells and choriocapillaris (CC) narrowing in the areas with ICG leakage. 24 hours later, homogeneous bright fluorescence was observed over the whole region. RPE cells showed signs of necrosis consistent with findings in other studies. Ultra-structurally, the cytoplasmic CC endothelial cell structure was not clear and endothelial walls were no longer connected to the basement membrane. Accumulation of tracer granules injected into the blood stream was detected in Bruch's membrane suggesting alteration of CC permeability at this time. The ICG leakage was reduced on day 7 and was back to normal values 14 days post injection. At this time the structure of CC endothelial cells looked normal while RPE cells were markedly damaged[119].

Kinetic vitreous fluorophotometry is a sensitive, non invasive method for detection of the permeability and integrity of the blood-retina barrier. The RPE and retinal vascular endothelial cells maintain this barrier and control the transport across, thus providing a suitable environment for the neural retina. Abnormally increased fluorescein values in the vitreous can be due to increased passive diffusion into the vitreous or decreased active outward transport by RPE. Anstadt et.al.[120] studied alterations in blood-retina barrier as a result of sodium iodate toxicity. Injection of 20 mg/kg (IV) of sodium iodete to Long Evans rats showed abnormally increased fluorescence in the vitreous reaching its peak at 2 hours as opposed to 1 hour in control animals. In the case of 60 mg/kg injected rats 24 hours post sodium iodate injection, the concentration of fluorescence in the vitreous reach the value of blood plasma 2 hours after IV fluorescence dye administration suggesting that free diffusion across the barrier had been established. For histological examination with light and electron microscope, horseradish peroxidase was injected (IV) 30 minutes before euthanasia. Retinas showed different degrees of patchy degeneration depending on the dosage. In areas with normal RPE, mild uptake of horseradish peroxidase into the RPE cytoplasm was detected. However, no leakage of horseradish peroxidase was found across the RPE into the retinal space. In damaged areas, RPE cells contained much more horseradish and showed apical rounding, swelling of mitochondria and apical microvilli while horseradish leakage into the space between photoreceptors was evident. There was no sign of leakage from retinal blood vessels. Hence, the choroidal blood retina barrier is severely disrupted at the RPE due to sodium iodate toxicity[120]. Contrast-enhanced MRI has also been used to visualize the blood-retina barrier breakdown and leakage of the contrast agent across the entire retinal extent in rabbits 24 hours after 30 mg/Kg sodium iodate injection via the marginal ear vein[121].

The force of adhesion of RPE to the neural retina, as well as the Bruch’s membrane, is also a factor to determine the integrity of the photoreceptor-RPE-Bruch’s membrane complex. IV injection of 20 mg/Kg sodium iodate in pigmented rabbits caused significant decrease (~50%) in the adhesion force 10 minutes after drug administration and the detachment accrued most often at the level of Bruch’s membrane. At about 100 minutes the peeling force decreased even further with separation mostly at the RPE level while electron microscopy showed RPE defragmentation and disorganized microvilli as well as disorganized photoreceptor outer segments (also reported by Ashburn et.al., 1980[122]). The sequence of preferred site of detachment (basal vs. apical) suggests that the drug initially affects the basal aspect of the RPE. As more damage and defragmentation occur over time, the apical aspect is affected as well. This might indicate that the RPE adhesion is stronger on the apical aspect as compared to the basal aspect[102]. These findings indicate that RPE active metabolic and barrier properties have immediate effect on retinal adhesion.

2.3.2 Long-Term Effects of Sodium Iodate on the Retina

Histological cross sections represented in a study on albino and pigmented rats and mice with 50 mg/Kg (IV) sodium iodate injection showed degeneration and fragmentation of RPE basal nuclei, and degeneration and smearing of the cytoplasm at day 7[116]. The OS layer was reduced in thickness with no clear boundary between the inner and outer segment accompanying some retinal folding disorganizing the photoreceptor cell nuclei. There was some gradual recovery of the visual function between 24 hours and 4 weeks post drug injection. Severe degeneration of the outer retina was observed in the central retina while the peripheral retina was less affected. This study also showed that the effect of the drug on albino retinas of rats and mice was more severe compared to pigmented retinas. Although the underlying reason is not currently clear, there is evidence for interaction between light and sodium iodate[91]. This effect might increase the damage potential in albino animals while melanin in pigmented retinas absorb the incoming light and reduce the light-drug interaction. Another possibility is more active role of melanin such as binding with sodium iodate or co-operation with antioxidant enzymes in the RPE[108], [123].

Machalińska et.al.[107] study on C57BL/6 mouse retina revealed RPE cells being replaced by a thin layer of melanin along Bruch's membrane at day 3 post 40 mg/kg IV drug injection. Discontinuity of the RPE layer and disruption of the inner and outer photoreceptor segments was observed in H&E stained samples while TUNEL staining revealed massive apoptosis in the outer nuclear layer. Fluorescence microscopy of flat mounts showed discontinuous melanin coverage with some nuclei present. At day 7 the outer and inner photoreceptor segments were significantly shortened and the ONL thickness (photoreceptor nuclei) was reduced. 18 and 28 days after, no RPE cover was present and patches of melanin clumps appeared along Bruch's membrane. There were indications that glial cells might contribute to phagocytosis of melanin remains. Retinal thickness was considerably reduced due to photoreceptor loss. This study also confirmed more profound damage to the central retina and better resistance of the peripheral regions to the drug.

Low dose administration (15 mg/kg, IV) of sodium iodate in C57BL/6 mice showed increased fluorescence-free areas (measured in retina flat-mounts) between days 7 and 28 of the study followed by some decrease (recovery) by month 3 suggesting possible regeneration or recovery of some RPE cells. Focal RPE loss with patchy regions devoid of RPE was observed in histological cross-sections on day 21 with no significant ONL damage. The thickness of the ONL was unchanged however, the number of nuclei was reduced at month 3. Visual function was moderately reduced on days 3 and 7 with slight recovery afterwards. With higher dose of 35 mg/kg, large regions of RPE loss was observed by day 3. Areas with no autofluorescence (i.e. RPE loss) in retina flat-mounts increased between days 7 and 28 showing slight recovery at month 3. The thickness of ONL and number of nuclei was reduced significantly at day 3 and continued to reduce over time to almost non-existent ONL at month 3. The visual acuity dropped to zero at day 3 and no recovery was observed within the 3 month study period. The partial recovery of the RPE cells (increased AF signal at month 3) along with non-recovery of the visual function suggests that although RPE cells might go through a recovery or regeneration process, their initial malfunction leads to permanent damage to the outer neurosensory retina[124]. Comparing the effects of the low and high drug dose in mice showed that the onset and extent of the outer retina damage is dose dependant and could be controlled.

Injection of very high dose,70 mg/Kg (IV), of the drug in C57BL/6 mice lead to complete absence of RPE autofluorescence signal (flat-mount) on days 3, 7 and 14. Significant reduction in photoreceptor body thickness was observed on day 3. ONL thickness and cell count showed significant reduction by day 7[117]. 60 mg/Kg (IV) of sodium iodate in Sprague Dawley rats showed irregular ONL alignment and ~50% reduction in ONL cell count on day 7. Photoreceptor outer segments were extremely shortened and disorganized. By day 28 ONL cell count decreases to ~40% of the baseline value while the cell count for inner nuclear layer (INL) and ganglion cell layer (GCL) remain unchanged[114].

Administration of 100mg/kg IP injection of sodium iodate to ICR (albino) and C57BL mice showed advanced destruction of photoreceptor inner and outer segments, decreased photoreceptor cell nuclei, flattened RPE cells on Bruch's membrane, Muller cell proliferation and melanin-phagocytosing macrophages migration into the photoreceptor layer at day 3. At this time photoreceptor apoptosis marker reached its maximum but was insignificant afterward on days 7 and 28. Patches of retina devoid of RPE and photoreceptor cells was observed with INL being directly in contact with Bruch's membrane in histological cross sections acquired on days 7 and 28. In this study, peripheral and central retinas in both strains as well as male and female animals showed similar results[106].

An early study (Korte,1984)[125] on pigmented rabbits receiving 2 doses of 25 mg/kg (4-6 hours apart) IV sodium iodate injection showed leakage across the RPE in fluorescence angiography 1 day post injection. One week later, diffuse fluorescence indicated blood-retina barrier breakdown. No fluorescence leakage was detected after this time point. Fundus photography showed patches of RPE degeneration. Light and electron microscopy showed a layer of non-pigmented, flattened cells and some highly pigmented ones on Bruch's membrane (possibly damaged RPE cells) as well as signs of CC atrophy. Four weeks post injection, CC was reduced or absent in areas of RPE loss but looked normal in areas of intact and normal RPE. At eleven weeks, larger areas with RPE loss was observed and remaining CC in those regions was encased by abnormally dense collagenous connective tissue. The RPE layer was replaced by scar tissue composed of transformed RPE cells and Muller cell processes covering the Bruch's membrane. No CC loss was detected in areas of normal RPE while RPE changes precede those of CC suggesting that CC depend on RPE cells for survival. Such correlation is also reported in other animal studies involving RPE damage[126], [127].

Many studies have reported more damage to the central retina when compared with peripheral retina especially in the case of low dose sodium iodate administration. The reason behind this difference is not still clear. A possible explanation is disparities in the local vascular anatomy leading to uneven distribution of the drug. It could also be due to different metabolism of the drug by the central and peripheral cells in the retina as well as different degree of regenerative potential in the RPE cells in these regions[107].

In summary, sodium iodate causes severe damage to the retina. Primarily, it leads to degeneration of the basal membrane, swelling of organelles, loss of apical microvilli and necrosis in RPE cells. The retinal adhesion is then weakened and the choroidal blood-retina barrier is compromised at the RPE. Consequently, photoreceptor outer segments become disorganized followed by entire photoreceptor cell degeneration while the choriocapillaris initially leaks and atrophies later as a response to the drug toxicity. None of the studies on the effect of sodium iodate on the retina have reported any damage to the inner retinal structure. All inner retinal layers preserved their normal structure even months after outer retina degeneration[106], [107], [114]–[116], [124]. On the other hand, all studies indicate that a normal RPE barrier and metabolic functions are critical for maintaining healthy PR and CC.

2.3.3 Clinical Relevance and Potential Applications

The sodium iodate induced outer retina degeneration model does not specifically and completely mimic any of the human retinal disease such as AMD or RP. It is rather a model of RPE loss with successive damage to the outer retina and choriocapillaris. A major difference between the sodium iodate model and human disease is the mechanism of RPE cell death. In human outer retina degeneration, RPE cell death occurs via apoptosis while necrosis is behind the RPE death in the sodium iodate model. Moreover, early AMD is associated with lipofuscin accumulation and formation of deposits on Bruch’s membrane leading to RPE cell death following loss of attachment to Bruch’s membrane[128]–[130]. In contrast, the Bruch’s membrane remains normal in the sodium iodate model[124]. In RP on the other hand, photoreceptor cell death precedes that of RPE cell as opposed to the order in the sodium iodate model.

Nevertheless, the sodium iodate model shares similarities with some aspects of the human retinal disorders and could serve as an inexpensive, convenient and controllable experimental tool. Quick onset retina degeneration is induced by a single dose of sodium iodate administration. The pattern and the degree of damage observed in outer retina is dose and time dependent and could be manipulated to some extent. Low dose administration of sodium iodate can cause diffused patches of RPE and photoreceptor loss similar to patterns present in some human disease such as RP and geographic atrophy (dry AMD)[107], [124], [125]. Although the initial target of toxicity is the RPE in sodium iodate injected animals, apoptosis is the final pathway of photoreceptor cell death in both the sodium iodate model and the human outer retina degenerative diseases such as AMD and RP. In addition, disruption of the choroidal blood-retina barrier similar to that observed in vitreous fluorophotometry of sodium iodate treated retinas is reported in diabetic patients[120].

Sodium iodate is used as the retinotoxic agent in toxicology studies, in testing new methods of measuring visual acuity in animals[116], [124], as well as for correlation of findings in different modalities investigating structure and function (e.g. ERG and histology)[107], [114], [131]. Moreover, it is currently used to investigate new treatments for human diseases that involve photoreceptor and RPE degeneration such as AMD. RPE damage in this model is specifically useful to evaluate novel therapy approaches for repopulating the RPE layer such as stem cell and growth factor applications[117], [132], [133]. Selective RPE loss could also be useful to investigate RPE cell regeneration on a normal Bruch's membrane[124], [125]. In addition, the dose dependency of the onset and severity of RPE damage and effects on the visual function in this model provides unique opportunity to adjust and study these aspects as desired to provide different degeneration patterns to mimic some aspects of specific diseases.

The reduced retinal adhesive force at Bruch's membrane could potentially be used as a model to investigate some aspects of RPE detachment in human eye. The model has it's limitation: for instance the photoreceptor and RPE damage might exceed that of real clinical situations. However, the nature of basal RPE attachment might provide insight into some aspects of human pathology such as AMD. Furthermore, CC atrophy is observed in areas of RPE loss in both sodium iodate model and human retinal diseases such as AMD and RP and could be useful in better understanding of the role of normal RPE function in CC well-being.

2.3.4 What is missing?

In study of sodium iodate effects on the retina, both *in vivo* and *ex vivo* methods have been employed. However, high resolution cross sectional information about the multilayered structural of retina was only provided *ex vivo* by use of histological preparations. Histology is currently the gold standard to study the microscopic cellular and sub-cellular structure of biological tissue. Nevertheless, the preparation steps (i.e. fixation, embedding, cutting, mounting, staining and etc.) could potentially be a source of artefacts. Furthermore, some changes such as edema and focal retinal detachments could remain undetected in histological analysis. Needless to mention that *in vivo* monitoring of the dynamic changes in the same subject is also of great value in longitudinal studies for better understanding of the mechanisms involved, as well as investigating inter-subject variability. Furthermore, *in vivo*, non invasive methods could potentially be used to explore the correlations among structural, functional and blood flow simultaneously. Ultrahigh resolution optical coherence tomography provides the opportunity to address some of these issues by allowing for high speed, high resolution, *in vivo*, non invasive, cross sectional, volumetric imaging of the retinal layers.

Chapter 3
Methods

3.1 Fourier Domain OCT System

The Fourier domain OCT system used for all studies described in this thesis is a fiber-based sd-OCT system, designed to operate in the 900-1200 nm wavelength range[51]. Fig.3.1 shows a schematic of the system:

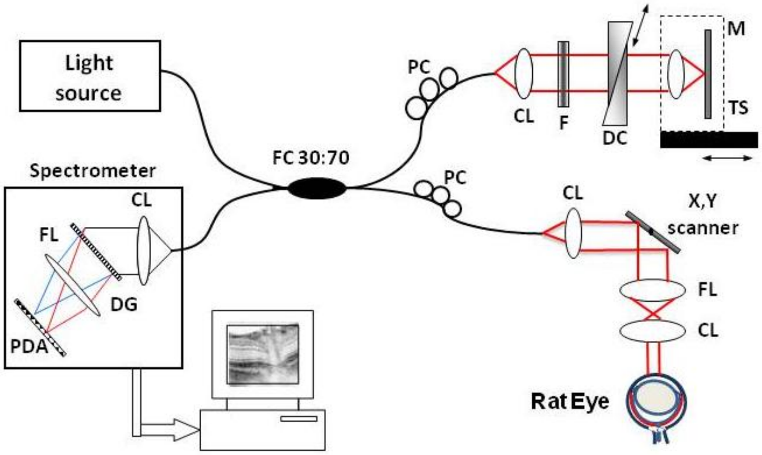

Figure 3.1 Schematic of the ultrahigh-resolution FdOCT system. System components are; TS-translation stage, M-mirror, DC - dispersion compensation unit, CL-collimating lens, F- neutral-density filter, PC-polarization controllers, FC-fiber couppler, SLD – superluminescent diode, CL-collimating lens, FL-focusing lens, X-Y scanning mirrors, DG- diffraction grating, PDA-photodetector array.(Figure reproduced from[134] with permission from the journal)

As seen in Fig.3.1, the sample arm is comprised of a polarization controller unit, 3 achromatic lenses (Edmund Optics) for providing a collimated beam at the cornea and a pair of X-Y galvanometric scanners (Cambridge Technology Inc.). The reference arm includes a polarization controller unit, a pair of lenses to focus the beam on the mirror, a neutral density filter to reduce the beam power that reaches the camera to prevent CCD saturation, and a dispersion compensation double prism unit to match the dispersion in the reference arm with the sample arm. In the case of *in vivo* human and animal imaging, 25 mm and 5 mm water cells (respectively) were inserted in the reference arm to compensate approximately for the dispersion due to the water content of the imaged eye. When testing the system's performance (measuring the system's SNR and axial PSF) with a mirror as the sample, water cells were inserted in both sample and reference arms. All optical and fiber optic components of the FdOCT system were selected to support the propagation of broadband light through the system with minimal spectral and power losses. A custom-built light source (Superlum Inc., λc = 1020 nm, Δλ = 110 nm and P_{out} = 10 mW) was interfaced to the OCT system. The interference signal was detected by a high efficiency custom spectrometer (P&P Optica Inc.), connected to a 1024 pixel linear array CCD camera (SUI Goodrich) with 47 kHz readout rate. The spectrometer was designed for the spectral range 940 - 1120nm and provided average absolute grating efficiency >80% over the entire spectral range, as well as spectral resolution of δλ = 0.15 nm. The OCT system provides 99 dB signal to noise ratio for 1.6 mW power of the incident sample beam and 1.1 mm axial scanning range in free space. Data was acquired with a framegrabber (National Instruments, PCIe-1429) and was processed and displayed by a computer (Intel Xion, 3.6 GHz, 2GB RAM).

3.2 Simulating the Water Absorption Effect on OCT Axial Resolution

A simple computational model was developed, which considers the effect of water absorption on the spectral bandwidth and central wavelength of an optical beam propagating through a water layer that approximates the water content of the rodent and human eye. A schematic representation of the model is shown in Fig.3.2. An optical imaging beam with initial spectral content and intensity $I_0(\lambda)$ is incident on an eye (Fig.3.2b) with physical length d (distance between the front surfaces of the cornea and the retina), or a water cell with the same physical thickness, d (Fig.3.2c).

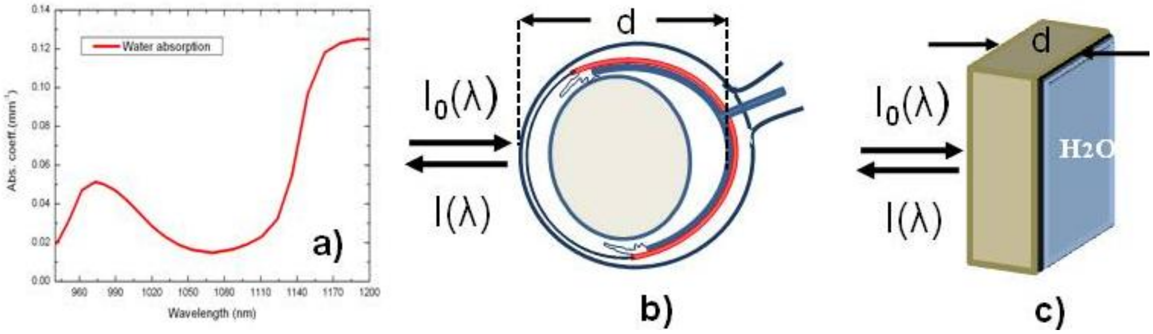

Fig.3.2 Water absorption profile (a); Schematic representation of the eye (b) and a water cell (c): $I_0(\lambda)$ – intensity of the incident optical beam; $I(\lambda)$ – intensity of the back-reflected optical beam; d – physical distance between the cornea and retina (b), equivalent to the thickness of the water cell (c). (Figure reproduced from[134] with permission from the journal)

The water cell is a simplified model of the eye, which neglects the absorption and scattering properties of any other materials comprising the ocular tissue except for water. The intensity and spectral content of the optical beam back-reflected from the retina (Fig.3.2b) or the back side of the water cell (Fig.3.2c) and measured after double pass though the eye / water cell is $I\left(\lambda\right)$. For weakly absorbing media such as water, the relationship between the intensity of the incident and detected optical beams is given by Beer-Lambert's law:

$$I(\lambda) = I_0(\lambda)\exp(-2\mu_a(\lambda)d)$$

(3.1)

Here $\mu_a(\lambda)$ is the wavelength dependent water absorption coefficient (Fig.3.2a) and the factor of 2 in the exponent accounts for the double pass of the optical beam through the eye / water cell. For this model, published values for water absorption were used[58], [59] and it was assumed that the average lengths of the rodent and human eye are 5 mm and 25 mm respectively.

Another factor that affects the final spectrum and therefore the OCT image resolution is the detector spectral response. In the case of our OCT system, the detector is a linear array CCD (LDH, SUI Goodrich). Fig3.3 shows the camera efficiency over the spectral range from 800 nm to 1300 nm. The spectral efficiency of the camera is very low at shorter wavelengths (20% for 800 nm) and increases monotonically to reach a plateau for wavelengths longer than 1000 nm with about 80% efficiency.

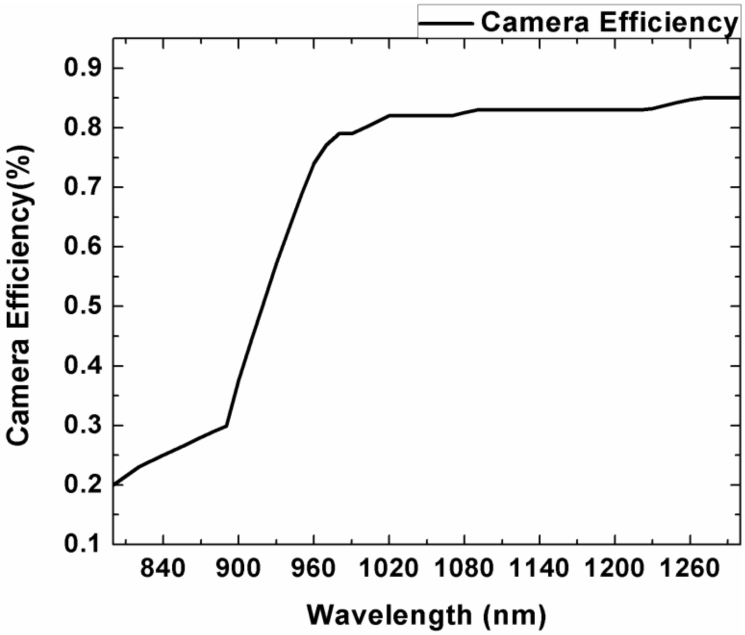

Figure 3.3 The CCD spectral efficiency from 800nm to 1300nm.

To take this factor into account, the intensity $I\left(\lambda\right)$ from Eq.3.1 was multiplied by the camera spectral efficiency $Cam(\lambda)$ to result in the final intensity $I\left(\lambda\right)_{final}$ as shown in Eq.3.2 below.

$$I\left(\lambda\right)_{final} = I\left(\lambda\right)\times Cam(\lambda)$$

(3.2)

To calculate the axial resolution, this final spectrum was first converted to wave-number space ($I\left(k\right)_{final}$) through Eq.3.3 and then re-sampled to equally spaced intervals in k-space.

$$k = \frac{2\pi}{\lambda}$$

(3.3)

The FT was performed on this equally spaced spectrum to generate the PSF and to calculate the resulting OCT axial resolution.

3.3 Imaging Probe

A custom imaging probe consisting of 3 achromatic lenses (Edmund Optics) and a pair of galvanometric scanners (Cambridge Technologies) was designed for *in vivo* imaging of rat retina. The schematic of the probe is depicted in Fig.3.4. L_0 is the lens at the output of the sample arm of the OCT system and collimates the beam incident on the scanning mirrors. The pair of X-Y scanning mirrors have a total maximum sweep angle of 20 degrees and are conjugate with the entrance pupil plane.

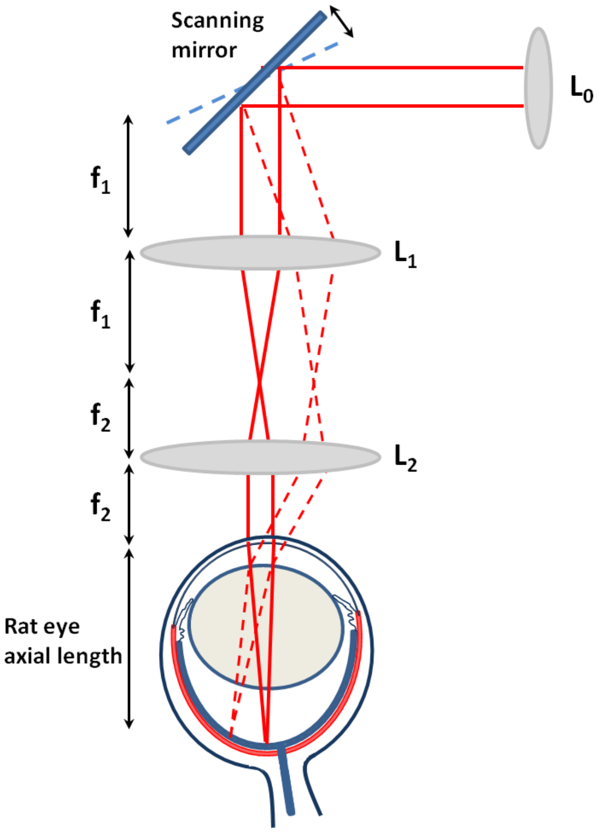

Figure 3.4 Schematic of the probe designed for imaging the rat eye. The probe consists of a lens (L_0) to direct a collimated bead to the scanning mirrors, a pair of X-Y scanning mirrors, a pair of lenses, L_1 and L_2, which direct a collimated beam onto the cornea. The scanning mirror is imaged into the entrance pupil plane of the eye.

A pair of 25 mm diameter lenses, L_1 and L_2, with focal lengths $f_1 = 60$ mm and $f_2 = 30$ mm respectively were used to direct a scanning collimated beam into the eye. When the imaging probe is interfaced with the UHR-OCT system, it provides a 1.2 mm diameter collimated imaging beam, incident on the rat's pupil and ~ 2 mm lateral field of view (FOV) at the retina.

The theoretical diffraction limited transverse resolution, according to Eq.1.5, is ~3.2 µm in the retina for 1.2 mm diameter of the imaging beam, 1020 nm central wavelength, 300 dioptres power of the rat eye. However, in practice, due to presence of aberrations in the rat eye, the transverse resolution is worse. Considering the fine structural features observed in the *en face* view in the reconstructed 3D images (i.e. capillary network in the plexiform layers, chapter 4), the actual transverse resolution in estimated to be ~5-10µm.

3.4 Animal Handling and Preparation

Mature female Long Evans rats (pigmented) were used in this study. All animal procedures were conducted in accordance with the regulations of the University of Waterloo Animal Care Committee and in compliance with the ARVO statement for ethical use of animals in ophthalmic and vision research. Animals were anesthetised with isoflurane (2.5 %) and pupil dilation was achieved by administering 1-2 drops of tropicamide 1% (Mydriacyl) in each eye. Outer retinal degeneration was induced by IV administration of 40 mg/kg of sodium iodate solution in the tail vein. During imaging, artificial tears were administered frequently to keep the corneas hydrated and optically clear.

3.5 Data Acquisition and Processing

Multiple 3D UHR-OCT tomograms were acquired from the right eye of each rat at the central region, about 1 mm temporal-superior to the optic nerve head. The unique blood vessel pattern at the optic nerve head was used to acquire images from the same location in the retina at different time points of the longitudinal study. The suitable location and orientation was initially found by imaging a wide area (2 mm x 2 mm) and then the central region (1mm x 1mm) was imaged and used for further qualitative and quantitative analysis. In all 3D volumes, the optic nerve head was located at the nasal-inferior corner of the 2 mm x 2 mm imaged area. Figure 3.5 shows a representative ~2 mm x 2 mm *en face* view from 3D reconstruction of retina structure using Amira software (Visage Imaging).

The structure at the lower left part of the image is the corner of the optic nerve head (Fig.3.5, white arrow). The desired central 1 mm x 1 mm region is marked by a white square.

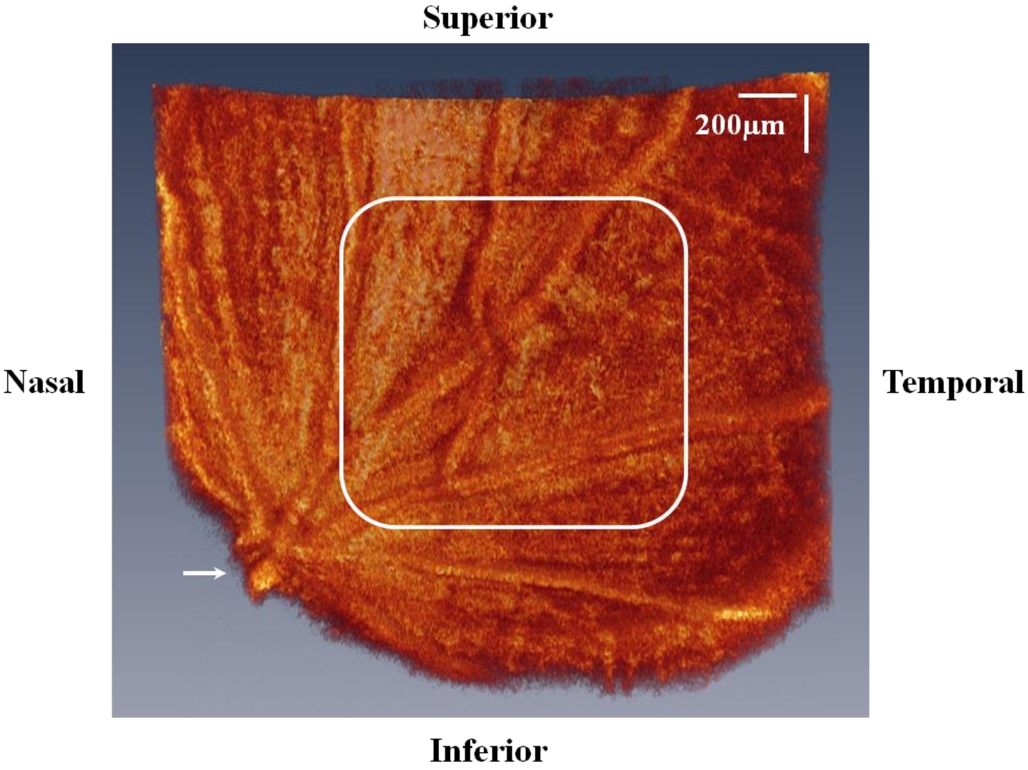

Figure 3.5 A sample *en face* view from the 3D reconstruction of wide FOV (2mm x 2mm) image acquired at the central region of a healthy rat retina with the optic nerve head located at the nasal-inferior corner (white arrow). The central 1 mm x 1 mm area (white square box) was used for further analysis.

All UHR-OCT images were composed of 1000 A-scans x 256 B-scans x 512 pixels. Using Eq.1.16, the one-sided maximum depth of the A-scan is ~1.1 mm which results in ~800 µm in the tissue for 1.38 tissue refractive index. Hence, Eq.1.17 gives ~3.1 µm axial pixel resolution. The lateral pixel resolution for a B-scan is ~2 µm for a 1 mm scan length on the retina and 1000 A-scans (Eq.1.18). Therefore, in a B-scan, the optical resolution will determine the resolution of the system.

Cross-sectional images of the rat retina were generated from the raw UHR-OCT data using a custom Matlab code (Mathworks). The Matlab code was originally developed in the Biomedical Imaging Lab. at University of Waterloo under Dr. Kostadinka Bizheva’s supervision and was later modified by the author. The 3D views of the imaged retinal volume were generated using Amira software. In the C-scan direction, the pixel resolution is 3.9 µm ($\frac{1000\ \mu m}{256\ B-scans}$) and will determine the resolution of the system.

A semi-automated retinal layer segmentation algorithm developed in collaboration with researchers from the Systems Design Engineering Department at University of Waterloo (Akshaya Mishra, et.al.)[135] was used to segment individual retinal layers from the UHR-OCT cross-sectional tomograms and to calculate the layer thickness and reflectivity. The contribution of the author was to discuss with the code developer what are the important features in a B-scan and what information needed to be extracted from the images. The code was written in several steps. At each step the author provided the code developer with sample data to test and discussed the results and suggested improvements.

For quantification of the changes in the retina, a 3D set of data (1000 A-scans x 256 B-scans) corresponding to a 1 mm x 1 mm area of the retinal tissue surface was selected for each time point from each rat and was used for segmentation. Equally spaced B-scans (~every 75 µm) were selected for segmentation while each B-scan was sampled at 50 equally spaced intervals (~every 24 µm) resulting in over 600 sampling points for one 3D set of OCT images of rat retina. The segmentation algorithm measures the thickness (number of pixels between two segmentation lines at the layer border) and intensity (average of the pixel values between two segmented lines) of each segmented layer at each sampling point in an individual B-scan. The total retina and PR layer values were calculated from the sum of the values from the related sub-layers at each sampling point (A-scan). The values from all the segmented B-scans in a 3D set were then used to calculate the average and the standard deviation (STD) of the thickness and reflectivity for each individual retinal layer in the imaged 3D volume.

3D sets from one of the rats were used for segmentation with finer sampling (segmented 256 B-scans in the 3D sets) and the segmented data was used to generate *en face* thickness and reflectivity maps over 3D volumes of retinal tissue demonstrating qualitatively, the spatial variations and overall time changes in the retinal morphology (chapter 5.5).

3.6 Statistical Analysis

The average and standard deviation values acquired from the segmented data for 13 animals were used for statistical analysis of the retinal layers' thickness and reflectivity. Since the statistical analysis procedures used in chapters 5 and 6 were different, the detailed description of the statistical procedure is given in each individual chapter (sections 5.4 and 6.4).

3.7 Histology

For histological examination of retinal tissue, both eyes of the animals were enucleated and fixed in freshly prepared 4% paraformaldehyde (20 min) before being rinsed with 0.1 (w/v) mM Sorenson's phosphate buffer (pH 7.5; SB; 3 x 10 min). Eyes were cryoprotected with 30% (w/v) sucrose in Sorenson's phosphate buffer overnight. The whole eyes were embedded in Optimal Cutting Temperature embedding medium, then frozen. The frozen samples where sectioned at 12 µm and sections acquired from the central retina were mounted onto clean glass slides using a cryostat and were allowed to dry before hemotoxylin and eosin (H&E) staining. Coverslips were mounted onto the slides using Permount and images were collected using a light microscope and a color camera.

Chapter 4

Spectral Shaping for Improving UHR-OCT Axial Resolution for *In Vivo* Imaging of Human and Rodent Retina in the 1060 nm Wavelength Region

This chapter is based on the following journal publication:
S. Hariri, A. A. Moayed, A. Dracopoulos, C. Hyun, S. Boyd, and K. Bizheva, "Limiting factors to the OCT axial resolution for in-vivo imaging of human and rodent retina in the 1060 nm wavelength range," *Opt Express*, vol. 17, no. 26, pp. 24304–24316, Dec. 2009. [134]

The UHR-OCT system used for this study was designed and built by Dr. Kostadinka Bizheva. She has also overseen the computational calculations, animal experiments and manuscript preparation.

Dr. S. Boyd provided the opportunity for imaging healthy rats at St. Micheal's Hospital, Toronto and made revisions to the manuscript.

C. Hyun made extensive modifications to the image acquisition program (Labview) and assisted with the processing of the raw data into dispersion compensated OCT images.

A. Dracopoulos performed the animal handling and anesthesia and observed all animal imaging sessions at St. Michael's Hospital. She also proofread the manuscript.

A.A. Moayed participated in all animal imaging sessions and assisted with the 3D data reconstruction and revisions of the manuscript.

The computational simulation of the effect of water absorption on the OCT axial resolution, testing and implementation of the modified light source, designing the water cells used to approximate the effect of water content of rat and human eyes, carrying out the animal experiments, the data processing and analysis, as well as the preparation of the manuscript are the author's work.

The author would like to sincerely thank Dr. Donna Strickland and Dr. Sebastian Marschall for their useful suggestions and guidance for improving the axial resolution calculation method used in this chapter and Dr. Melanie Campbell and Marsha Kisilak for their assistance with ANSI safety limit calculations.

The author would like to gratefully acknowledge the inkind support provided by Superlum Inc, in particular, V. Shidlovski for providing the modified light source; M. Xia, H. Van der Heide and J. Szubra for their assistance with the electronic and mechanical designs, and X. Zhao from St. Michael's Hospital, Toronto for assistance with the animal preparation. This work was supported in part by NSERC, CIHR doctoral fellowship, Ortho-Biotec (Canada) and Ontario Centers of Excellence grants and the Walter Family fund (St Michael's Hospital).

All animal experiments were conducted in accordance with animal protocols approved by the Animal Ethics Review Boards of the University of Waterloo and St. Michael's Hospital, Toronto.

4.1 Overview

A computational model was developed to evaluate the limitations to the highest axial resolution, achievable with ultrahigh resolution optical coherence tomography (UHR-OCT) in the 1060nm wavelength region for *in vivo* imaging of the human and rodent retina. The model considers parameters such as the wavelength dependent water absorption and the average length of the human and rodent eyes. A custom-built light source with re-shaped spectrum was used to verify experimentally the results from the computational model. Axial OCT resolution of 4.2µm and 7µm was measured from a mirror reflection with the custom light source by propagating the imaging beams (both sample and reference) through water cells with 5 mm and 25 mm thickness, corresponding to the average axial length of the rodent and human eye respectively. Assuming an average refractive index of 1.38 for retinal tissue, the expected axial OCT resolution in the rodent and human retina is 3 µm and 5 µm respectively. Retinal tomograms acquired *in vivo* from the rat eye with the modified light source show clear visualization of all intra-retinal layers, as well as a network of capillaries in the inner- and outer plexiform layers of the retina.

4.2 Introduction

OCT imaging in the 1060 nm wavelength region has recently gained popularity for ophthalmic applications due to the fact that it offers multiple advantages as compared to retinal imaging at shorter wavelengths. Specifically, water, which comprises most of the ocular tissue (cornea, aqueous, vitreous, lens and retina), has a local absorption minimum at ~1060 nm, while light scattering from biological tissue decreases with longer wavelengths. In addition, the maximum permissible power for safe retinal imaging at this region is higher than that of the 800nm region[60]. The higher allowable optical power, combined with the reduced scattering and absorption from melanin in the retinal pigmented epithelium (RPE) at longer wavelengths results in deeper image penetration and better visualization of the choroidal structure and vasculature[25], [51], [56], [62], [136]–[144]. Moreover, the water dispersion is zero for ~1 µm at 37ºC temperature[31]. However, as we tend to use ultra-broadband spectra to improve the axial OCT resolution, dispersion plays a stronger role in longer eyes because of the water content of the eye between the corneal surface and retina. There is then an imbalance between the chromatic dispersion in the sample and reference arms which can have a negative effect on the achieved axial resolution. This is especially important in *in vivo* human UHR-OCT retinal imaging due to the longer axial eye length (~25 mm).To overcome this problem, it is important to properly match the water dispersion in sample and reference arms. Any residual dispersion can be corrected with post processing dispersion compensation algorithms[16], [29], [30].

Visualization of sub-retinal structure and the blood vessel network are of particular diagnostic value, since diseases such as “wet” and “dry” age-related macular degeneration (AMD) are characterized by penetration of abnormal choroidal blood vessels through the RPE (wet AMD) and formation of drusen between the RPE layer and the Bruch’s membrane (dry AMD)[43]. The reduced scattering coefficient of ocular tissue at 1060 nm as compared to 800 nm has the additional advantage of providing retinal images with significantly better quality in patients with corneal haze or cataracts[56].

Retinal OCT imaging in the 1060 nm wavelength region also has the potential for non-invasive probing of light induced physiological changes in the retina, since retinal photoreceptors are not sensitive to light >900 nm[63], [145], [146]. Considering the fact that the early stages of retinal diseases are characterized by abnormal function of retinal cells, the ability to image *in vivo* and non-invasively measure physiological changes in human and animal retinas and to correlate them with structural abnormalities, can further our understanding of the origins and development of retinal diseases. Such optophysiological recordings have the potential to evolve into a powerful clinical diagnostic and monitoring tool.

Although OCT retinal imaging at 1060 nm offers multiple advantages, development of high speed, high axial resolution OCT systems for this wavelength range poses a number of technological challenges. Specifically, axial OCT resolution is primarily determined by the spectral bandwidth and the central wavelength of the light source used (Eq.1.4), while the image acquisition speed is related to the reference mirror velocity (time domain OCT – TdOCT)[34], [147], the data transfer rate of the camera (spectral domain OCT – sdOCT)[148], [149] or the frequency sweep rate of tunable lasers (swept source OCT – ssOCT)[146]. It is also worth noting that the lateral resolution is also negatively affected by the longer central wavelength of the 1060 nm region compared to the standard 800 nm region (Eq.1.5).

The first experimental demonstration of the advantages of retinal imaging in the 1060 nm wavelength region was accomplished with TdOCT[136], where porcine retinal samples were imaged *ex vivo* with axial OCT resolution of 2.8 µm in retinal tissue and image acquisition speed of ~0.01 frames/s (20 A-scans/s). Later on, improved image penetration into the choroid was demonstrated *in vivo* in human retina[137] with TdOCT, with OCT axial resolution of ~7 µm in retinal tissue and image acquisition rate of 150 A-scans/s.

Recent advances in CCD and tunable laser technology have lead to significant improvement of the image acquisition rate of retinal OCT systems operating in the 1060 nm wavelength region, specifically, up to 47 kHz[51] and 92 kHz[21], [22] for sdOCT and 249 kHz[25], 400 KHz[26] and 1.37 MHz[27] for ssOCT. By employing broad bandwidth continuous wave light sources and tunable lasers with spectral outputs centered in the range of 1020 nm – 1040 nm, high axial resolutions of 7 µm[150], 5.3 µm[26], and 5.7 µm[51] were achieved *in vivo* in human retinas with sdOCT systems.

Until recently, it was generally accepted that the local peak at ~980 nm and the fast rise beyond 1120 nm in the water absorption profile[58], [59] defines an optical "window" (see Fig.4.1A, grey line), which limits the effective spectral bandwidth transmitted through the anterior part of the eye to the retinal surface. The full width at half maximum (FWHM) of this optical window is ~100 nm, centered at ~1060 nm, which effectively limits the OCT axial resolution in human retina to ~3.6 µm. This value is a theoretical estimate, since in practice the spectral transmission characteristics of the optical and fiberoptic components of the imaging system, along with the spectral efficiency of the detector can reshape the input optical spectrum and effectively reduce the measured axial OCT resolution.

This study aimed to a) determine if spectral reshaping of the input optical spectrum can overcome at least partially the retinal OCT resolution limitations imposed by the water absorption profile in the 1060 nm wavelength range; and b) investigate the practical limits to the highest OCT axial resolution achievable *in vivo* in human and small animal retinas, by considering spectral reshaping and the OCT system design. For the purpose of this study a simple computational model was developed and experiments were conducted to verify the theoretical results in practice. The outcome of this study could serve as an insight and a guideline to research groups and companies developing CW or tunable light sources for high resolution ophthalmic (retinal) sdOCT and ssOCT systems operating in the 1060 nm wavelength range.

4.3 Results

4.3.1 Computational Results

Fig.4.1 shows the spectral shape, bandwidth and power losses for an input spectrum of Gaussian shape, centered at 1060 nm with a spectral bandwidth of 200 nm as propagating through water cells with thickness equivalent to the length of the human or rodent eye. Fig.4.1A shows an overlay of the input spectrum (black line) and the water absorption profile (grey line).

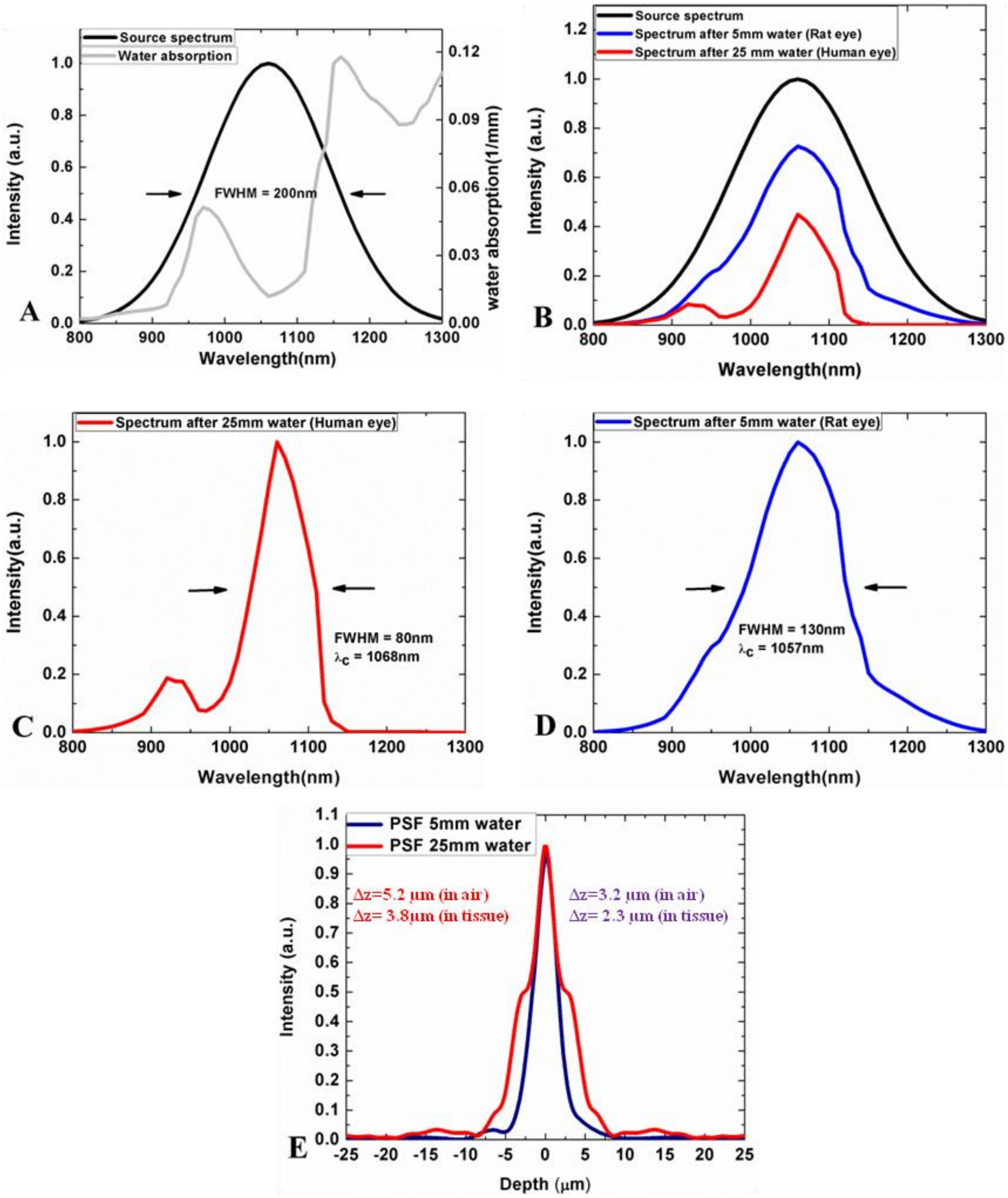

Fig.4.1 Graphical representation of the spectral shape, bandwidth and power losses due to water absorption, calculated for a double pass of the imaging beam (black line) through water layers of 5 mm (blue line) and 25 mm (red line), corresponding to average lengths of a human and rat eye respectively. (A) Gaussian shaped input spectrum with 200 nm spectral bandwidth, centered at 1060 nm and the water absorption profile (grey line). (B) Comparative spectral power losses. Spectral shape and bandwidth changes, and theoretical values for the corresponding OCT axial resolution in the retina for the case of 25 mm (C) and 5 mm (D) thick water layers. Comparison of the PSFs (E) computed by Fourier transforming the spectra shown in (C) and (D). (Figure reproduced with modifications from [134]with permission from the journal)

Comparison of the overall shape and power losses resulting from double pass propagation of the input beam through 5 mm (blue line) and 25 mm (red line) water layers is shown in Fig.4.1B. Total power loss of 80% and 46% was computed for the case of 25 mm and 5 mm thick water layers respectively, by integrating over the spectral intensities below the curves in Fig.4.1B.

Fig.4.1C shows that water absorption in a human eye of 25 mm average length limits the maximum useful spectral bandwidth of the imaging beam to ~80 nm, corresponding to OCT axial resolution of ~3.8 µm in the retina. In the case of the much smaller rodent eye, the useful imaging bandwidth is reduced to ~130 nm (Fig.4.1D), corresponding to axial OCT resolution of ~2.3 µm in the rat retina. The spectra shown in Fig.4.1C and 4.1D were Fourier transformed (as explained in chapter 3.2) to determine the effect of the non-Gaussian shape of the water affected spectra on the resulting PSFs (Fig.4.1E).

Achieving axial OCT resolution < 3µm in the human retina at ~1060 nm, comparable to the highest resolution demonstrated previously with research grade OCT systems operating at ~800 nm, may be possible by expanding the usable spectral bandwidth around 1060 nm by reshaping the spectrum of the incident imaging beam. Numerical spectral reshaping has been used in the past to suppress the appearance of sidelobes in the OCT PSF[151]. The question is: could this method be used to predict the ideal light source spectral shape for specific applications (i.e. *in vivo* human or animal retinal imaging) to improve the axial resolution? To test the idea of spectral reshaping, the example Gaussian input spectrum (Fig.4.1A, black line) was multiplied by an inverse function of the water absorption (Fig.4.1A, grey line) and the inverse function of the camera spectral efficiency (Fig.3.3) to generate the reshaped input spectra for the two cases of 25 mm water layer (Fig.4.2A, black line) and 5 mm water layer (Fig.4.2B, black line). By applying the re-shaped input spectra to the computational model described above, an axial resolution of 1.8 µm, corresponding to spectral bandwidth of 200 nm centered at 1060 nm, can be achieved theoretically in the human or the rat retina. In other words, using light sources with the spectral shape shown in Fig.4.2A and Fig.4.2B for 25 mm and 5 mm water cells respectively, will result in a final Gaussian spectrum (Fig.4.1A) with 200 nm FWHM yielding 1.8 µm axial resolution in tissue.

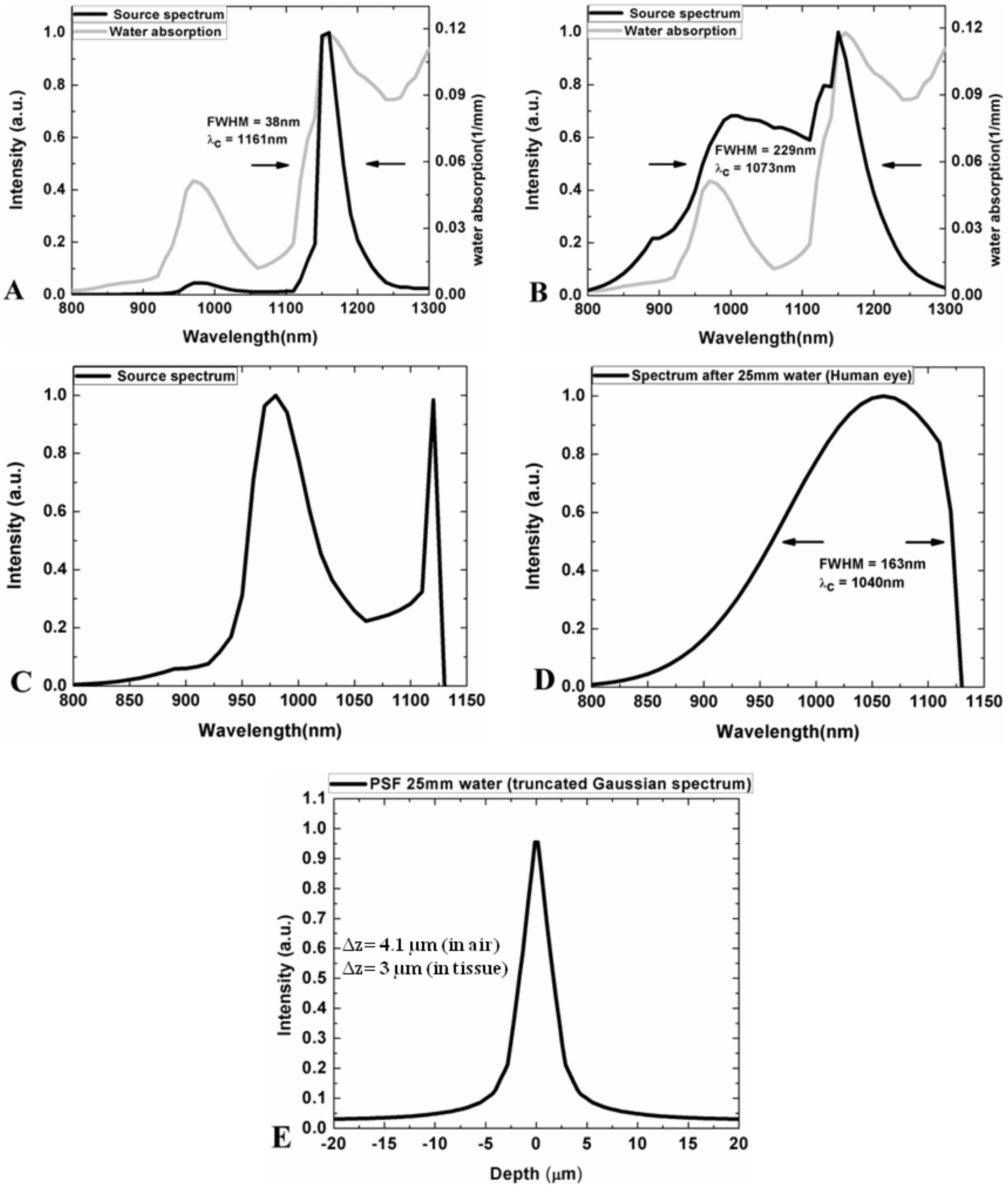

Fig.4.2 Reshaped input imaging spectra for the (A) 25 mm (human, black line) and (B) 5 mm (rat, black line) thick water layers described in the computational model. The reshaped spectra were generated by multiplying the original Gaussian input spectrum from Fig.4.1A with an inverse function of the water absorption (Fig.4.1A) and the inverse function of the camera spectral efficiency (Fig.3.3). The figure shows the major limitation (power loss) to achieving the theoretical axial OCT resolution of 1.8 µm in the human retina. Truncated input spectrum (C), the corresponding spectrum after 25 mm water for the human eye (D) and its axial PSF (E). (Figure reproduced with some modifications from [134] with permission from the journal)

The computational results shown in Fig.4.2A and Fig.4.2B, also demonstrate the major difficulty with achieving the theoretical resolution in practice. Due to the sharp increase of water absorption (grey line) for wavelengths longer than 1120 nm, more than 95% of the input power of the reshaped spectrum for the human eye (25 mm water layer, Fig.4.2A) is contained in a fairly narrow spectral range (1150 nm – 1200 nm), corresponding to the tail of the detected Gaussian shaped spectrum.

Since in the case of OCT imaging of the human retina at ~1060 nm, the safety guidelines of the ANSI standard[60] limit the spectral power incident on the cornea to 3.2 mW for 5 min exposure to the scanning beam and 2.0 mW for 10 s for a stationary beam should the scanners fail, the power reaching the retina is not sufficient for obtaining high contrast images of the retina and for imaging choroidal blood vasculature. In the case of the rodent eye, the power losses attributed to water absorption are significantly smaller (~50%), therefore achieving an axial OCT resolution of 2 µm or better in the rat retina is limited by the availability of light sources with spectra close to the theoretical one shown in Fig.4.2B and the design of the OCT system, capable of sustaining that spectrum. However if the ANSI standard for the scanning beam were corrected for the f# of the rat eye giving greater image irradiance on the retina, the ANSI limit becomes 0.6 mW for a 5 min, scanning beam exposure, also causing lower contrast images. One way to achieve improvement in the axial OCT resolution in the human retina within the power guidelines of the ANSI standard, is to truncate the long wavelength end of the input spectrum (Fig.4.2A) at 1120 nm to limit the total power at the cornea which results in the spectrum shown in Fig.4.2C. The resulting spectrum after double pass through 25 mm water is a truncated Gaussian showed in Fig.4.2D. In this case the spectral bandwidth is limited to ~160 nm and the central wavelength is shifted to 1040 nm, which results in ~3 µm axial OCT resolution in the human retina (Fig.4.2E) but a slightly lower ANSI limit (2.9 mW for scanning beam).

4.3.2 Experimental Results

To demonstrate experimentally that spectral re-shaping of the incident imaging beam can lead to improvement in the OCT axial resolution for retinal imaging at ~1060 nm, the spectral output of a commercially available SLD based light source (Superlum Inc.) was modified to increase the spectral power at ~980 nm where water absorption has a local maximum. The original light source was comprised of two SLDs with partially overlapping spectra and power outputs selected to result in a nearly Gaussian shaped spectrum of the light source (Fig.4.2A, black line). The original SLD was modified with assistance from Superlum to increase the power output of the shorter wavelength SLD, which was centered at ~980 nm, overlapping with the water absorption peak. The spectral shape of the modified light source is shown in Fig.4.3A (red line), and the total power output of the source was ~10 mW. Note that the spectra shown in Fig.4.3A are the spectra of the original and modified light sources measured at the detection end of the sdOCT system with a silver mirror used as a sample in the imaging arm of the system. Therefore, this measurement automatically accounts for any spectral losses related to the transmission bandwidth of all optical and fiber optic components in the sdOCT system, as well as the spectral sensitivity of the CCD camera. The graphs in black and red colors in Fig.4.3B and Fig.4.3C show the spectra measured at the detection end of the sdOCT system with the original and modified light sources, for water cells of 5 mm and 25 mm thickness respectively, inserted in both the sample and the reference arms of the OCT system before the mirror. Fig.4.3D and Fig.4.3E show the measured axial PSFs of the sdOCT system for the spectra shown in Fig.4.3B and Fig.4.3C. In the case of the 5 mm water cell, 4.2 μm axial resolution was measured in air with the sample mirror, which corresponds to 3 μm axial resolution in the rat retina assuming an average refractive index of 1.38 for retinal tissue in the 1060 nm wavelength range. This constitutes about ~30% improvement of the axial OCT resolution in the rat eye as compared to the one achieved with the non-reshaped spectrum of the standard, commercially available light source[51]. In the case of the 25 mm water cell, the measured resolution from the mirror reflection was ~7 μm, corresponding to ~5 μm imaging resolution in the human retina, assuming an average refractive index of 1.38 of retinal tissue. In this case, spectral re-shaping of the SLD based light source improved the axial OCT resolution by about ~12% as compared to previously published results[51]. The axial PSF can also be calculated by performing FT on the cross-correlation of sample and reference spectra. Figures 4.3F shows the calculated axial PSFs in the case of 5 mm water cells in both sample and reference arms . The resulting axial resolutions in air are 4.6 μm and 5.6 μm for the modified and regular SLDs respectively. For 25 mm of water, the calculations result in 6.3 μm and 7.2 μm for modified and regular SLDs respectively (Fig.4.3G). These values are close to the measured axial resolutions.

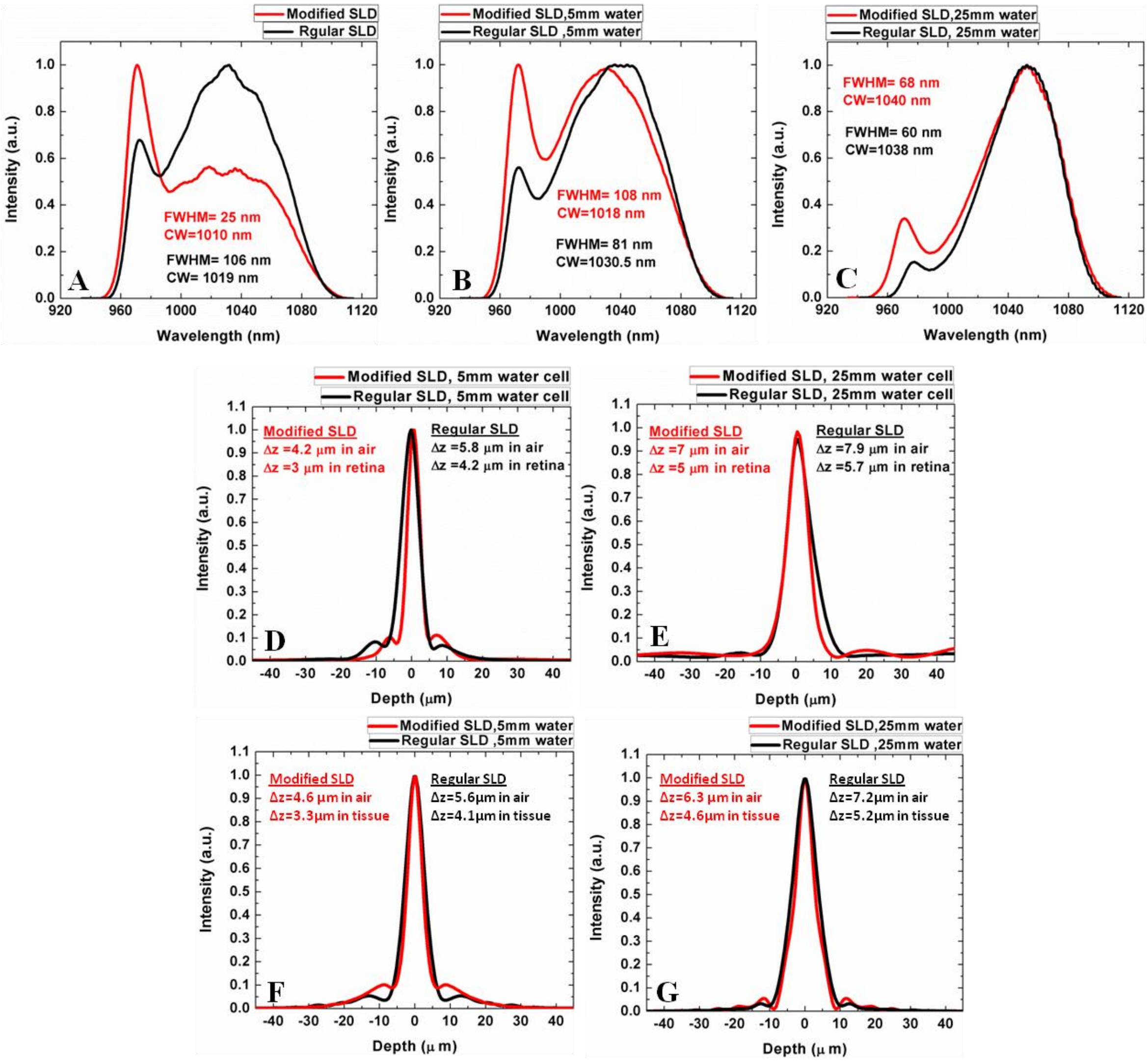

Fig.4.3 Spectra of the original and modified SLD based light sources measured at the detection end of the SD-OCT system from a mirror reflection in the sample arm (A). Spectra of the original and modified SLD based light sources measured after a double pass of the imaging beam through a 5 mm (B) and 25 mm thick (C) water cells. PSFs measured with the sdOCT system with the two light sources and with 5 mm (D) and 25 mm (E) water cells in both arms of the imaging system. Calculated PSFs from cross-correlation of sample and reference arms with 5 mm (F) and 25mm (G) water cells inserted in both sample and reference arms of the OCT system. (Figure reproduced with modifications from[134] with permission from the journal)

The experimentally measured axial resolutions (Fig.4.3D and E) are within 10% from the values calculated from the reference and sample spectra (Fig.4.3F and G). This difference is most likely due to the fact that the spectra and PSFs were acquired on different occasions possibly with slightly different experimental conditions such as polarization mismatch between the reference and sample arms of the interferometer, chromatic aberrations of the focusing lenses and precision of the positioning of the mirror in the sample arm during the axial resolution measurements.

To demonstrate experimentally the effect of the high axial OCT resolution on the image quality, OCT tomograms were acquired *in vivo* from the retinas of Long Evans rats. The imaging procedure and data processing was performed as explained in previously in chapters 3.3 and 3.4. Figure 4.4 shows representative 2D and 3D images of healthy rat retinas acquired *in vivo* with the reshaped spectrum. The images were acquired at 47 kHz with 1.6 mW power of the optical beam incident on the rat cornea and 99 dB sensitivity. The image size is 1000 A-scans x 220 pixels.

The image in Fig.4.4A was acquired away from the optic disc and shows clear visualization of all intra-retinal layers, cross-sections of blood vessels in the underlying choroid and part of the sclera. The image in Fig.4.4B was acquired from the area around the optic disc and shows a cross-section of the remains of the hyaloid blood vessel (HV). The small black circular features observed in the inner- and outer plexiform layers of the rat retina in both images correspond most likely to reflections from red blood cells (about 6 µm in diameter) in the tiny capillaries.

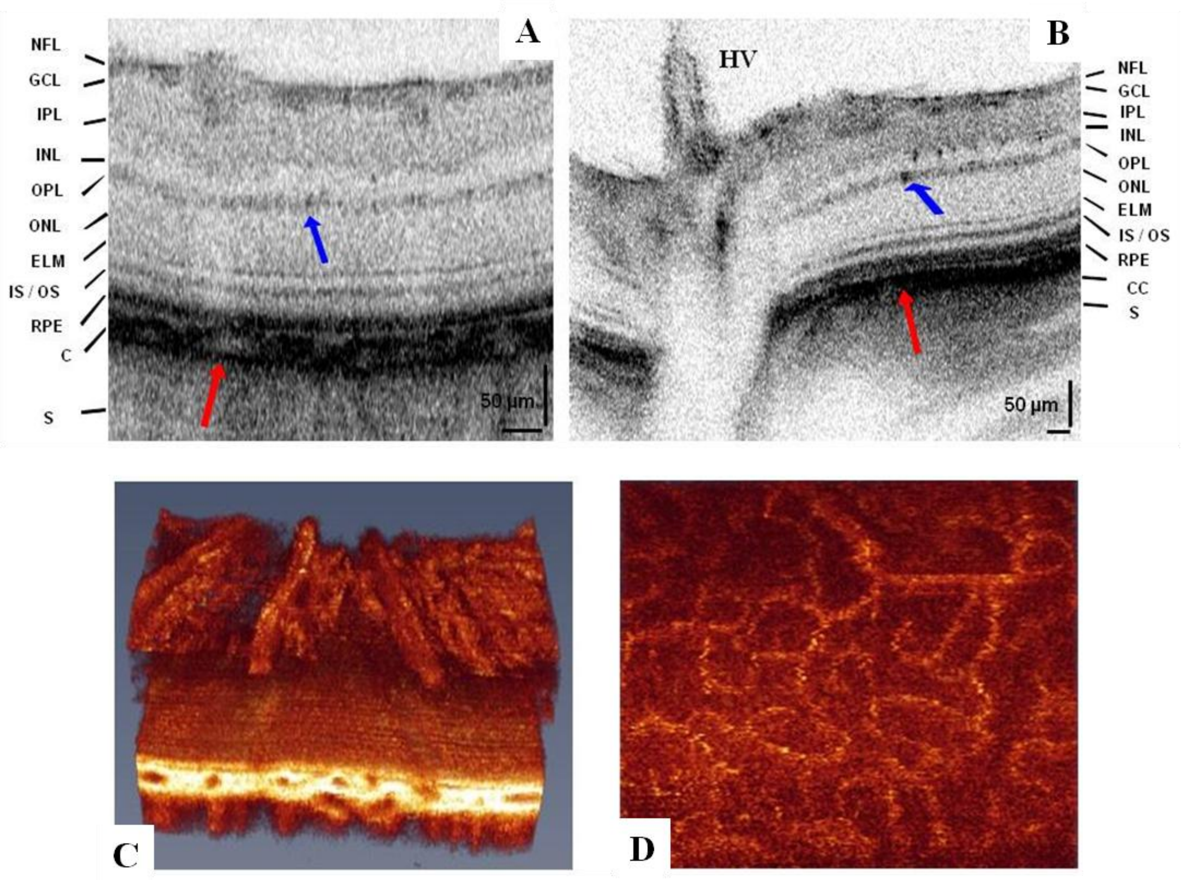

Fig.4.4 Two-dimensional images of rat retina acquired *in vivo* away from the optic disc (A); and at the optic disc (B). Image dimensions are 1000 x 220 pixels. Both images show clear visualization of all retinal layers, as well as the cross-sections of multiple choroidal vessels marked with red arrows. Cross-sections of capillaries located at the inner plexiform (IPL) and outer plexiform (OPL) layers are distinctly visible on both images and marked with blue arrows. Fig.4.4B shows the remains of the hyaloids vessel (HV). Fig.4.4C shows a representative 3D stack of 172 B-scans of the rat retina. Fig.4.4D shows an *en-face* cross-section of the retina obtained from the 3D stack at the location of the outer plexiform layer of the retina. The en-face image shows the intricate network of capillaries, that correspond to the highly reflective black spots in observed in the 2D retinal images (blue arrows). NFL: nerve fibre layer, GCL: Ganglion cell layer, IPL: inner plexiform layer, INL: inner nuclear layer, OPL: outer plexiform layer, ONL: outer nuclear layer, ELM: external limiting membrane, IS/OS: inner segment outer segment junction, RPE: retinal pigment epithelium, C: choroid, S: sclera. (Figure reproduced from[134] with permission from the journal)

To determine the effect of the improved axial OCT resolution on the image quality, OCT tomograms were acquired with the original and the modified light source at approximately the same location in the rat retina of the same animal. Representative images are shown in Fig.4.5.

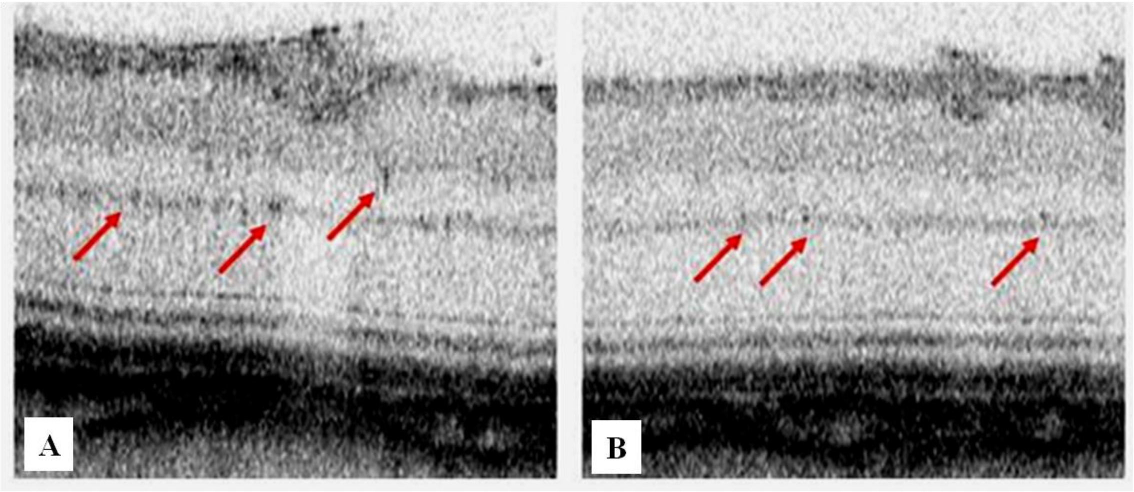

Fig.4.5. Comparison of retinal OCT tomograms acquired with the original (A) and the modified (B) SLD based light source. The image acquired with the modified light source shows slightly better visualization of the boundaries of the inner retinal layers, as well as better definition of the reflections from retinal capillaries (red arrows). (Figure reproduced from[134] with permission from the journal)

Visual comparison of the two images shows that the one acquired with the modified light source (Fig.4.5.B) offers slightly better delineation of the retinal layer boundaries and decreased apparent size of the highly reflective spots that correspond to reflections from retinal capillaries (red arrows). This improvement in Fig.4.5B compared to Fig.4.5A is most likely due to the resolution improvement effect where the axial PSF of the image in the latter is narrower than that of the former, resulting in finer appearance of the capillaries in the OCT tomogram acquired with the modified SLD (Fig.4.5B). Since the experimental improvement of the axial OCT resolution in this case was limited to only ~30% due to technical difficulties of building a light source with spectral output close to the one suggested by the theoretical model, and given the size of morphological features in the rat retina, dramatic changes in the image quality of the retinal tomograms were not expected. Future development of light sources based on the model presented here, could potentially generate 2 µm axial OCT resolution in the rat retina, which will constitute of factor of 2x resolution improvement as compared to recently published results[51]. However the maximum permissible power for safe retinal imaging will pose severe restrictions to the image contrast.

The diffraction limited lateral resolution in the rat retina is calculated via Eq.1.5 which yields ~3.2 µm in retina for the 1.2 mm size of the imaging beam used in this study. However, this diffraction limited value can be improved by increasing the pupil size and reaches 1.3 µm for a 3 mm pupil size, 1020 nm central wavelength and the typical 300 dioptre power of the rat eye when the aberrations are corrected using adaptive optics. Hence, by using a combined OCT and adaptive optics (AO) system, diffraction limited lateral resolution of bellow 2 µm can be achieved in the rat retina that would allow for resolving adjacent photoreceptor cells (~2 µm separation[152]) .

4.4 Discussion

Results from the computational model (Fig.4.1C) show that the use of a Gaussian shaped spectrum in the imaging beam of an sdOCT system designed for retinal imaging at 1060 nm, and the water absorption profile in this wavelength range ultimately limit the maximum achievable axial OCT resolution to ~4.5 µm in the human retina. Theoretically, reshaping of the OCT spectrum incident on the human cornea can improve the axial OCT resolution in human retina (Fig.4.2C and 4D). However the extent of the reshaping is limited by the maximum permissible exposure limit defined by the ANSI standard [60]. For the spectral range 900 nm – 1200 nm, 7 mm limiting aperture and 10 s continuous exposure, the ANSI limit for the power incident on the human cornea is 2.0 mW. Previous studies[51] conducted with a commercially available SLD based light source (same as the basic SLD unit used in the current study before the modification) have shown that 5.7µm axial OCT resolution can be achieved in the human retina with imaging power of < 1 mW at the cornea. In this study, an improved axial resolution of 5 µm was shown for a 25 mm water cell corresponding to the water content of the human eye (please refer to Appendix A for more results in human OCT imaging). According to the computational model, a reshaped spectrum similar to the one presented in Fig.4.2C could theoretically result in ~3 µm axial OCT resolution in the human retina. However, calculations show ~80% power loss due to water absorption and hence need for increased input power to acquire high contrast images. Further truncation of the shorter wavelength end of the reshaped spectrum (truncating the spectrum shown in Fig.4.2C), or partial magnitude reduction of the peak at ~980 nm could lower the imaging power incident on the cornea at the expense of degrading the axial OCT resolution in the human retina. In the case of imaging the rat retina, use of spectral reshaping offers theoretically and experimentally, significant improvement as compared to previous studies conducted with a commercially available SLD[51].

Due to the higher NA of the rat eye which results in smaller spot size on the retina and the shorter axial length which leads to less water absorption, the irradiance at the retinal tissue for each C-scan is higher in the rat retina as compared to the human retina by a factor of the ratio of the two f# squared (where f# is the ratio of the focal length to the pupil diameter). This suggests the need for more conservative use of the input power in rat eye, for which the limit for the 1mm by 1mm scan at a 1020 nm central wavelength would be 0.5 mW for 5 min. The imaging beam power used in this study was 1.6 mW at the cornea above this corrected ANSI standard. In this study, the allowed modifications to the SLD unit limited the imaging power incident on the rat cornea to 1.6 mW and the spectral modifications only to the shorter wavelength end of the SLD spectrum. ~30% improvement of the axial OCT resolution in the rat retina was achieved with these spectral modifications. Future development of light sources with properly shaped emission spectra could potentially allow the achievement of ~2 μm axial OCT resolution in the rodent retina, close to the theoretical limit predicted in this study (Fig.4.2B) but the scanning area would need to increase or the spectrum would need to be centered at a longer wavelength to meet the corrected ANSI standard. The high axial OCT resolution can improve the contrast of small features in the rodent retina, for example the small capillaries in the plexiform layers, as well as the sharpness of the retinal layer boundaries in the OCT images. The last feature is directly related to the precision and optimal performance of layer segmentation algorithms and the accurate thickness measurement of individual retinal layers, which can serve as a biomarker of developing retinal diseases. Furthermore, if the sdOCT system is combined with an adaptive optics (AO) system, diffraction limited lateral resolution of bellow 2 μm can be achieved in the rodent retinas due to the shorter focal length of these animal’s eyes. Such imaging resolution could potentially allow for visualization of individual photoreceptors in 3D, which would be of significant interest to researchers studying neurodegenerative disease models in small animals.

The strong attenuation of the optical imaging power in the human eye resulting from water absorption in the vitreous and the anterior chamber will also have a detrimental effect on the contrast and image penetration depth of retinal OCT tomograms. Assuming an average water absorption coefficient of 0.04 mm^{-1} for the spectral range of 950 nm – 1130 nm, a double pass of the optical beam through a human eye of 25 mm average length, would result in ~9 dB loss of SNR which could significantly affect the OCT image contrast and penetration depth into the choroid. In the case of small animal eye (for example rodents) imaging, the SNR loss due to water absorption will be in the order of 2 dB, which should not affect significantly the contrast or image penetration depth of 1060 nm OCT retinal tomograms. This is clearly demonstrated by the rat retina images acquired with modified light source.

The simple computational model described in this manuscript can serve as a guideline for future design of novel light sources, targeted to improve the axial OCT resolution of ophthalmic OCT systems, designed for imaging the human or animal retina in the 1060 nm wavelength range. Although the model was tested experimentally with a sdOCT system, improvement of the axial OCT resolution in retinal imaging through spectral reshaping is feasible both in TdOCT and ssOCT. It is important to note that other factors such as the spectral efficiency of the detector (whether it is a single photodiode, a dual balanced detector or a linear array CCD), as well as the spectral characteristics of all optical and fiber optic components in the imaging system will further modify the emission spectrum of the light source, as it propagates through the system. These modifications can have positive or negative effects on axial OCT resolution. Extending the spectrum of the input imaging beam to < 900 nm can result in multimodal light propagation through the fiber based OCT system, which can have a detrimental effect on the OCT axial resolution and SNR. Furthermore, as shown in Fig.3.3 the InGaA detector efficiency drops sharply for wavelengths shorter that 960 nm (e.g. 50% for 920 nm vs. 80% for 960 nm) hence, it is better to move the spectrum's central wavelength further away from 900 nm and closer to 1100 nm to use the maximum detector sensitivity and gain a more uniform camera efficiency over the spectrum. On the other hand, extending the spectrum beyond 1120 nm will result in significant power loss due to increased water absorption. Therefore the optimal wavelength range to work with is between 950 nm and 1120 nm. In the OCT system used for the experimental verification of the computer model, fibers with cut-off wavelength of 905 nm were used and the shorter wavelength end of the spectrum of the modified SLD light source was located at ~950 nm. If the exact spectral characteristics of some of the OCT system components are known *a priori*, they can be included in the computer model for better guidance of the final design of the desired light source spectrum. In this study, the spectral efficiency of the InGaAs CCD camera was included in the computational model as explained earlier in this chapter as well as in chapter 3.2. Other factors, for example the spectral transmission of fiber couplers or fiberoptic isolators are polarization dependent, therefore, their influence on the final detected spectrum can only be approximated in the proposed computer model.

4.5 Conclusions

Improving the axial resolution of ophthalmic UHR-OCT systems designed for retinal imaging in the 1060 nm wavelength range is a key factor to resolution of adjacent small morphological details or the improved contrast of small features in the human or animal retina that can be associated with diagnostic or therapeutic markers of many retinal diseases. Furthermore, the high axial resolution will improve the precision of segmentation algorithms designed for thickness measurement of individual retinal layers. In this chapter, the effectiveness of spectral shaping as a method for improving the axial resolution in the retina of UHR-OCT systems designed for the 1060 nm wavelength region was proposed and tested. Results from this study not only establish the theoretical and practical limits to the highest axial OCT resolution achievable at 1060 nm, but also can serve as a guideline for development of novel light sources for UHR-OCT at 1060 nm.

Chapter 5

Long-Term Effect of Sodium Iodate Toxicity in a Rat Model of Outer Retina Degeneration Imaged *In Vivo* with Ultrahigh Resolution Optical Coherence Tomography

This chapter is based on the following journal publication:

S. Hariri, A. A. Moayed, V. Choh, and K. Bizheva, "In vivo assessment of thickness and reflectivity in a rat outer retinal degeneration model with ultrahigh resolution optical coherence tomography," *Invest. Ophthalmol. Vis. Sci.*, vol. 53, no. 4, pp. 1982–1989, Apr. 2012.[154]

The UHR-OCT system used for this study was designed and built by Dr. Kostadinka Bizheva. She has also overseen the experiments, the data analysis and the manuscript preparation and made revision to the text.

Dr. V Choh has taught the author tissue preparation, H&E staining, preparation and imaging histological cross sections. She has also supervised the statistical analysis of the data used in this manuscript and made revisions to the text including the method sections regarding the histology and statistics as well as the results and discussion sections.

A.A.Moayed assisted with the animal handling and imaging, data processing, 3D data reconstruction and revisions of the manuscript.

Design and testing of the imaging probe used for imaging the rat retina, design and conducting the animal experiments, OCT image processing, active participation in development and modification of the segmentation algorithm (developed by Akshaya Mishra, [135]), statistical analysis of the thickness and reflectivity data, tissue preparation, H&E staining and imaging of the histological cross sections, as well as preparing the manuscript are the author's work.

The author would like to sincerely thank Dr. Hutchings and Dr. Campbell for their useful advice and assistance with improving the statistical analysis methods used in this chapter.

The author would like to gratefully acknowledge Dr. Shelley Boyd. St. Michael's Hospital, Toronto, and Dr. Melanie Campbell, University of Waterloo, for helpful discussions about the $NaIO_3$ retina degeneration model, Akshaya Mishra for development of the segmentation code, Donghyun Lee and Eun Sun Song for assistance with the image processing and segmentation, Nancy Gibson for her instructions in animal handling and injections, assistance with animal care and tail vein injections.

All animal procedures were conducted in accordance with the regulations of the University of Waterloo Animal Care Committee and in compliance with the ARVO statement for ethical use of animals in ophthalmic and vision research.

5.1 Overview

The high speed, UHR-OCT system described in the previous chapter was used for *in vivo* longitudinal assessment of long-term (up to 3 months) effect of sodium iodate retinotoxin on the rat retina.

Outer retinal degeneration was induced in 4 female Long Evans rats via tail vein injection of sodium iodate (40 mg/kg). Changes in the thickness and optical reflectivity of individual retinal layers were extracted using the semi-automatic segmentation algorithm (see chapter 3.5) and were assessed *in vivo* at 6 hours, days 1, 3 and 7 and up to 3 months post-injection with UHR-OCT. H & E histology was used to confirm the morphological changes observed in the UHR-OCT images.

UHR-OCT tomograms showed progressive structural damage in the rat retina over time, such as swelling, thinning, complete disintegration of individual retinal layers and clustering of highly reflective cellular debris. Photoreceptor layer swelling was observed 6 hours post-injection of sodium iodate, followed by progressive structural decomposition of the outer retina. At 3 months post-injection, the outer retina was completely disintegrated and the inner nuclear layer (INL) was in direct contact with the choroid. Changes in the reflectivity of individual retinal layers were observed over time and correlated well with the morphological changes.

5.2 Introduction

As mentioned previously (chapter 2.3), sodium iodate is a retinotoxin that is used in animal models to induce outer retinal degeneration[106], [107], [114]–[117], [120], [124], [131]. This compound is known to selectively affect the RPE cells as the primary site of damage[107]. Since normal RPE function is essential for PR survival, PR functional and structural degradation follows the RPE degeneration. Until recently, all reported studies that investigated the morphological effects of sodium iodate on different retinal layers have been conducted *ex vivo* using histological and immunohistochemical methods. In these longitudinal studies, retinas were evaluated both qualitatively and quantitatively for morphological changes at different time points after drug administration. The quantitative data was acquired by manual thickness measurement of different layers along with the number count of nuclei rows in the outer nuclear layer (ONL)[117]. Although histology and immunohistochemistry provide sub-cellular level resolution images of the retinal structure and very valuable information as to retinal physiology and biochemistry, these methods have a common disadvantage - they require termination of multiple animals at each time point of a longitudinal study to allow for statistical evaluation of the research results, and do not permit *in vivo* examination of the retinal structure, function or physiology.

Compared to other optical imaging techniques such as fundus photography and scanning laser ophthalmoscopy (SLO), UHR-OCT provides, in real-time, cross-sectional morphological tomograms of the retina that permit morphometric analysis in terms of individual layer thickness and shape. Furthermore, UHR-OCT can provide information about the optical properties of biological tissue in terms of wavelength-dependent absorption and scattering that can be used to infer information regarding retinal biochemistry[155]–[157]. This additional information could be useful in retinal degeneration studies as a non-invasive tool for investigating cell death *in vivo*, since it has been demonstrated recently that cell apoptosis and necrosis cause changes in the tissue optical reflectivity[158], [159]. In a recent study, UHR-OCT was used for *in vivo* quantification of the reflectivity of retinal layers in healthy human retina[144]. Over the past decade UHR-OCT has been used to image both human retina[36], [38] and rodent retina[50], [51], [53]–[55], [160] in health and in disease.

Preliminary results from the OCT imaging of outer retina degeneration in rats caused by sodium iodate were published previously by our group for the first time. Retinas were imaged at baseline, day 3 and day 7 post IV sodium iodate injection and results were compared with the retinal electrical activity recorded by electroretinography (ERG) showing severe damage to both retinal structure and electrical function[161].

In this study the high speed UHR-OCT system and a semi-automatic layer segmentation algorithm were used to image *in vivo* and quantify morphological changes in the rat retina in a longitudinal study of long-term effect of sodium iodate-induced outer retinal degeneration.

5.3 Study Procedure

Ten 11-16 weeks old animals were used for this study. Four rats were imaged before drug administration (baseline) as well as at 6 hours, on days 1, 3, 7 and at months 1, 2 and 3 post sodium iodate injection (IV, 40 mg/kg). Three rats were imaged as the control group at baseline and 1, 2 and 3 months post vehicle injection. Additional three rats were injected with the drug,imaged and then euthanized, one at baseline (before drug administration), one at day 7 and another one at month 3 post drug injection for histological processing to confirm the morphological changes observed in the UHR-OCT images. All the OCT measurement sessions were conducted within the 2 hour time interval from 12 pm to 2 pm to minimize the potential effect of diurnal variations in the tissue thickness and reflectivity in this study.

5.4 Statistical Analysis

The average values for individual layers acquired from the segmented 3D data sets (chapter 3.5) were used for statistical analysis. Due to the occurrences of rats not cooperating in the long-term study, the missing data module of the statistical package (SPSS v16) was used to impute 5 missing values (out of the total 32 values: 4 animals and 8 time points for each animal). For the statistical analysis of the thickness and reflectivity data, one-way repeated measures ANOVAs on the values were used to determine changes in each retinal layer as a function of time (significant changes, $p \leq 0.05$). Bonferroni-corrected multiple comparison tests were used as the post-hoc test. The significance threshold (α value) was corrected for the pairwise comparisons according to the Bonferroni correction criteria base on the number of pairs tested (significant changes, $p \leq \alpha$, α=0,05/n, for n pairs).

Unfortunately, since the control study was not performed at all time points (only done at baseline, months 1 ,2 and 3), the comparison of the control and experiment group in the statistical analysis was not possible. Hence, independent tests were performed on these two groups.

5.5 Results

Representative UHR-OCT cross-sectional tomograms of the central retina located ~1 mm temporal-superior to the optic nerve head in a rat eye, imaged over a time span of 3 months are shown in Fig.5.1, thus corresponding to different stages of outer retinal degeneration. H&E-stained histological sections of a similar location in the retina, prepared at baseline, day 7 and 3 months post-injection are presented as well (Fig.5.1B, 1G and 1K, respectively). The cell nuclei appear dark blue in the histology images while the cell bodies appear pink due to their different stain absorption. All intra-retinal layers and the choroid are clearly visible in the healthy retina (Fig.5.1A). The histology section acquired at baseline (Fig.5.1B) also shows a clear view of all retinal layers including the inner segment (black arrow) and outer segment (red arrow) of the PR layer. Six hours after drug administration (Fig.5.1C), the PR outer segment (OS) structure is disrupted and the OS low reflective band appears darker indicating increased reflectivity (Fig.5.1C, bracket) in the OCT images. A low reflective layer is observed to appear between the PR layer and RPE (Fig.5.1C, arrow). One day post injection (Fig.5.1D), the OS appears similar to its normal low reflective contrast , the low reflective layer located between the PR and RPE has disappeared and the external limiting membrane (ELM) and the inner segment (IS) to OS junction (IS/OS junction) are less visible. The ordered inner and outer segment structure disappears at day 3 post sodium iodate injection (Fig.5.1E), while the layered structure of the PR is completely disrupted and appears dark, suggesting increased reflectivity (Fig.5.1E, black arrow). At this time point, the ELM is no longer visible, the outer plexiform layer (OPL) has become irregular in shape (Fig.5.1E, red arrow) and disruptions in the RPE layer are visible (Fig.5.1E, white arrow). The image from day 7 (Fig.5.1F) shows complete decomposition of the PR layer structure (Fig.5.1F, black arrow) and severe irregularity in the OPL (Fig.5.1F, red arrow). The corresponding histology image (Fig.5.1G) also shows irregularities in the OPL and similar decomposition of the PR layer as observed in the OCT tomogram. The detachment at the PR layer is a histology artifact.

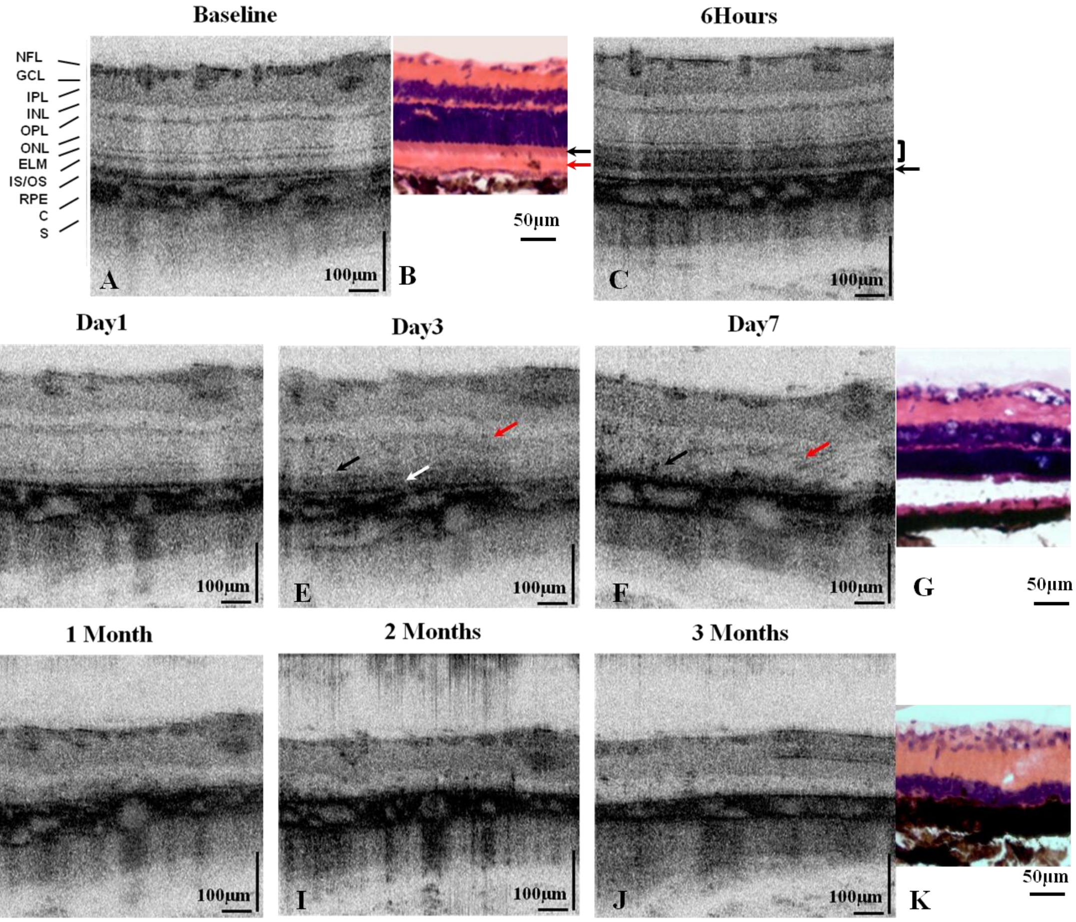

Figure 5.1: Cross-sectional UHR-OCT and histology images of rat retina at different stages of the outer retina degeneration. Healthy retina at baseline (A) show all layers of a normal rat retina. Images acquired at various time points after drug injection show the gradual degeneration and decomposition of the outer retina (C-F and H-J). Histological cross-sections acquired at baseline (B), day 7 (G) and month 3 (K) post drug administration correlate well with the corresponding OCT images of the same time point. NFL: nerve fibre layer, GCL: Ganglion cell layer, IPL: inner plexiform layer, INL: inner nuclear layer, OPL: outer plexiform layer, ONL: outer nuclear layer, ELM: external limiting membrane, IS/OS: inner segment outer segment junction, RPE: retinal pigment epithelium, C: choroid, S: sclera. (Figure reproduced from[154] with permission from the journal)

One month post drug administration, the outer retina appears collapsed, and a thin, irregularly shaped layer of highly reflective material separates the inner nuclear layer (INL) from the choroid (Fig.5.1H). Images acquired 2 and 3 months post injection of sodium iodate (Fig.5.1I and 1J, respectively) show progressive and complete disintegration of the outer retinal structure. The INL appears in direct contact with the choroid due to absence of the outer retina. The histological section acquired at 3 months post drug injection (Fig.5.1K) confirms the absence of the outer retina. Here the lower border of the dark blue INL is in contact with the choroid.

Quantitative analysis of the structural changes over time in the outer retinal degeneration model was carried out by segmenting the individual retinal layers from the UHR-OCT tomograms and measuring their average thickness and optical reflectivity as a function of time. The segmented tomograms were from the 3D imaged volumes corresponding to ~1mmx1mm area at the surface of the retina located ~1mm temporal-superior to the optic nerve head. A representative cross-sectional retinal tomogram and the corresponding segmented image are presented in Figure 5.2. The region between each two lines is considered one layer. In Fig.5.2A all retinal layers as well as the choroid and sclera are labeled. Brackets in Fig.5.2B mark the regions used for quantitative assessment of the thickness and reflectivity changes. The total retina is measured from the surface of the NFL to the bottom of the RPE as labeled by a bracket in Fig.5.2B. The segmentation algorithm was able to segment the choroid and 9 layers in the healthy rat retina, 4 of which were the sub-layers of the PR (1. the pale IS layer from ELM to IS/OS junction, 2. the dark IS/OS junction, 3. the pale OS band below IS/OS and 4. the dark band of the OS-RPE junction). The first PR band (from ELM to IS/OS junction) was not included in the RP layer measurements since it was only visible in the baseline and hour 6. Hence the PR layer was measured from IS/OS junction to the RPE. The number of segmented retinal layers changed over time with the outer retinal degeneration. In the experimental group, no data was available after day 7 for the ONL (D) and after day 3 for the IS/OS junction to RPE (E) because these layers could not be segmented due to sever disruption and degeneration. Therefore, the analysis of these layers was done from the baseline (before treatment) until the last time point at which the layer was still present.

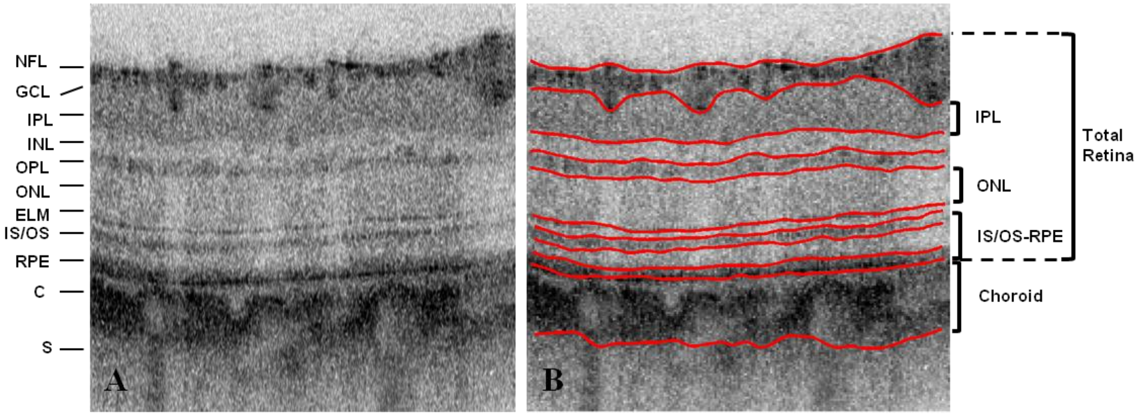

Figure 5.2 Original (A) and segmented (B) UHR-OCT tomogram acquired at baseline (day 0, before sodium iodate injection) highlighting different retinal layers (A) and regions used for extracting thickness and reflectivity values (brackets in B). (Figure reproduced from[154] with permission from the journal)

Figure 5.3 shows sample segmented OCT images acquired at different time points of the study. As explained above, 10 layers were segmented in the baseline images including 4 layers within the PR layer (Fig.5.3A). At six hours post injection 9 layers could be segmented including 3 in the PR layer (Fig.5.3B). One day post injection, only one layer could be detected in the PR layer resulting in a total of 7 layers (Fig.5.3C). At day 3, the OPL could not be segmented due to severe disruption and hence, 6 layers were segmented (Fig.5.3D). Seven days post injection 6 layers could be segmented (Fig.5.3E). However, due to the severe irregularities in the PR layer structure, it could not be segmented as a continuous layer and hence the measurements from this layer were not included in the analysis from this time point onward. At one, two and three months post injection (Fig.5.3F, Fig.5.3G and Fig.5.3H respectively) 4 layers were segmented, three of which were the inner retinal layers (NFL, IPL and INL).

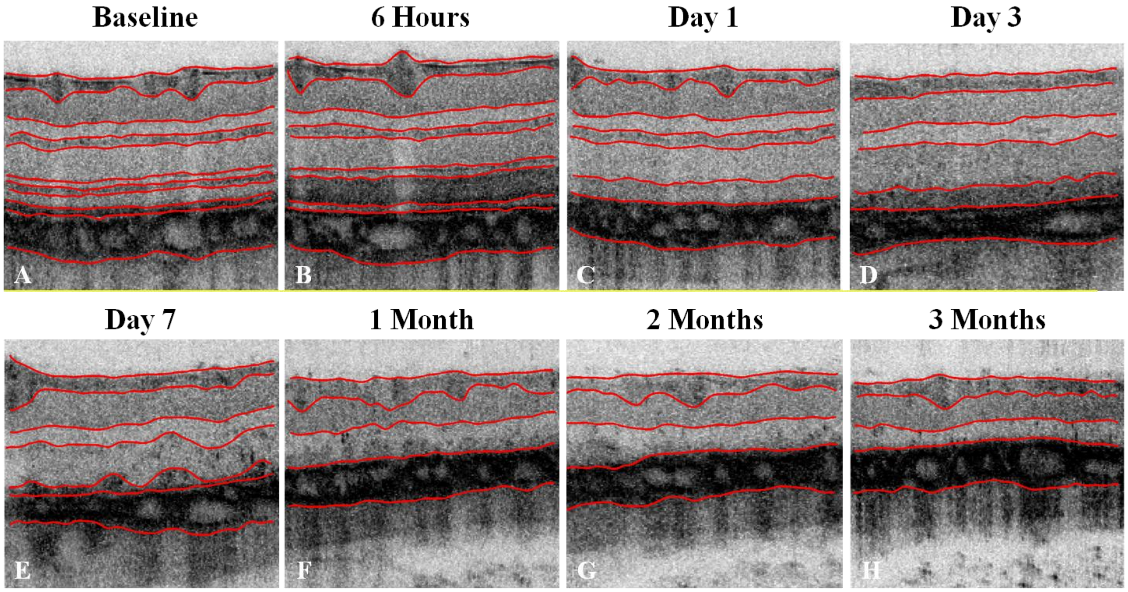

Figure 5.3 shows sample segmented OCT tomograms acquired from a rat at baseline (A), 6 hours (B), day 1 (C), day 3 (D), day 7 (E), 1 month (F), 2 months (G), 3 months (H).

Statistical results from the retinal layer thickness and intensity (reflectivity) measurements for both experimental (sodium iodate injected) and control groups are presented in Fig.5.4 and Fig.5.5 for different time points of the longitudinal study. The black and red bars represent the average values for the drug injected and the control groups respectively. The error bars depict one standard deviation in the graphs.

For the statistical analysis, one way repeated measures ANOVA was used. When $p<0.05$, Bonferroni corrected pairwise comparisons were used for the post-hoc testing. Time points that were significantly different from the baseline are marked with an asterisk in the graphs (Fig.5.4 and Fig.5.5).

Results showed that there was no significant change in any of the time points in the control study in thickness (total retina: F=1.42, p=0.35; choroid: F=0.18, p=0.82, IPL: F=2.23, p=0.26; ONL: F=0.52, p=0.54; IS/OS-RPE: F=0.75, p=0.51) in the control group over the 3 month of the study.

In the sodium iodate injected group the total retinal thickness showed significant changes over time (F=218, p=0.000002). Probability values from the Bonferroni corrected pairwise comparisons are presented in Table 5.1 below. values significant at p≤0.0178 are shown in red (28 pairs for 8 time points, α=0. 05/28=0.00178).

Total retina thickness	Base	6 hours	Day 1	Day 3	Day 7	Month 1	Month 2	α=0.05/28
Base								0.00178
6 hours	0.03712							
Day 1	0.12235	2.30E-05						
Day 3	0.19794	3.61E-05	1					
Day 7	2.97E-05	2.39E-08	0.04919	0.02995				
Month 1	8.97E-12	1.47E-13	6.38E-10	4.71E-10	2.32E-07			
Month 2	7.38E-15	3.48E-16	1.53E-13	1.24E-13	8.14E-12	2.50E-05		
Month 3	4.54E-15	2.28E-16	8.74E-14	7.11E-14	4.19E-12	7.69E-06	1	

Table 5.1 Probability values for Bonferroni corrected pairwise comparisons of total retina thickness changes for drug treated animals at each time point. The label "Base" is for the baseline measurements prior to injection. Values significant at p≤0.0178 are shown in red.

The thickness of the total retina was significantly lower at day1, month 1, month 2 and month 3 compared to the baseline (Fig.5.4A).

The choroid thickness (Fig.5.4B) showed no difference at any time point (F=3.42, p=0.1). IPL thickness (Fig.5.4C) showed change over time (F=7.32, p=0.013). Pairwise comparison (α=0.05/28=0.00178) showed that there was a difference between 6 hours & month 3 (p=0.0008) and between day 7 & month 3 (p= 0.00003). However, none of the time points were different from the baseline (all p>0.0178).

There was a change in the ONL thickness (Fig.5.4D) over time (F=15.03, p=0.017). Ten pairs were considered in the post-hoc analysis (5 time points, α=0.05/10=0.005). There was a difference between the baseline and day 3 (p=0.00184), baseline and day 7 (p=0.00365), 6 hours and day 3 (p=0.0009) and 6 hours and day7 (p=0.00189). The ONL thickness was significantly increased at days 3 and 7 of the study. Due to the lack of visibility of the OPL, the ONL could not be segmented with high confidence at the time points past day 7 of the study.

The thickness of the photoreceptor (PR) layer structure, between the IS/OS junction and the RPE (Fig.5.4E), changed significantly over time (F=53.57, p= 0.0047). For the 6 pairs (4 time points) in the pairwise comparison (α=0.05/6=0083), there was a difference between baseline and 6 hours (p= 0.00157), baseline and day 1 (p=0.00173), 6 hours and day1 (p=0.000006), 6 hours and day3 (p=0.00001). Hence the PR layer thickness decreased significantly at 6 hours and day 1 compared to the baseline. After day 3 post injection, the PR structure appeared so irregular that it could not be segmented as a cohesive layer.

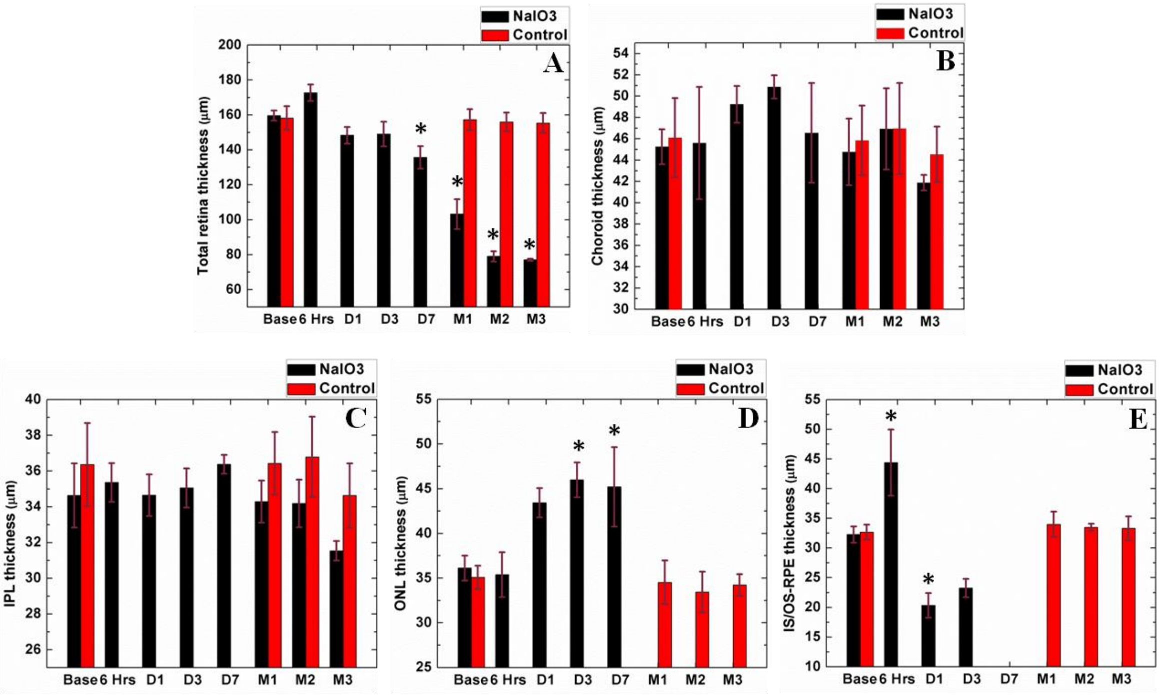

Figure 5.4: Results from statistical analysis of the thickness data over 4 experiment (drug injected) and 3 control rats. In each graph, the $NaIO_3$ injected and control data are shown in black and red columns respectively. Graphs show results for total retina thickness (A), choroid (B), IPL (C), ONL (D) and IS/OS junction to RPE (E). Error bars represent the standard deviation. Asterisks at each column in the graphs indicate the statistically significant deviation of thickness from the baseline. In the experimental group, no data is show after day 7 for the ONL (D) and after day 3 for the IS/OS junction to RPE (E) because these layers could not be segmented due to sever disruption and degeneration. Please see Table 5.1 for additional significant pairwise comparisons. (Figure reproduced with modifications from[154] with permission from the journal)

Figure 5.5 summarizes statistical results for the observed changes in the tissue reflectivity of the rat retina as a whole, as well as for individual retinal layers, as a function of time in both experiment and control groups. Since the image contrast varied somewhat during the different imaging sessions due to slight variation in the system performance, light coupling in the animal eye, and possible differences in the image quality in different animals, the intensity of each layer was normalized to that of the corresponding IPL. This normalization assumed that the IPL reflectivity was not affected significantly by the sodium iodate-induced outer retinal degeneration. The IPL was chosen for the normalization procedure, because it appeared to remain unaffected by the drug-induced retinal degeneration. Of course, this normalization was not performed on the IPL reflectivity values and the statistical analysis was performed on the absolute values acquired from this layer to preserve the possible variations in this layer over time. The reflectivity changes are presented in percentage by setting the experimental group's baseline value (day 0, images before drug administration) equal to 100% in Fig.5.5 for convenient comparison.

Results showed that there was no significant change in any of the time points in intensity (total retina: F=1.23, p=0.38; choroid: F=3.59, p=0.14; IPL: F=2.63, p=0.24; ONL: F=1.46, p=0.34; IS/OS-RPE: F=1.22, p=0.38) in the control group over the 3 month of the study.

The statistical analysis of the data from the drug treated animals showed that the total retina reflectivity (Fig.5.5A) changed as a function of time (F=29.54, p=0.002). Probability values for the Bonferroni corrected pairwise comparisons are presented in the Table 5.2. Since there are 28 pairs (8 time points) the corrected alpha value is α=0. 05/28=0.00178. Probability values significant at p<0.0178 are shown in red in the table.

Total retina reflectivity	Base	6 hours	Day 1	Day 3	Day 7	Month 1	Month 2	α=0.05/28
Base								0.00178
6 hours	0.01131							
Day 1	7.11E-06	0.10747						
Day 3	2.71E-05	0.44924	1					
Day 7	0.0016	1	0.6799	1				
Month 1	1.77E-08	6.00E-05	0.1193	0.02698	3.84E-04			
Month 2	1.47E-08	4.68E-05	0.0917	0.02061	2.96E-04	1		
Month 3	1.26E-08	3.82E-05	0.07378	0.01651	2.39E-04	1	1	

Table 5.2 Probability values for Bonferroni corrected pairwise comparisons of total retina reflectivity changes at each time point. The label "Base" is for the baseline measurements prior to injection. Values significant at $p \leq 0.0178$ are shown in red.

These results showed that the total retina reflectivity was reduced significantly from day 1 onward compared to the baseline. There was no change in the reflectivity of the choroid (Fig.5.5B) over time (F=3.28, p=0.3).As reported in previous studies[114], [117], [124] and confirmed in this study, the IPL reflectivity did not change significantly over time (F=0.52, p = 0.62046; Fig.5.5C).

The reflectivity of the ONL (Fig.5.5D) showed significant change over time (F=10.02, p=0.0099). Pairwise comparisons between time points (5 time points, 10 pair, α=0.05/10=005) showed that there was a different between baseline and day 3 (p=0.00362) and between 6 hours and day3 (p=0.00154). Hence, the data showed that the reflectivity of the ONL was significantly increased at day 3 compared to the baseline consistent with the collapse of the PRL and re-distribution of highly reflective material throughout the outer retina.

The reflectivity of the PR layer structure between the IS/OS junction and RPE (Fig.5.5E) changed as a function of time (F=10.58, p=0.033). Bonferroni corrected pairwise comparisons (4 time points, 6 pairs, α=0.05/6=0083) showed that there was a difference between baseline and day 1 (p=0.00294). The PR layer was significantly reduced at day 1 compared to the baseline.

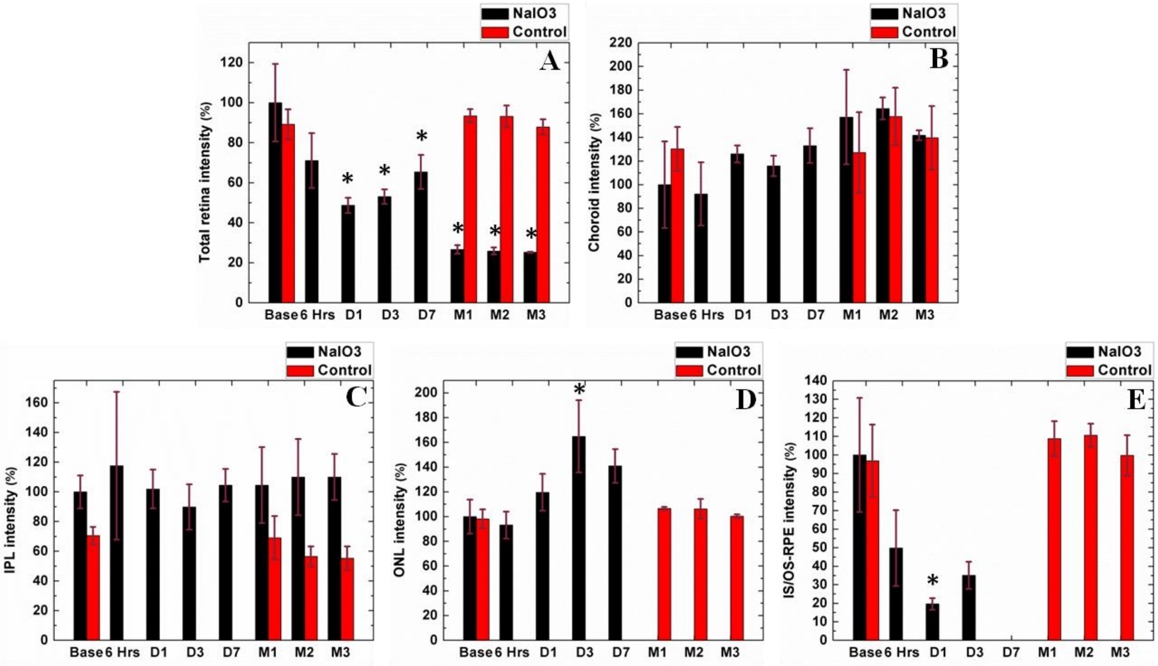

Figure 5.5: Results from statistical analysis of the intensity (reflectivity) measurements over 4 experimental (drug injected) and 3 control rats. In each graph, the $NaIO_3$ injected and control data are shown in black and red columns respectively. Graphs show results for total retina thickness (A), choroid (B), IPL (C), ONL (D) and IS/OS junction to RPE (E)). Error bars represent one standard deviation. Asterisks at each column in the graphs indicate the statistically significant difference between the reflectivity of that layer at that time point from the baseline. In the experimental group, no data is show after day 7 for the ONL (D) and after day 3 for the IS/OS junction to RPE (E) because these layers could not be segmented due to sever disruption and degeneration. Please see Table 5.2 for additional significant pairwise comparisons. (Figure reproduced with modifications from[154] with permission from the journal)

To map out spatial variations in the total retinal thickness and reflectivity over time, B-scans from one 3D data set acquired from approximately the same location of an animal retina at each time point of the longitudinal study (before and after the treatment) were segmented. The 3D data shown here contains the data from one of the four rats for which total thickness and reflectivity were previously analysed statistically for changes over time.Figures 5.6 and 5.7 show *en face* views of the total retina thickness and reflectivity maps (sum of the values from the individual layers along the depth axis), respectively, of the central region in the rat retina at different time points of the longitudinal study. Each *en face* map consists of 256 segmented B-scans and represents a 1 mm x 1 mm retinal surface area located at ~1mm temporal-superior to the optic nerve head, created using a 1000 x 256 x 512 pixel 3D volume. The similar pattern of surface blood vessels observed in the *en face* views at different time points shows that the 3D sets were successfully acquired from approximately the same location in the retina.

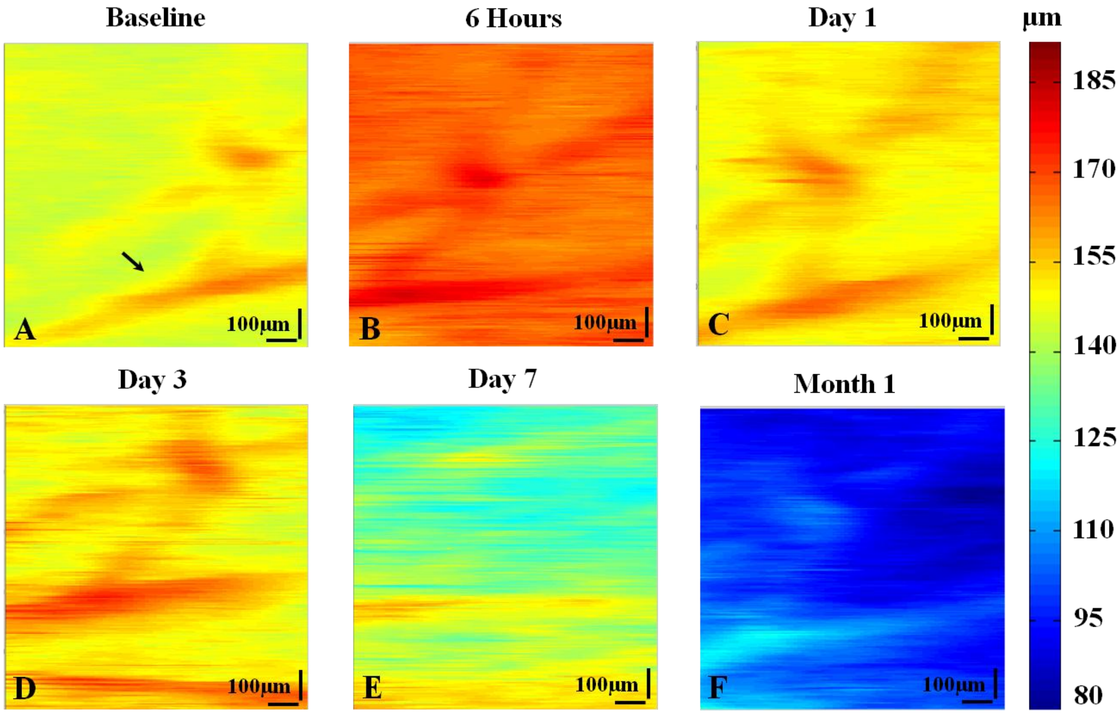

Figure 5.6: Topological thickness maps reconstructed from segmenting 3D OCT image volumes acquired from the central region of the retina of one treated animal at different stages of the degeneration. Each map represents an *en face* view of a tissue surface area of ~1 mm x 1 mm, measured at baseline before treatment (A), 6 hours (B), day1 (C) and day 3 (D) day 7 (E) and 1 month (F) post drug injection. The color bar indicates the color coding values in microns. The arrow in Fig.5.6A points at one of the surface blood vessels. (Figure reproduced from[154] with permission from the journal)

Figure 5.6A shows the thickness distribution of a rat retina at baseline prior to treatment, where slight variation in the thickness is observed due to presence of surface blood vessels (Fig.5.6A, arrow). At days 1 and 3 post injection, consistent with the previous statistical analysis (Table 5.1), no discernible change in the total retina thickness is observed, relative to baseline but the retina is thinner than at 6 hours (Fig.5.6C and Fig.5.6D respectively). The retina thickness shows gradual decrease at day 7 and month1 in Fig.5.6E and Fig.5.6F respectively, consistent with the previous statistical analysis (Table 5.1).

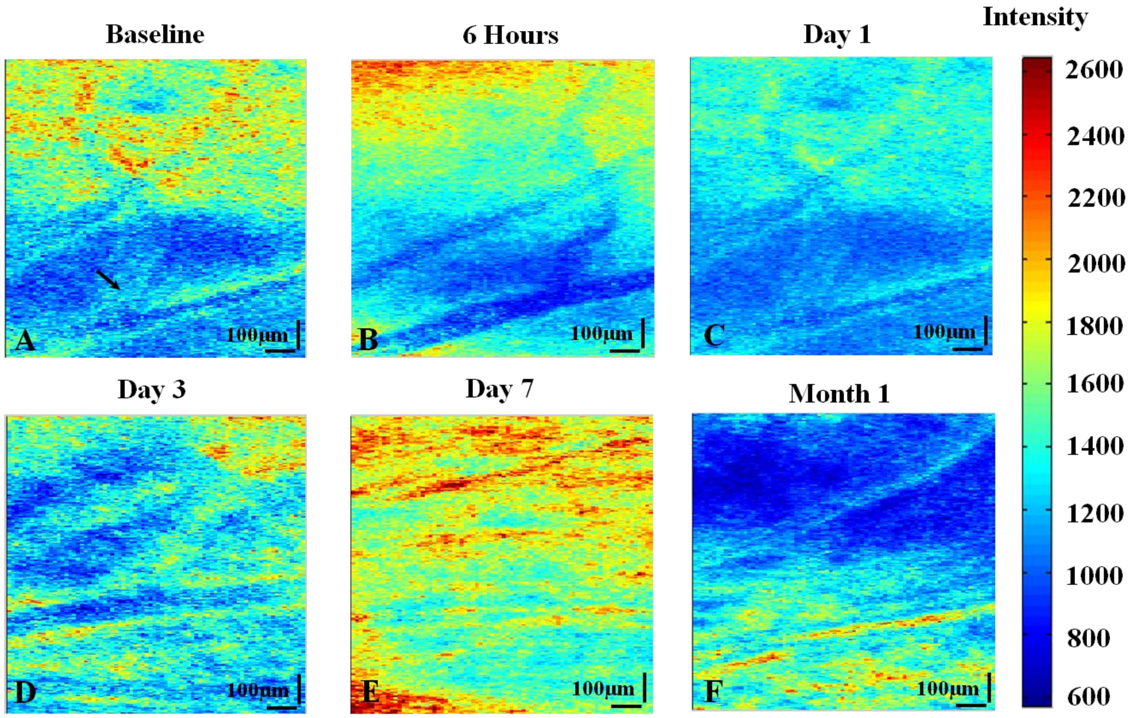

Figure 5.7: Topological reflectivity maps reconstructed from segmenting 3D OCT image volumes acquired from the central region of one treated retina at different stages of the degeneration. Each map represents an *en face* view of a tissue surface area of ~1 mm x 1 mm at baseline (A), 6 hours (B), day1 (C), day 3 (D) , day 7 (E) and 1 month (F) post drug injection. The color bar indicates the camera intensity values in color coding. The camera response is linear with incident irradiance. The arrow in Fig.5.7A points to one of the surface blood vessels. (Figure reproduced from[154] with permission from the journal)

Figure 5.7 presents the total retina reflectivity (intensity) map generated from the same data sets as used for the generation of the thickness data shown in Fig.5.6. Each figure is a 2D *en face* view reconstructed from a 3D set from the sum of the depth-averaged layer values (not normalized to the IPL) in each A-scan from NFL to RPE. Figure 5.7A shows the intensity distribution in the healthy baseline retina as well as some variations related to presence of surface blood vessels (arrow). The total retina reflectivity is reduced by day 1 relative to the baseline, consistent with the previous statistical analysis (Table 5.2), with the plots consistent with a further significant decrease between Day 7 and Month 1(Figs.5.7B-F). Due to the presence of a severely irregular distribution of the high reflective material, the surface blood vessels could not be visualized clearly at day 7 (Fig.5.7E).

5.6 Discussion

The quantitative thickness measurements in Fig.5.4 illustrate the changes in layers at different stages of the outer retina degeneration. The IPL thickness did not vary significantly over the 3 month period of this study, as expected, indicating sparing of the inner retina, similar to that reported in previous studies using histopathology[114], [117], [124]. The ONL thickness increased significantly by about 30% at day 3 and 25% at day 7 (with respect to baseline), potentially as a result of loss of ELM and merging of the ONL with the first bright band of the IS and also potential changes occurring in the ONL structures. The PR structure from the IS/OS junction to the RPE was the location of the earliest observed changes in the retina. At 6 hours post injection the PR layer thickness increased significantly with respect to baseline by 38% due to the appearance of an additional, low reflective band between the PR OS and the RPE which disappeared by day 1 when the PR layer was significantly thinner than baseline. The low reflectivity and short period of time over which this layer appeared and then disappeared together suggest that the layer is most likely comprised of fluid. The thickness of the PR structure decreased significantly by 40% at day 1 suggesting PR decomposition.

The total retina thickness did not change significantly at 6 hours and day 1 post injection compared to the baseline despite the significant changes in the PR layer thickness (~12 µm increase and ~11 µm decrease respectively). Although the ONL thickness has increased significantly (~10 µm increase) at day 3 post injection, the thickness of the total retina has not changed significantly. The lack of significant change in the total retina thickness despite the significant changes in other layers at 6 hours, day 1 and day 3 is most likely because the thickness changes caused by PR layer and ONL fall within the variability of the total retina thickness values and because the PR and ONL may be changing in opposite directions during some of this period. The total retina thickness was decreased significantly at day 7 by about 16% (~25 µm decrease) with respect to the baseline. This change is mainly caused by the thickness changes in the ONL (~9 µm increase) and PR layer (~32 µm decrease as a result of complete loss of PR layer). Total retina thickness at 1, 2 and 3 months post injection showed significant decrease compared to the baseline by about 36%, 50% and 52% respectively. At this time points, the PR layer and ONL could not be distinguished and segmented due to sever outer retina disruption and degeneration.

Quantitative analysis of the reflectivity measurements in Fig.5.5 showed intensity variations at different stages of the degeneration. As expected, the IPL showed no significant variations in the reflectivity over time. The slight variation in the reflectivity of this layer was most likely due to slight change in the system performance, coupling of the beam into the animal eye at different imaging sessions. The ONL reflectivity increased significantly by 65% at day 3 with respect to the baseline most likely due to non-even distribution of highly reflective debris within the outer retina which could also be partially responsible for the significant increase in the ONL thickness observed at this time point. The decrease in the intensity of the PR layer was significant at 80% at day 1 with respect to the baseline when the high reflective bands in the PR layer structure in the OCT tomograms appeared less reflective (reduced contrast). This is most likely due to active decomposition process and disorganization and loss of photoreceptor cell bodies. At later time points the PR layer could not be segmented as a continuous layer due to severe irregularities. The total retina reflectivity changed significantly at days 1, 3 and 7 as well as months 1, 2and 3 post injection compared to the baseline by about 52%, 47%, 35%, 74%, 73%,and 73% respectively.

The thickness and reflectivity surface maps presented in this chapter (figs.5.6 and 5.7) only serve as sample qualitative demonstrations. To explore the intra-animal variations, statistical analysis on the data from single animals at different time points must be conducted in future studies.

The observed thickness increase assumed to be retinal swelling and the formation of a low reflective region below the PR layer at 6 hours post-injection have not been reported in other studies. The only other method previously used to examine the retinal cross-sectional morphology in detail is histology. The histology results presented in this study (Fig.5.1) are consistent with the histology results reported in previous studies[107], [116], [124] (i.e. disruption of the photoreceptor inner and outer segments at day 7 and complete loss of outer retina at 3 months post drug administration). The procedure involved in processing tissue for histology can lead to artefacts, including the separation of the retina from the choroid, which could be a reason why this particular layer has never been observed in histopathological studies. However, using electron and light microscopy and kinetic vitreous fluorophotometry, some studies reported swelling of RPE cytoplasmic organelles at 6 hours, a decreased number of RPE cell nuclei at 12 hours[106] and breakdown of the choroidal blood retina barrier at the RPE 24 hours post drug administration[120], all of which could be related to an influx and efflux of fluid. These movements of fluid could explain the appearance and subsequent disappearance of the low reflective region between the PR and RPE in this study. Further investigation of the sodium iodate effect in earlier time points and using OCT along with other techniques such as FA and FAF may be required in order to determine the origins and composition of the newly observed phenomenon.

5.7 Conclusion

In this study, a state-of-the-art, high speed, UHR-OCT system along with a semi-automatic segmentation algorithm were used to visualize, quantify and monitor the structural and reflectivity changes of the rat retina over time in a sodium iodate model of outer retina degeneration. Furthermore, swelling of the retina due to what is most likely a temporary fluid accumulation associated with the drug induced retina degeneration in this model was depicted for the first time. Results presented here showed that outer retinal damage can be characterized by changes in the layer thickness, shape, integrity and optical properties of different retinal layers.

Chapter 6

Acute Effect of Sodium Iodate Toxicity in a Rat Model of Outer Retina Degeneration Imaged *In Vivo* with Ultrahigh Resolution Optical Coherence Tomography

This chapter is based on the following manuscript:

S. Hariri, Man Chun Tam, Donghyun Lee, Denise Hileeto, A. A. Moayed, and K. Bizheva, "Non-invasive imaging of the early effect of sodium iodate toxicity in a rat model of outer retina degeneration with SD-OCT", Journal of Biomedical Optics, Feb. 2013. Issue 2, Vol. 18.[162]

The UHR-OCT system used for this study was designed and built by Dr. Kostadinka Bizheva. She has also overseen the experiments, the data analysis and the manuscript preparation and made revision to the text.

A.A.Moayed assisted with animal handling and imaging, data processing, revisions and proofreading of the manuscript.

After the completion of this thesis, Man Chun Tam and Donghyun Lee performed additional animal experiments for comparison of the OCT images with histology and Denise Hileeto prepared and analysed the histological and immunohistochemical cross-sections obtained from $NaIO_3$ treated rat retinas. These preliminary histology data were not included in this thesis.

Planning and conducting the animal experiments, the OCT image processing, image segmentation, statistical analysis of the thickness and reflectivity data, as well as the manuscript preparation are the author's work.

The author would like to thank Dr. Hutchings and Dr. Campbell for their useful advice and assistance with improving the statistical analysis methods used in this chapter.

The author would like to sincerely acknowledge Dr. N. Hutchings from the School of Optometry, University of Waterloo and Dr. S. Boyd from St. Michael's hospital, Toronto, for helpful suggestions related to the $NaIO_3$ model, H. van der Heide from the University of Waterloo Science Shop for assistance with machining the imaging probe, and N. Gibson from University of Waterloo for assistance with the animal handling and tail vein injections. Financial support for this project was provided by the Natural Sciences and Engineering Research Council (NSERC) of Canada.

6.1 Overview

The short-term, acute effects of sodium iodate toxicity on the rat retina structure was imaged *in vivo* for the first time by use of UHR-OCT.

Outer retinal degeneration was induced in twelve female Long Evans rats via tail vein injection of sodium iodate ($NaIO_3$, 40mg/kg). Six additional rats were used for the control study. Structural changes in the retinal layers of each rat were assessed longitudinally and *in vivo* at baseline and 1, 2, 3, 6, 8, 10 and 12 hours post sodium iodate injection with a high speed UHR-OCT system and segmentation algorithm.

Disruption of the structural integrity of the photoreceptor inner (IS) and outer segment (OS) layers was observed as early as 1 hour post injection of sodium iodate. A new layer of very low optical reflectivity was observed to form between the retinal pigment epithelium (RPE) and the photoreceptor OS a few hours post sodium iodate injection in all treated animals. The thickness of this layer increased, peaked and decreased progressively with time, and the layer disappeared completely by hour 12 of the study. The low reflective layer is most likely a temporary accumulation of fluid in the retina as an acute response to the sodium iodate toxicity. Changes in the reflectivity of individual retinal layers were observed over time and correlated well with the morphological changes seen in the OCT tomograms.

6.2 Introduction

As reviewed in chapter 2.3.1, a number of studies have been carried out in rodent models to investigate the acute, short-term effect of sodium iodate on the retina morphology within the first few hours after the drug administration. These studies utilized research methods such as histology, immunohistochemistry, electron microscopy[106], [114], [116] and vitreous fluorophotometry[120]. The studies reported defragmentation of RPE cell nuclei at ~2 hours post drug administration, disorganization of the rod outer segment discs[115] at ~6 hours, swelling of the RPE cytoplasmic organelles at ~6 hours[116], decreased number of RPE cell nuclei at ~12 hours[106], breakdown of the blood-retina barrier at ~24 hours post drug administration[120] and significant reduction in the adhesion between the RPE and the Bruch's membrane 10 minutes and between RPE and neuro-sensory retina ~2h and onward after sodium iodate administration [102].

In the previous chapter, the long-term effect of sodium iodate on the morphology of rat retina was investigated. Moreover, the presence of a very low reflective layer between the RPE and the photoreceptor outer segment (OS) layers at ~6 hours post sodium iodate injection was reported for the first time, which disappeared by day 1 of the study. The presence of this additional layer has not been reported before. In this chapter, the same high speed UHR-OCT system and segmentation algorithm were used to monitor and quantify for the first time *in vivo* and in detail, the acute short term effects of sodium iodate on the rat retina structure.

6.3 Study Procedure

Eighteen 12-15 weeks old rats were used for this study. Animals were divided into two groups of nine. In both groups six animals were injected with sodium iodate while the other three were used as controls. In group 1 (n=9) 6 rats received the IV sodium iodate injection and 3 control rats received equivalent IV injections of phosphate buffered saline (PBS) as a vehicle. Animals in group 2 received either sodium iodate (n=6) or vehicle (n=3) as well as 1mL supplementary subcutaneous PBS injections at hours 1 and 3 post drug administration intended to decrease the severe adverse side effects of the drug on the animal's internal organs. Animals were imaged at baseline and hours 1, 2, 3, 6, 8, 10 and 12 post $NaIO_3$/vehicle injection. The imaging sessions adhered to a strict schedule, starting at 9-10 am and finishing at 9-10pm and 3D UHR-OCT images were acquired from the same position of the retina for consistency of the experiment.

6.4 Statistical Analysis

The average values of thickness and reflectivity acquired from the segmented 3D data sets (chapter 3.5) were used for statistical analysis. For the statistical analysis of the data acquired from the IPL, ONL, PR layer and choroid, repeated measures ANOVA was performed ($p<0.05$) with 2 within-subject factors (Layer and Time point) and one between-subject factor (Control or Experimental Group).

For the analysis of the total retina thickness and reflectivity, repeated measures with 1 within-subject factor (time point) and one between-subject factor (Control or Experimental Group) was performed. Dunnett 2-tailed was used as the pos-hoc test for comparison between the control and experiment groups.

6.5 Results

Figure 6.1A shows a representative cross-sectional UHR-OCT image of the healthy rat retina acquired at baseline, where all retinal layers are clearly visualized. Since this project focused on examining the acute effect of sodium iodate toxicity on the RPE and photoreceptor IS and OS, it was important to have a good understanding of the healthy rat retina morphology of these layers as visualized on the UHR-OCT images. Figure 6.1B shows a magnified view of a section of the rat outer retina (area marked with the red rectangle in Fig.6.1A) while Fig.6.1C is a schematic of a photoreceptor and an RPE cell. This schematic is based on a recent publication from Spaide and Curcio[152] describing the anatomy of the human photoreceptor cells. The structure of the human rod photoreceptor is very similar to that of rats and therefore could be used as a guideline to draw the rat PR cell schematics. However, the proportions of the rod PR cell in the schematic (Fig.6.1C) presented here are not to scale. Figure 6.1 allows low and high reflective bands in the UHR-OCT image to be related to anatomical features of the photoreceptor and RPE cells.

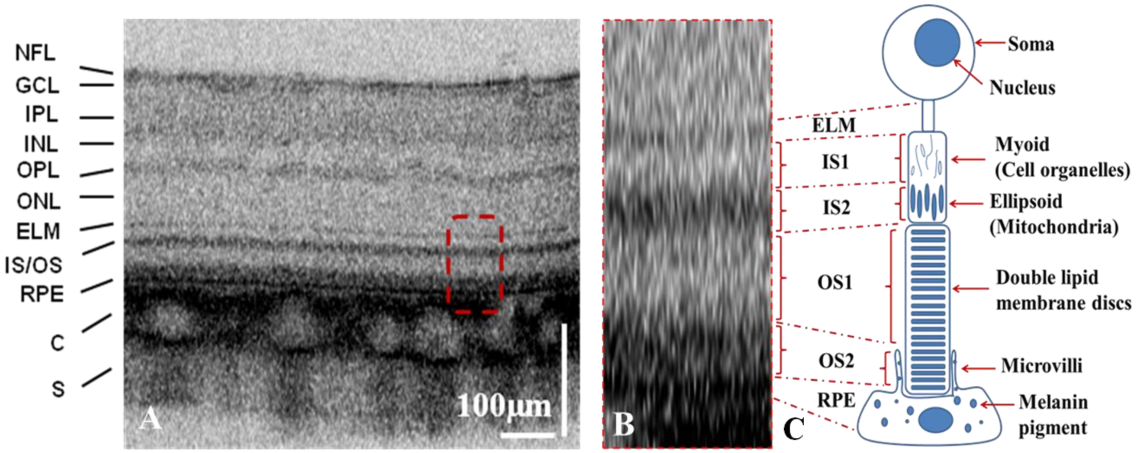

Figure 6.1: A representative UHR-OCT tomogram acquired from healthy rat retina with all retinal layers clearly visible and labeled (A). Magnified view of the photoreceptor and RPE layers (B) allows for direct correlation of the alternating low and highly reflective PR bands to anatomical features of the rod photoreceptor cell in the schematic representation (C). (Figure reproduced from[162] with permission from the journal)

As observed in the UHR-OCT tomogram (Fig.6.1B), the photoreceptor layer consists of alternating low and high reflective layers, which starting from the top and following the analysis presented by Spaide and Curcio [152] , can be interpreted as: a very narrow and highly reflective external limiting membrane (ELM), composed of synapses from the Mueller cells; a low reflective band corresponding to the myoid, the upper section of the photoreceptors inner segment (IS1) that is filled mostly with transparent cytoplasm and cellular organelles such as microfilaments, Golgi apparatus and ribosomes that are less than 1µm in size, thus resulting in weak optical reflectivity; a very highly reflective band corresponding to the ellipsoid, the lower part of the photoreceptor inner segment (IS2) which is filled with densely packed mitochondria with significantly higher refractive index (~1.45)[164] as compared to the surrounding cytoplasm (~1.35)[165], [166]; a low reflective outer segment (OS1) consisting of double lipid membrane dicks of fairly low refractive index; a highly reflective band (OS2), corresponding to the OS/RPE junction, which is filled with interspaced photoreceptor outer segments and highly reflective microvilli of the RPE cells, which contain large quantities of melanin of high optical refractive index (~1.7)[167]; the very thin and highly reflective line corresponds to the RPE, which contains large quantities of melanin. The detailed analysis of the rat outer retina morphology as visualized in UHR-OCT images presented in Fig.6.1, was used as a reference point to examine any structural changes in the photoreceptor and RPE layers caused by the sodium iodate toxicity at different time points of the longitudinal study

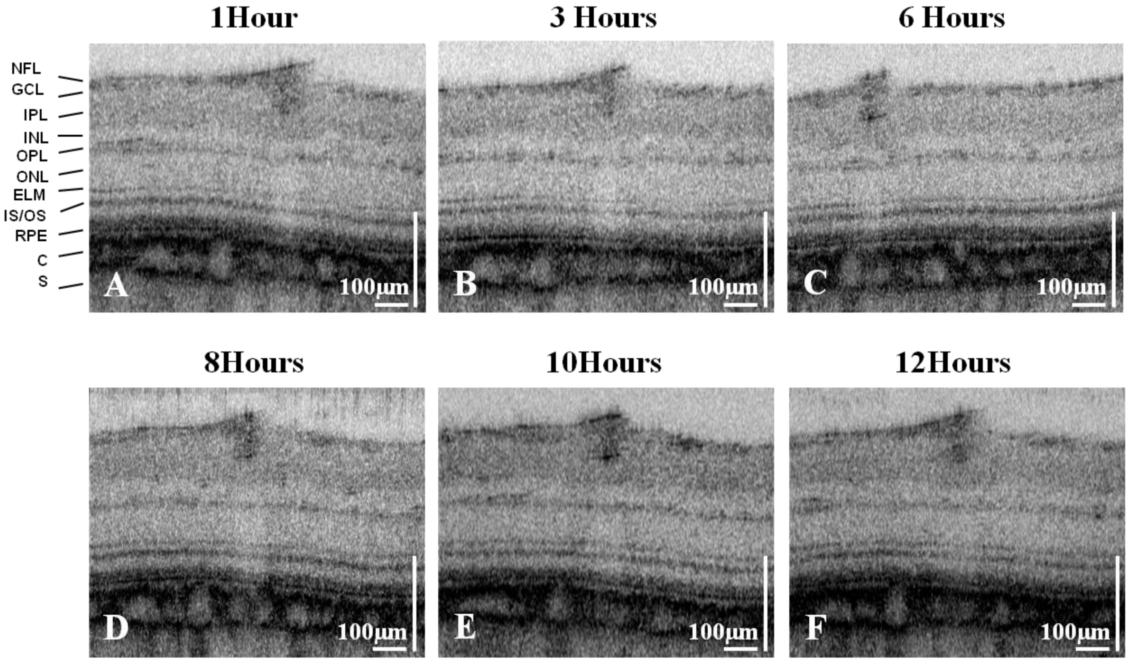

Figure 6.2 Representative 2D OCT tomograms acquired from the same central retinal region from a control animal receiving IV PBS injection as well as additional 1mL subcutaneous PBS injections at hours 1 and 3. Images were acquired at 1 hour (A), 3 hours (B), 6 hours (C), 8 hours (D), 10 hours (E) and 12 hours (F) post IV injection. As expected, no structural abnormalities are observed at any of the time points. All individual retinal layers and the choroidal structure are clearly visible and intact.

Figure 6.2 shows representative OCT tomograms selected from a 3D OCT data set acquired from a 1mmx1mm area from the same central retinal region of a control rat receiving IV vehicle (PBS) injection as well as extra 1mL subcutaneous PBS at hours 1 and 3 post IV injection. Images acquired at 1 hour (Fig.6.2A), 3 hours (Fig.6.2B), 6 hours (Fig.6.2C), 8 hours (Fig.6.2D), 10 hours (Fig.6.2E) and 12 hours (Fig.6.2F) show no structural abnormalities in the retina. As expected, all individual retinal layers and the choroidal structure are clearly visible and intact as seen typically in normal healthy animals.

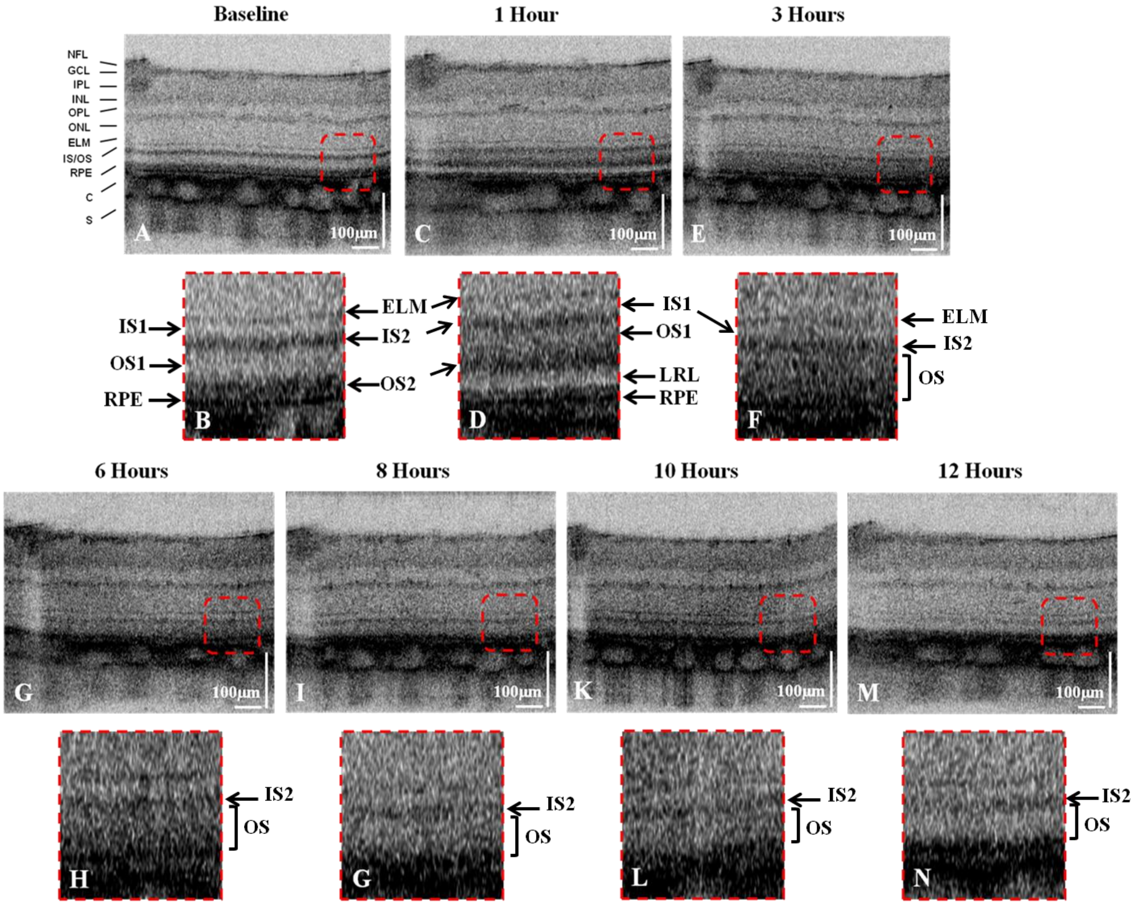

Figure 6.3: UHR-OCT cross-sectional images acquired from the same region of the central retina of a treated animal, showing progressive changes in the outer retina due to the toxic effect of the injected drug: baseline (A and B), 1 hour (C and D), 3 hours (E and F), 6 hours (G and H), 8 hours (I and J), 10 hours (K and L), 12 hours (M and N). This rat showed the smallest reaction to the drug toxicity among all rats that were not hydrated with PBS. (Figure reproduced from[162] with permission from the journal)

Figure 6.3 shows UHR-OCT images from the rat retina acquired at all time points of the longitudinal study from one of the rats that did not receive supplementary PBS injections after the administration of the sodium iodate. The changes observed in this rat occurred in the other 5 rats receiving the same treatment. However, the timing of the changes varied in different animals. The typical layered structure of the normal healthy rat retina imaged at baseline is shown in Fig.6.3A. A magnified view (3x) of a section of the outer retina, marked with the red box in Fig.6.3A is shown in Fig.6.3B, where the bright and dark bands of the PR layer are labeled following the method described in Fig.6.1. Figure 6.3C shows a cross-sectional image of the same location in the retina, acquired 1 hour post sodium iodate injection. The previously clear band corresponding to the OS1 in Fig.6.3B, is now more optically scattering, and a new layer of very low reflectivity (LRL) appears to separate the photoreceptor OS from the RPE. In the enlarged view (Fig.6.3D), the RPE layer appears structurally intact, while the dark, band above it, most likely corresponds to the RPE microvilli. Three hours after the sodium iodate injection, the new LRL is no longer visible (Fig.6.3E). This is confirmed by the magnified view of the outer retina in Fig.6.3F, where the LRL is missing, while the photoreceptor OS layer appears almost homogeneous and highly reflective and can no longer be separated in to two distinct bands of low (OS1) and high (OS2) reflectivity, as in the case of the healthy retina at baseline. The higher scattering could be induced by re-arrangement of the OS, disruption of the membrane disks or both. Six hours post sodium iodate injection (Figs 6.3G and 3H) the appearance of the OS is similar to the previous time point. Images acquired at 8 and 10 hours post injection (Figs 6.3I, 3G, 3K and 3L) show reduced apparent reflectivity in the OS region compared to 3 and 6 hours post injection. Twelve hours after sodium iodate injection (Figs 6.3M and 3N), the appearance of the alternating low and highly reflective bands in the IS and OS layers resembles closer their appearance in the healthy retina at baseline (Figs 6.3A and 3B). However, at this time point the clear border between OS1 and OS2 as well as the border between OS2 and RPE (as seen in the baseline image) are lost, the OS2 appears thinner than its normal appearance in the baseline image and the overall apparent image contrast of the photoreceptor layer has decreased as compared to the baseline image.

The timing of the appearance and disappearance of the LRL, as well as the maximum thickness of the layer varied from animal to animal even within the group of 6 rats that were not hydrated with additional injections of PBS. The results presented in Fig 6.3 show an extreme case of the smallest LRL thickness, as well as the earliest and most rapid appearance and disappearance of that layer, that were observed in a rat that has not been hydrated with PBS. The results presented in Fig.6.4 below show another extreme case from the same group of rats that have not been hydrated with PBS. In this case the LRL appeared as early as 1 hour post sodium iodate injection (Fig.6.4B), gradually increased in thickness over the next few hours, reaching a maximum ~6 - 8 hours post drug injection (Fig.6.4E and 6.4F) and completely disappeared by hour 12 (Fig.6.4H). The photoreceptor OS layer showed similar changes as observed in the other rat (Fig.6.3): increase of the OS layer overall reflectivity and merging of the low and high reflective bands of the OS for the time period from 1 hour to ~10 hours post sodium iodate injection (Figs 6.4B - 4G), during which the LRL appeared, changed thickness and disappeared.

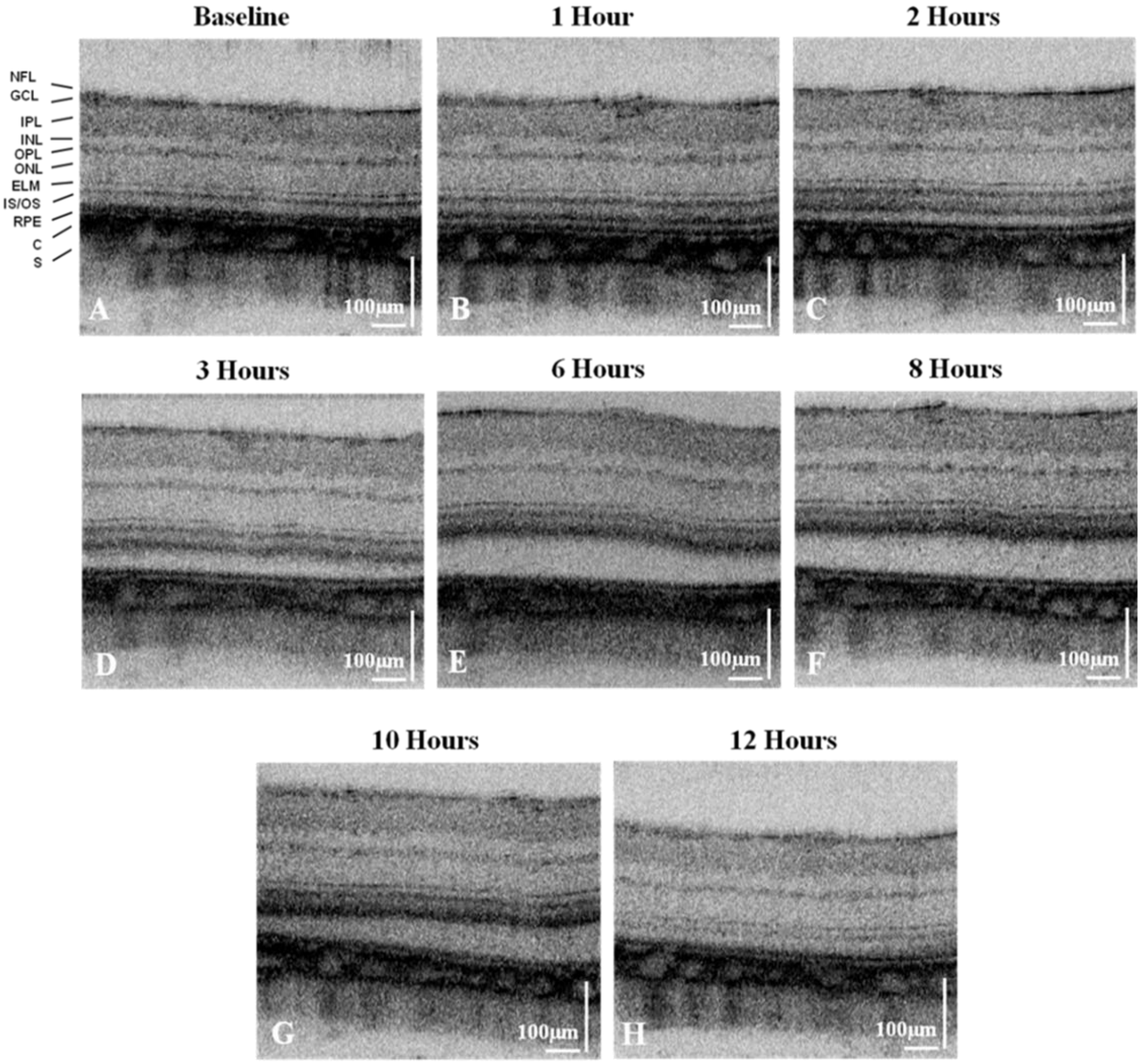

Figure 6.4: UHR-OCT cross-sectional images acquired at the same central location of a rat retina depicting the largest reaction to the drug toxicity in the case of no hydration with PBS: baseline (A) and 1 hour (B), 2 hours (C), 3 hours (D), 6 hours (E), 8 hours (F), 10 hours (G), 12 hours (H) post $NaIO_3$ injection. (Figure reproduced from[162] with permission from the journal)

Less variability in the timing of the appearance and disappearance, as well as the maximum thickness of the LRL in animals that had received additional subcutaneous PBS injections was observed, as compared to results obtained from the rats that were not hydrated with PBS. In all these animals the last time point with a visible LRL was either 3 or 6 hours post drug injection (except for one rat) while in the group with no extra PBS injection the last time point with a visible LRL was anywhere between 1 and 10 hour. Furthermore, the animals receiving no extra PBS injections showed more severe side effects as a result of drug toxicity such as blood in their urine.

Figure 6.5 shows representative UHR-OCT images acquired from a rat that was hydrated with 1mL subcutaneous PBS injections at 1 and 3 hours post sodium iodate administration.

Figure 6.5A shows the healthy rat retina with normal appearance of all retinal layers. One hour post drug injection, the new LRL appears below the PRL (Fig.6.5B). At 2 hours the layer has increased its thickness and the low reflective OS band (OS1) shows initial increase in the optical reflectivity (Fig.6.5C). At 3 hours (Fig.6.5D), the OS1 and OS2 bands that were very clearly visible in the baseline image (Fig.6.5A), can no longer be identified as separate layers, the OS layer appears of almost homogeneous reflectivity and the LRL has grown to its maximum thickness. Six hours post injection of sodium iodate (Fig.6.5E), the LRL has disappeared, though the OS layer still appears as one almost homogeneous and highly reflective band. At hours 8 (Fig.6.5F) and 10 (Fig.6.5G) of the study the OS1 becomes less reflective. The appearance of the OS1 returns to normal at 12 hours post drug administration (Fig.6.5H), while the overall contrast of the IS and OS layers has decreased as compared to the baseline image (Fig.6.5A). Similar results were obtained from the other 5 rats of the group of animals that were hydrated with PBS injections during the 12 hour study. Figures 6.6 to 6.10 present OCT tomograms acquired from these 5 animals at different time points of the study.

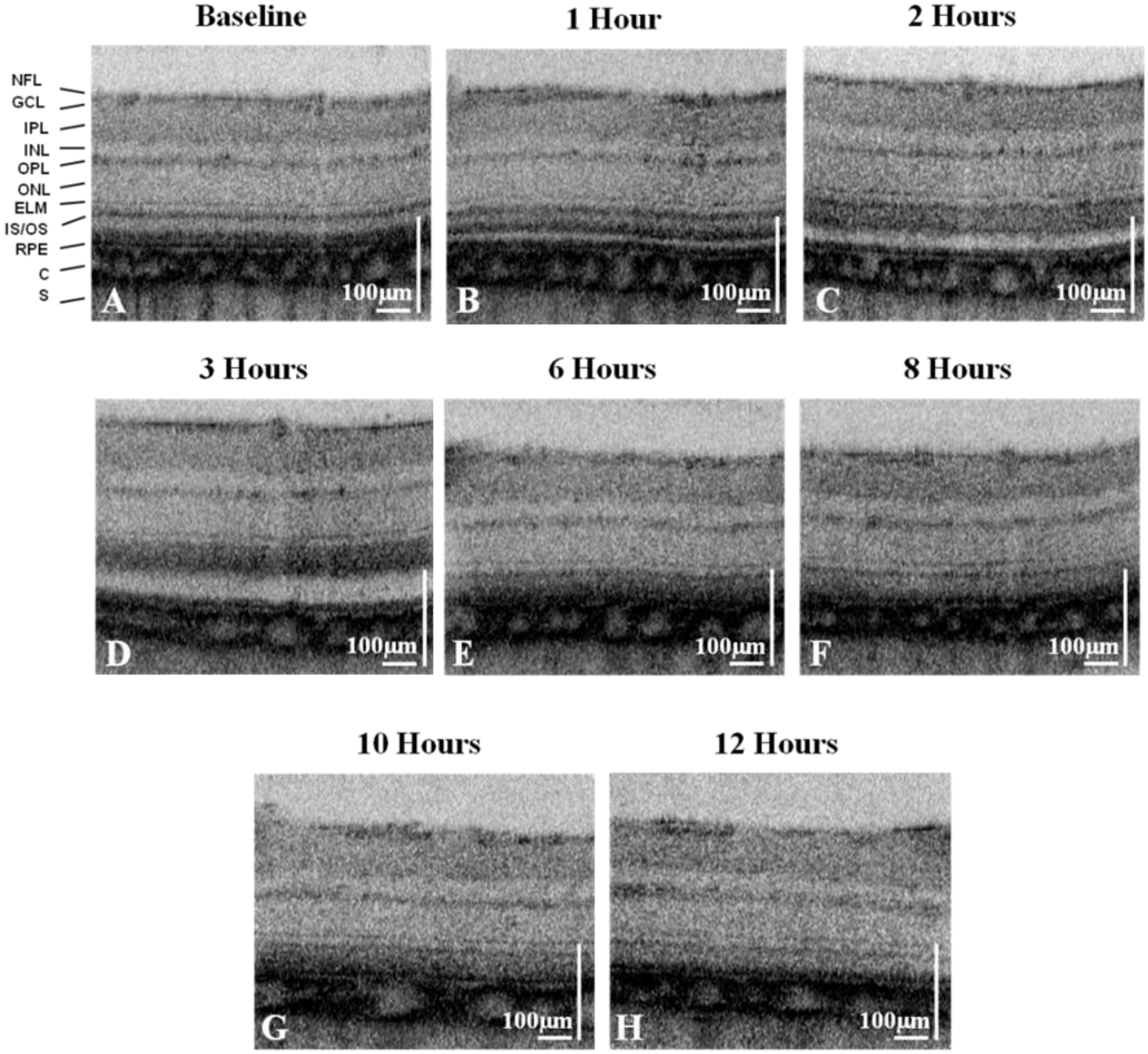

Figure 6.5: OCT tomograms acquired from the same location of central retina over the course of 12 hours from a rat that received sodium iodate as well as a total of 2ml PBS (2 subcutaneous injections at hours 1 and 3 of the study), showing gradual changes to the retina structure as an acute response to the $NaIO_3$ toxicity at: baseline (A) and 1 hour (B), 2 hours (C), 3 hours (D), 6 hours (E), 8 hours (F), 10 hours (G), 12 hours (H) post $NaIO_3$ injection.

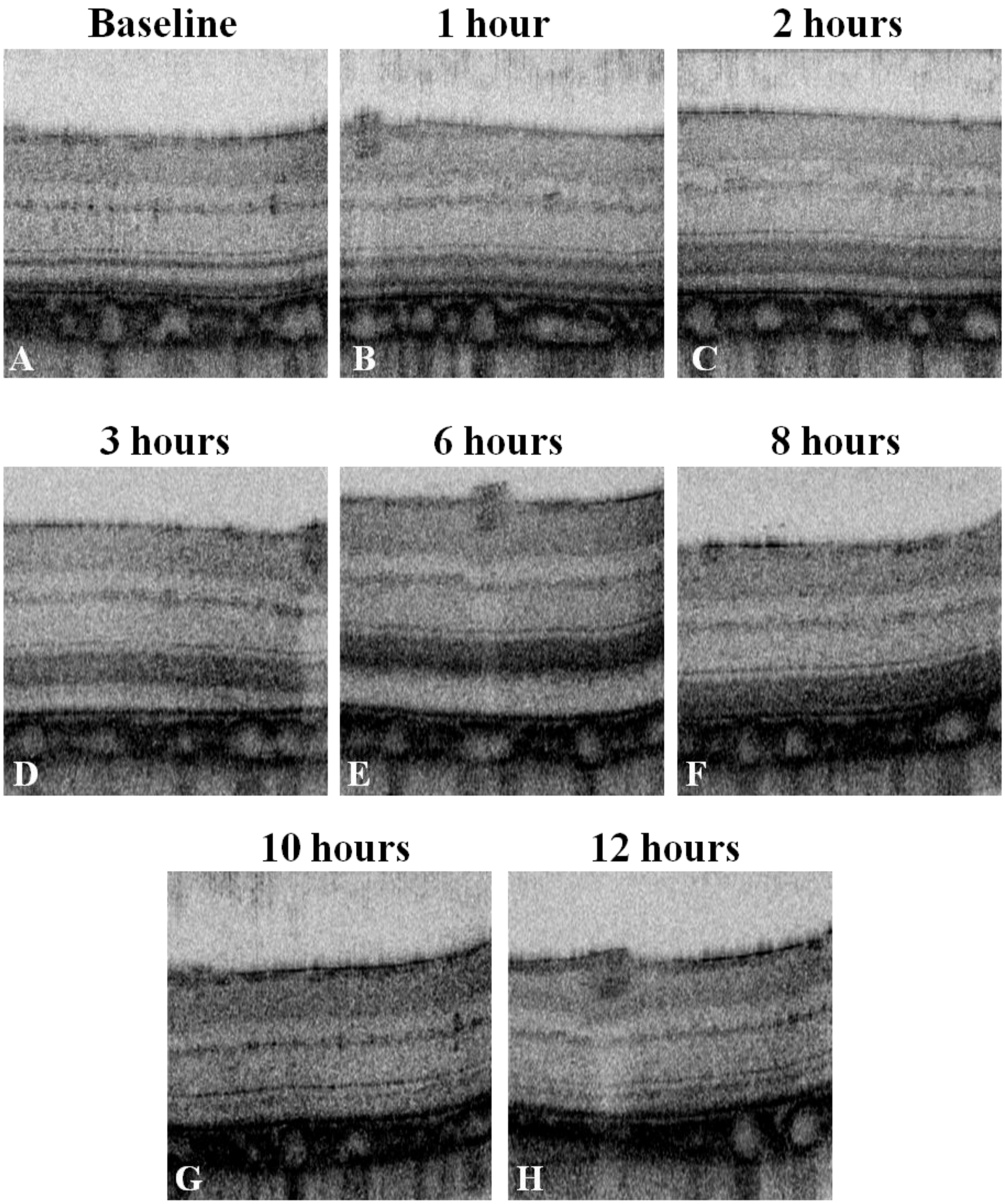

Figure 6.6: OCT tomograms acquired from the central retina over the course of 12 hours from the second rat that received sodium iodate as well as a total of 2ml PBS (2 subcutaneous injections at hours 1 and 3 of the study), showing gradual changes to the retina structure as an acute response to the $NaIO_3$ toxicity at: baseline (A) and 1 hour (B), 2 hours (C), 3 hours (D), 6 hours (E), 8 hours (F), 10 hours (G), 12 hours (H) post $NaIO_3$ injection.

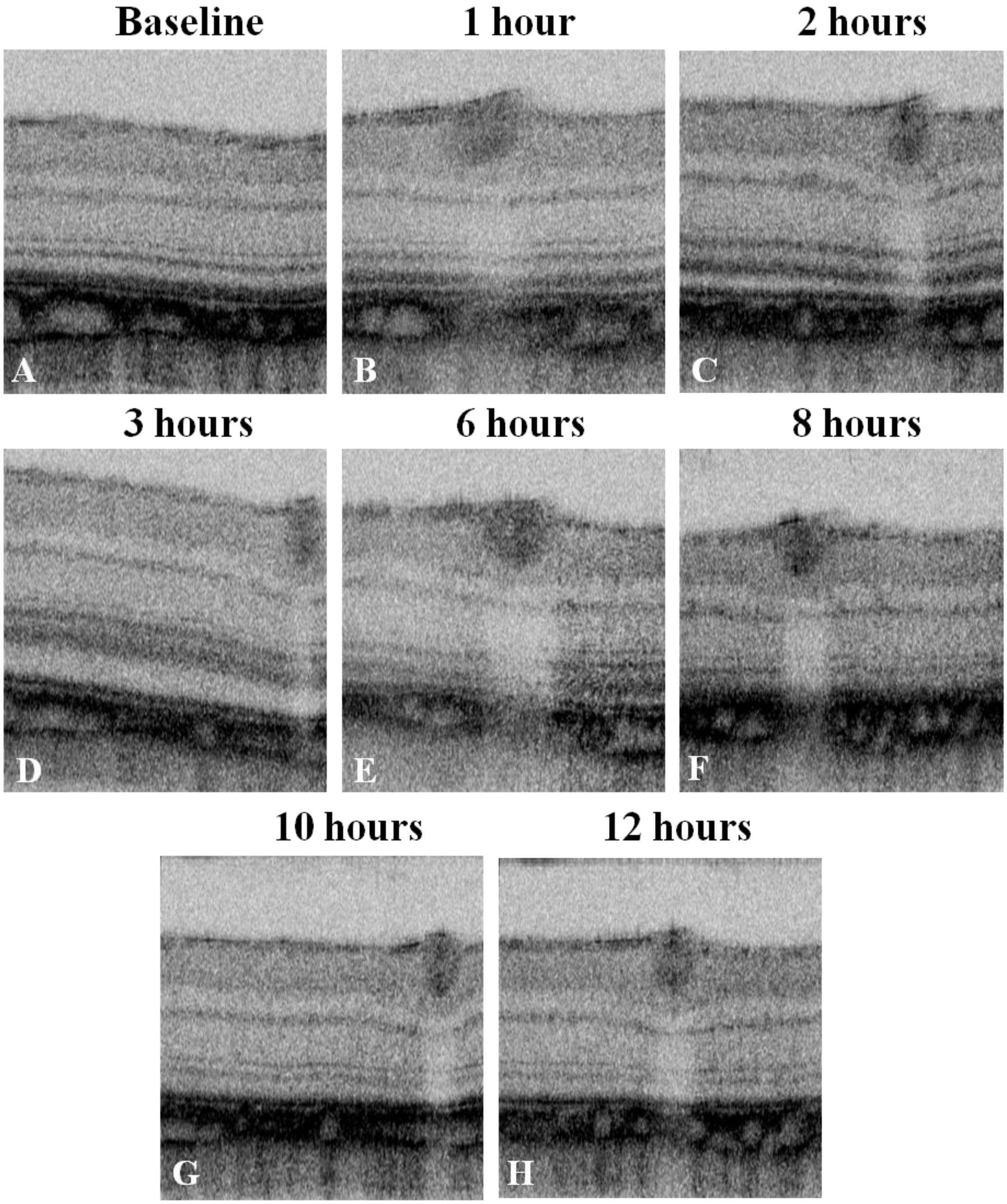

Figure 6.7: OCT tomograms acquired from the central retina over the course of 12 hours from the third rat that received sodium iodate as well as a total of 2ml PBS (2 subcutaneous injections at hours 1 and 3 of the study), showing gradual changes to the retina structure as an acute response to the $NaIO_3$ toxicity at: baseline (A) and 1 hour (B), 2 hours (C), 3 hours (D), 6 hours (E), 8 hours (F), 10 hours (G), 12 hours (H) post $NaIO_3$ injection.

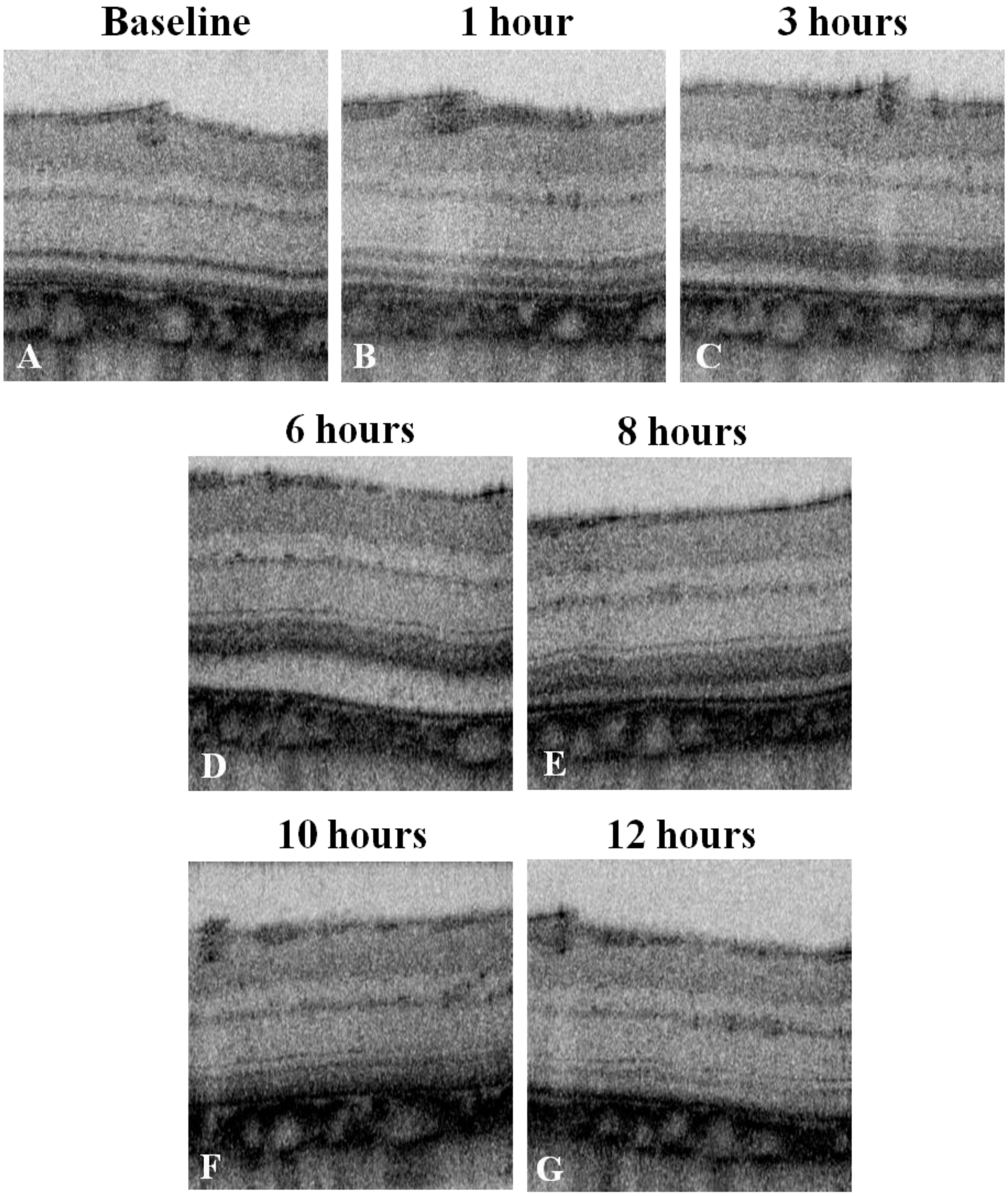

Figure 6.8: OCT tomograms acquired from the central retina over the course of 12 hours from the fourth rat that received sodium iodate as well as a total of 2ml PBS (2 subcutaneous injections at hours 1 and 3 of the study), showing gradual changes to the retina structure as an acute response to the $NaIO_3$ toxicity at: baseline (A) and 1 hour (B), 3 hours (C), 6 hours (D), 8 hours (E), 10 hours (F), 12 hours (G) post $NaIO_3$ injection.

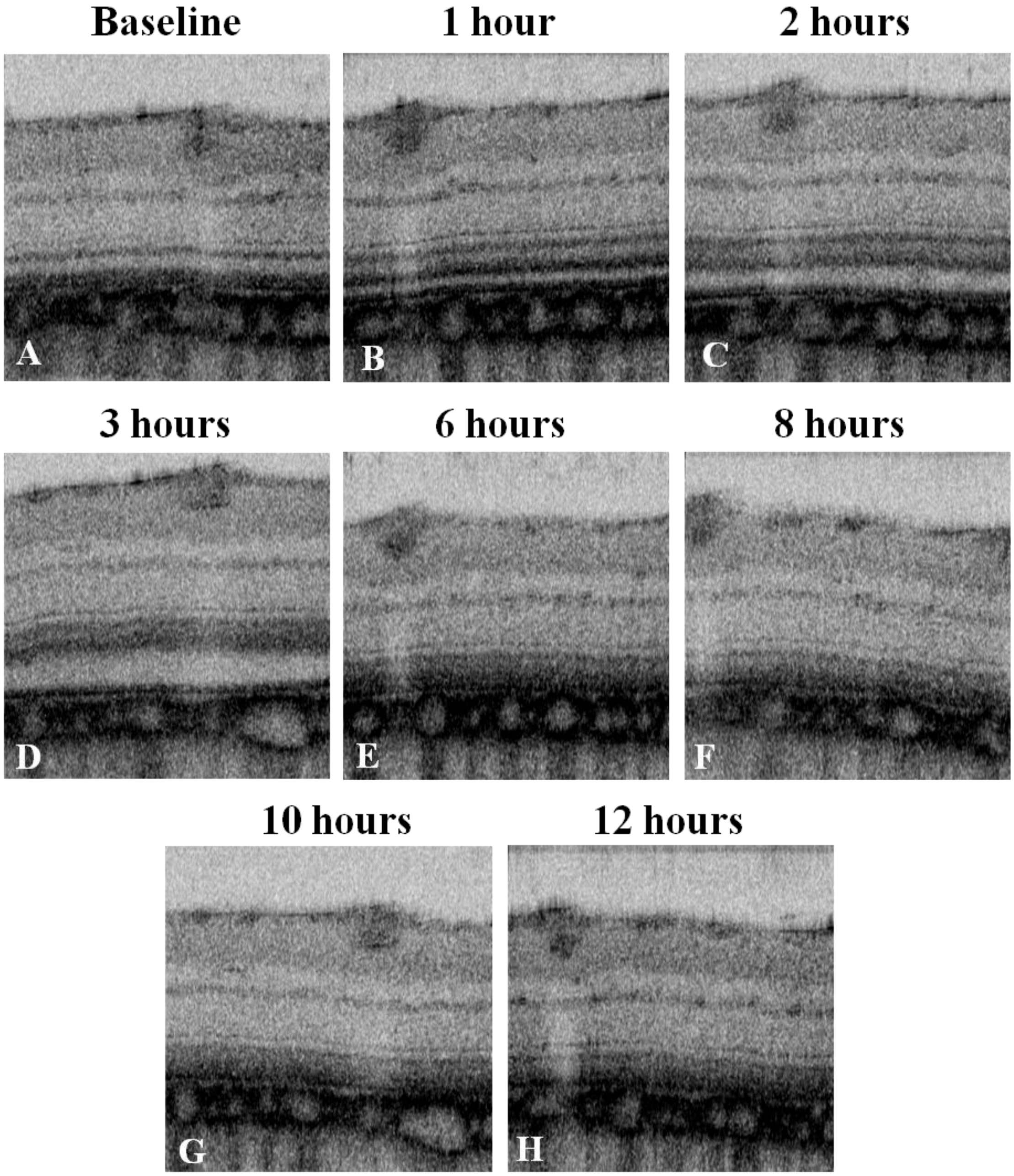

Figure 6.9: OCT tomograms acquired from the central retina over the course of 12 hours from the fifth rat that received sodium iodate as well as a total of 2ml PBS (2 subcutaneous injections at hours 1 and 3 of the study), showing gradual changes to the retina structure as an acute response to the $NaIO_3$ toxicity at: baseline (A) and 1 hour (B), 2 hours (C), 3 hours (D), 6 hours (E), 8 hours (F), 10 hours (G), 12 hours (H) post $NaIO_3$ injection.

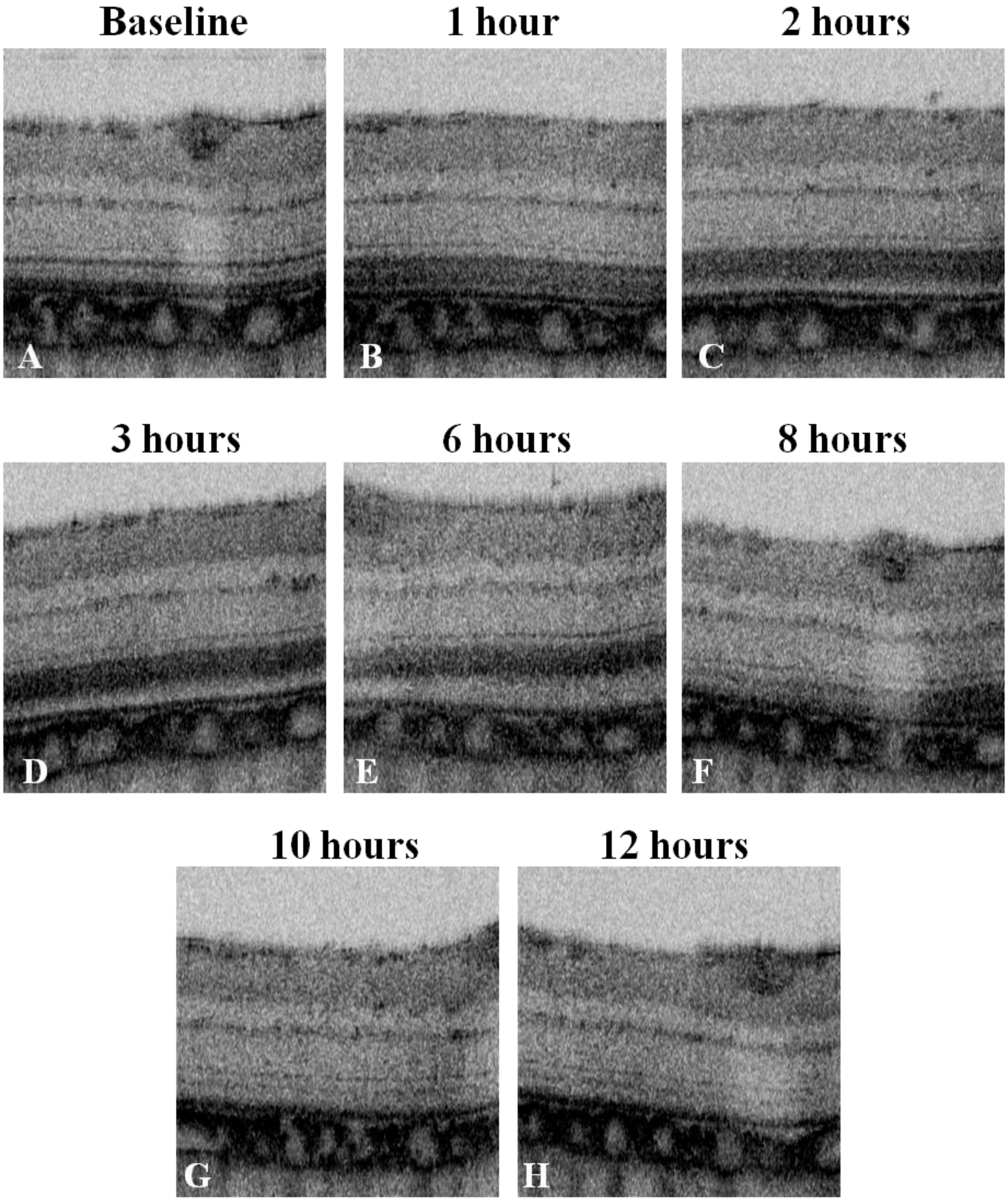

Figure 6.10: OCT tomograms acquired from the central retina over the course of 12 hours from the sixth rat that received sodium iodate as well as a total of 2ml PBS (2 subcutaneous injections at hours 1 and 3 of the study), showing gradual changes to the retina structure as an acute response to the $NaIO_3$ toxicity at: baseline (A) and 1 hour (B), 2 hours (C), 3 hours (D), 6 hours (E), 8 hours (F), 10 hours (G), 12 hours (H) post $NaIO_3$ injection.

For statistical analysis (Fig.6.12 and 6.13), 3D volumetric OCT image sets acquired from three $NaIO_3$-injected (rats used in Fig.6.5,6.6 and 6.7) and three control rats were used. The three treated animals were selected based on the less variability in the timing of the changes. All 3D volumes corresponded to a 1mm x 1mm area from the central region of retina located temporal-superior to the optic nerve head. All 6 rats had received additional subcutaneous PBS injections at 1 and 3 hours post IV drug/vehicle administration. Quantitative thickness and reflectivity measurement was carried out by segmenting individual retinal layers and the choroid in the volumetric data sets acquired at baseline as well as hours 3, 8 and 12 as explained in detail in chapter 3.5.

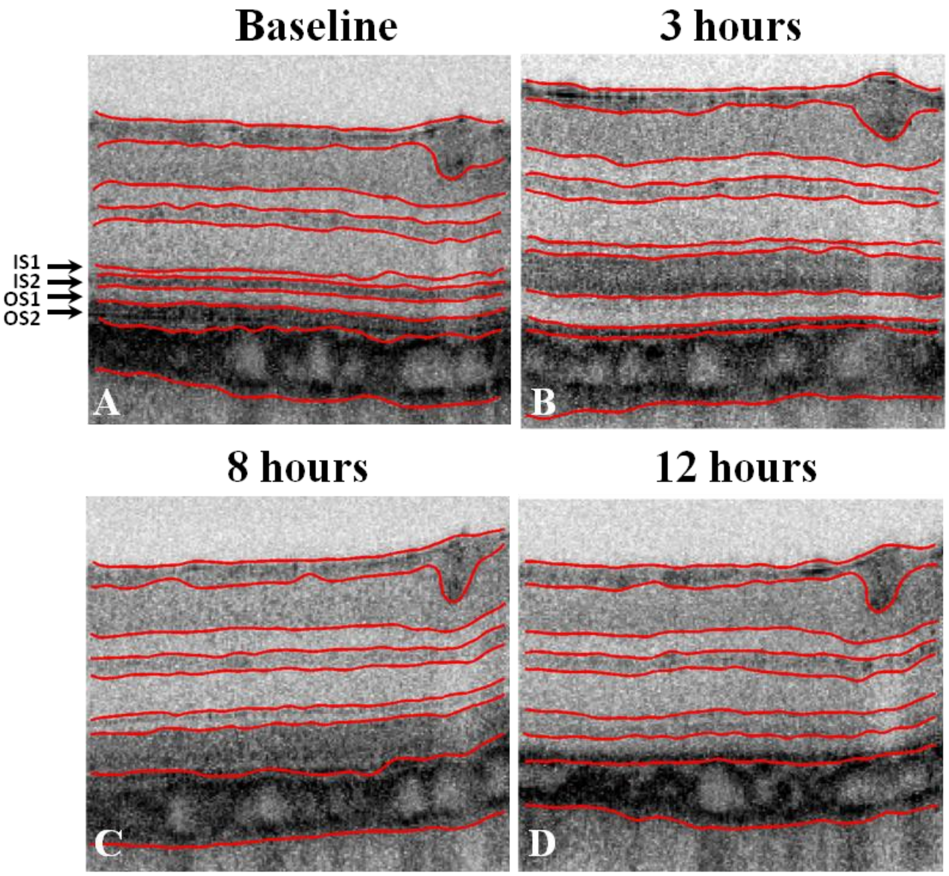

Figure 6.11 Sample segmented OCT images acquired from the same animal at baseline (A), 3 hours (B), 8 hours (C) and 12 hours (D) post drug administration.

Figure 6.11 shows sample segmented OCT images acquired at different time points that were used for the statistical analysis. The baseline image (Fig.6.11A) could be segmented into 9 retinal including 4 PR sub-layers (labeled) and the choroid layer. At 3 hours post injection (Fig.6.11B) the low reflective OS1 band appears darker and is blended with the two bordering layers (IS2 and OS2). The OS2 is separated from the RPE by the low reflective layer (LRL) and a total of 10 layers are segmented at this time. At 8 hours (Fig.6.11C) the LRL has disappeared and a total of 8 layers are segmented including 2 layers in the PR layer. At 12 hours (Fig.6.11D) the same 8 layers as in the 8 hour images were segmented . The OS1 appears low reflective again similar to its baseline appearance. However, the IS2 is less visible and could not be segmented as a separate layer at this time point. A total of 8 layers were segmented in images acquired at 12 hours post drug administration.

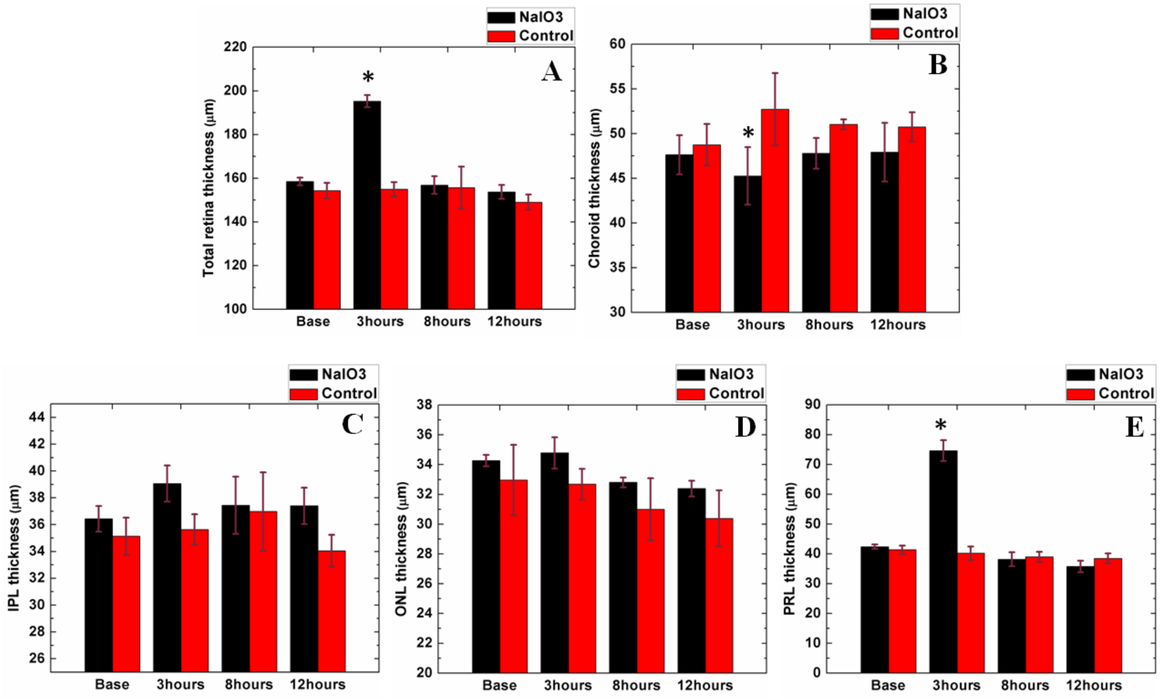

Figure 6.12 The average layer thickness at different imaging time points in three sodium iodate treated and three control rats receiving extra 1mL of subcutaneous PBS injection at hours 1 and 3 post drug administration. Graphs represent thickness of the total retina (A), choroid (B), IPL (C), ONL (D) and PR layer (E). Error bars represent the corresponding standard deviation for each column. Asterisks at each column in the graphs indicate that a statistically significant difference was found for the thickness of the layer at that time point for the experimental animals compared to the corresponding controls.

Figures 6.12 and 6.13 summarize the thickness and reflectivity measurement results from both sodium iodate injected and control groups. The black and red bars represent the average values for the drug injected and the control groups respectively. Error bars depict one standard deviation in the graphs. Here, the ELM was visible at all time points hence the PR layer was measured from ELM to RPE (including the LRL when applicable). The total retina was measured from the NFL to the RPE.

Statistical analysis across the IPL, ONL, PR layer and choroid showed that the layer thickness differed across time points and this difference was also different between experimental animals and controls (Layers*Time point*Group F=49.282; p<0.00005).

Post-hoc analysis revealed that the photoreceptor layer (Fig.6.12E) in the experimental group was significantly thicker than the control group at the second time point (Dunnett; p=0.000008). The photoreceptor layer of the experimental group was thicker at the second time point than all other layers at any time point of the control group (Dunnett; all p<0.05). Also at the second time point, the choroid layer (Fig.6.12B) was significantly thinner in the experimental group than in the control group (Dunnett; p=0.006). Otherwise, there were no differences between the control and experimental groups for each layer at all other time points (Dunnett; all p>0.05).

Analysis of the total retina thickness (Fig.6.12A) showed that it differed across time points and this difference was different between experimental and control groups (Time point*Group F=38.274; p=0.0000).

Post-hoc analysis revealed that the retinal thickness in the experimental group was significantly thicker than the control group at the second time point (Dunnett; p=0.000009). There was no difference between the control and experimental groups for all other time points (Dunnett; all p>0.05).

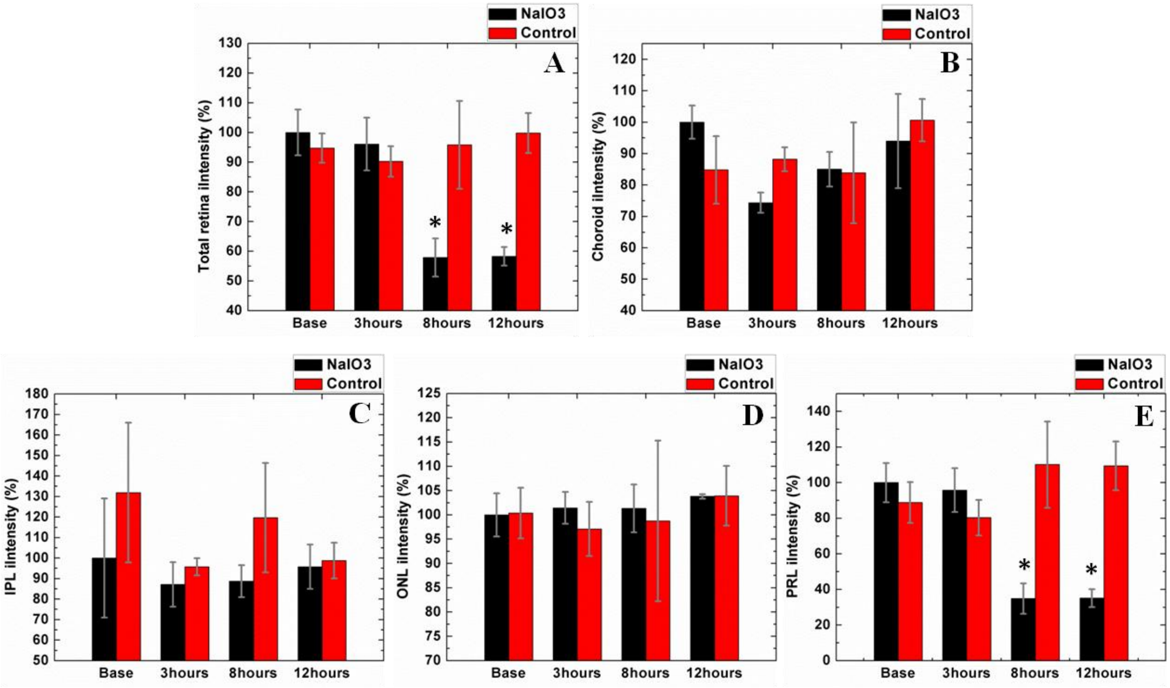

Figure6.13. The average layer reflectivity (intensity) at different imaging time points in three sodium iodate treated and three control rats receiving extra 1mL of subcutaneous PBS injection at hours 1 and 3 post drug administration. Graphs represent total retina (A), choroid (B), IPL (C), ONL (D) and PR layer (E). Error bars represent the corresponding standard deviation for each column. Asterisks at each column in the graphs indicate that a statistically significant difference was found for the reflectivity of the layer at that time point for the experimental animals from the corresponding controls.

Figure 6.13 represents the average reflectivity (intensity) changes in the tissue over time within the first 12 hours of sodium iodate injection. Similar to chapter 5, the average intensities of each layer as well as the total retina and choroid were normalized to that of the corresponding IPL to compensate for image contrast variability during the different imaging sessions due to slight variation in the system performance, light coupling in the animal eye, and possible differences in the image quality in different animals. The normalization was not performed on IPL values to preserve any possible variability in this layer. This normalization was based on the assumption that the IPL remained unaffected in response to sodium iodate-induced outer retina degeneration. The reflectivity values are presented in percentage by setting the baseline value as 100% for convenient comparison.

Results showed that there was no significant difference in intensity between the experimental and control groups across layers at each time point (Layers*Time point*Group F=1.1774; p=0.338).

There was a significant difference between the intensity measure for layers and this was different between time points (Layers*Time point, F=2.3086; p=0.036). Post-hoc analysis revealed that the inner plexiform layer (IPL, Fig.6.13C) had significantly higher intensity than all other layers (Tukey; all p<0.001) and the intensity of the IPL was significantly higher at time point 1 than time point 2 (Tukey; p=0.001) and time point 4 (Tukey; p=0.036).

When evaluating the total retina intensity (Fig.6.13A), there was a significant difference between intensities of the experimental and control group that was different between time points (Time point*Group, F=55.39; p=0.00001). Post-hoc analysis revealed that the experimental group had significantly lower intensity at time point 3 (Dunnet; p=0.000001) and time point 4 than the control group (Dunnett; p=0.0000006). The total retina intensity in the experimental group at time points 3 and 4 were significantly lower that time points 1 and 2 (Dunnet; all p<0.00005).

The significantly higher IPL intensity compared to other layers is due to the fact that the intensity of the other layers have been normalized to the IPL (divided by the corresponding IPL value) hence, resulting in significantly smaller values for the relative intensities of other retinal layers. When considering all layers together the error term of the ANOVA is driven by the magnitude of the IPL response, resulting in any relative differences in the lower intensity layers to be masked. Two way repeated measures ANOVAs were therefore performed for each layer to assess the changes in individual layers over time.

Results showed no significant difference between the intensities of the experimental and control groups in different time points in the choroid (Fig.6.13B, Time point*Group, F=3.11908; p=0.13537). For the ONL (Fig.6.13D), results showed that there was no significant difference between the intensities of the experimental and control groups at different time points (Time point*Group, F= 0.16761; p=0.779).

The PR layer (Fig.6.13E) showed significant difference between the experimental and control groups that was different between time points (Time point*Group, F=101.34377;

p=0.00006). Post-hoc analysis on the PR layer revealed that the experimental group had significantly lower intensity at time point 3 (Dunnett; p=0.0000001) and time point 4 than the control group (Dunnett; p=0.0000001). The intensites of the PR layer in the experimental group at time points 3 and 4 were significantly lower that time points 1 and 2 (Dunnet; all p<0.00005).

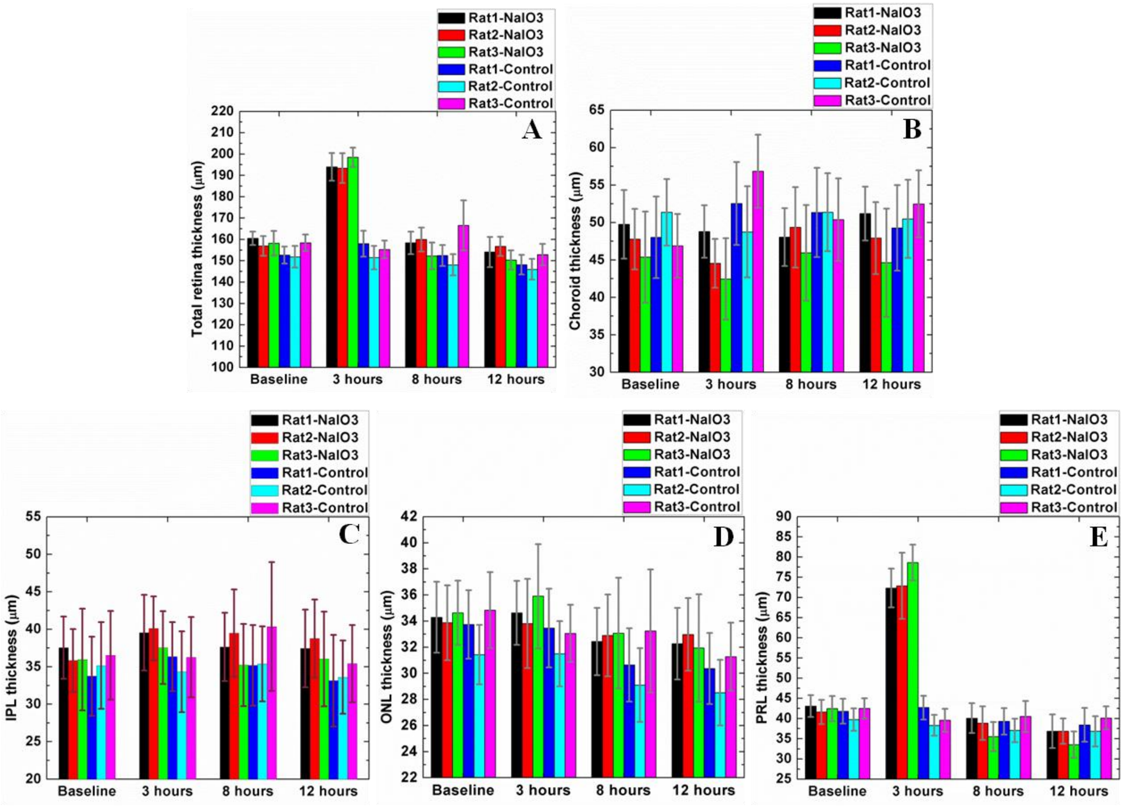

Figure6.14 average thickness for individual sodium iodate injected (n=3) and control (n=3) rats for total retina (A), choroid (B), IPL (C), ONL (D) and PR layer (E). Error bars represent standard deviation.

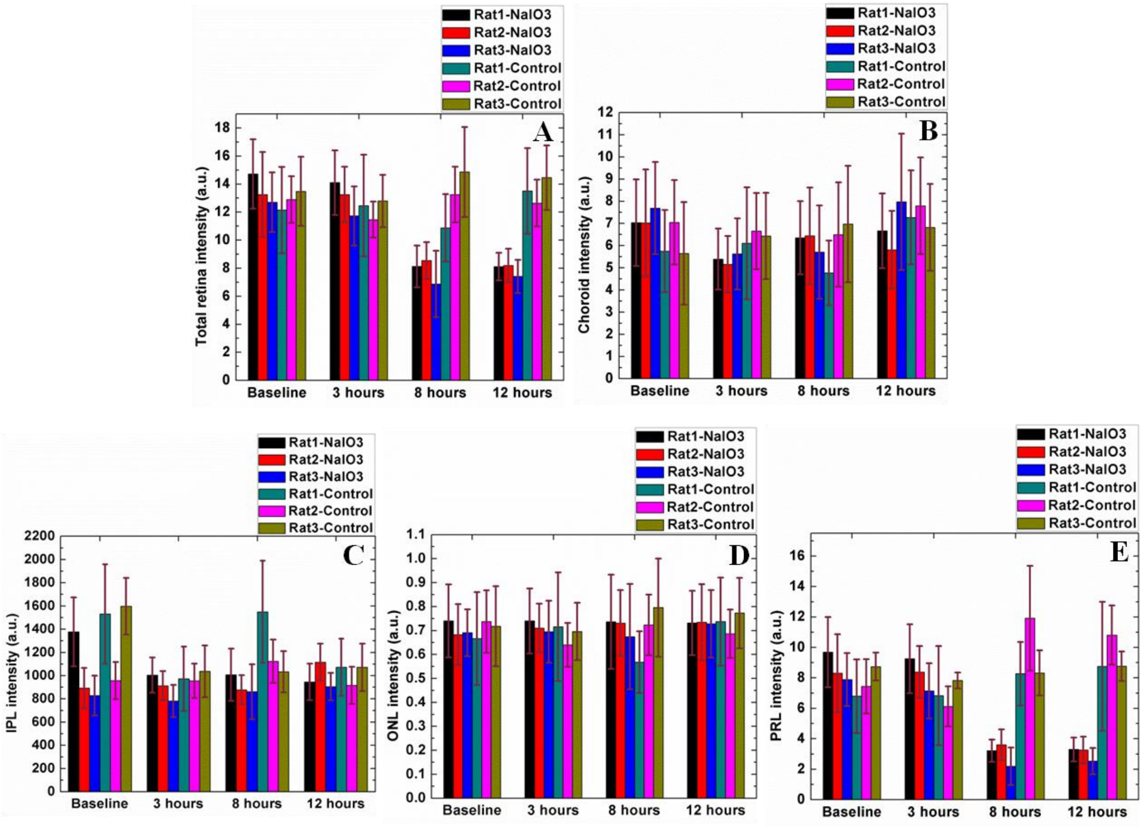

Figure6.15 average reflectivity for individual sodium iodate injected (n=3) and control (n=3) rats for total retina (A), choroid (B), IPL (C), ONL (D) and PR layer (E). Error bars represent standard deviation.

Figures 6.14 and 6.15 show the thickness and reflectivity variations in individual animals (the 3 experiment and the 3 controls) used for the statistical analysis. As depicted in Fig.6.14 and 6.15, the individual animal behaviour follows the same trend as in the averaged behaviour shown in Fig.6.12 and Fig.6.13 for thickness and reflectivity changes over time in both control and experiment groups.

6.6 Discussion

Results from this study suggest that the acute effect of sodium iodate toxicity on the rat retina could vary from animal to animal depending on the animal physiological response to the drug. The strongest variation in the observed morphological changes in the retina was observed in the group of animals that were not hydrated with PBS injections (Figures 6.3 and 6.4). These animals also showed severe adverse side effects to the drug toxicity such as blood in the urine. The severity of the side effects and the variability of the data was much stronger in this case compared to the animals used for the long-term study who had received the same dose of the drug (chapter 5). This is most likely because in the case of the long-term study the animals were injected early in the morning (~9am) and were anesthetized and imaged 6 hours after the injection. In the short-term study however, animals were injected with the drug and then anesthetized for imaging immediately and later every few hours and were less likely to eat and drink to help the toxin get metabolized and eliminated. In addition, the combination of the sodium iodate and repeated isoflurane (anesthesia) could have potentially made it harder for the body to handle the acute toxicity. However, none of the previous short-term studies have mentioned any observed side effects as a result of sodium iodate administration most likely because the majority of the studies have used *ex vivo* methods. These side effects led us to decide to administer extra PBS to animals to hydrate the body and help metabolize the toxin and to reduce the adverse side effects.

The second group of animals that were hydrated with PBS injections during the first 3 hours post sodium iodate injection, showed less inter-animal variability in the retinal morphological changes observed with UHR-OCT (Fig.6.5) and had considerably less adverse side effects to the drug. It appears that availability of the extra hydration has helped the body to handle the acute sodium iodate toxicity more efficiently. Results showed the formation of an additional LRL between the PR OS layer and the RPE. Considering its very low optical reflectivity and dynamics (appearance and disappearance on a time scale of only a few hours) and the fact that this layer has not been observed in studies using histological preparation, the author suggests that the LRL most likely corresponds to fluid accumulation in the sub-retinal space resulting from early breakdown of the choroidal blood retina barrier and loss of RPE adhesion and active outward transport , as an acute response to the sodium iodate toxicity. This fluid accumulation is followed by changes in the photoreceptor layer structure. The OS1 which is low reflective in normal retina becomes darker gradually (at 3-6 hours post drug injection) turning the outer segment into a homogeneous highly reflective band above the LRL. The timing of this alteration is consistent with the observed disorganizations in the PR outer segment discs in electron microscopy images[116]. It is possible that the photoreceptor-RPE detachment and impaired RPE function disrupt the outer segment disc phagocytosis and could lead to disc accumulation and disorganization in the PR outer segment. In this case, it is likely that increased

OS1 reflectivity is partly due to the initial misalignment and accumulation of outer segment discs leading to increased scattering. In addition, fluid flow into the OS layers could disrupt their normal organization.

Observations of individual animals and statistical analysis of the 3 sodium iodate injected and 3 control animals (Fig.6.12 and Fig.6.13) show that the changes in the total retina and PR layer thickness and reflectivity correspond well with the dynamics of the LRL and alterations observed in the PR layer (which includes the LRL). The PR layer thickness was significantly increased compared to the control by ~85% (~34 µm) three hours after drug injection (Fig.6.12E) due to formation of the LRL resulting in a ~25% (~40 µm) increase in the total retina thickness (Fig.6.12A). As the fluid in the LRL subsides, the thickness of both PR and total retina decrease and return to the values not significantly different from the controls at hours 8 and 12. The choroid thickness decreased significantly by ~14% (~7 µm) compared to the control 3 hours post drug administration.

Reflectivity change in the total retina also corresponds well with the PR layer. The PR layer intensity (Fig.6.13E) decreased significantly relative to the controls by ~75% and 74% respectively at 8 and 12 hours post-injection. This was due to clearing of the highly reflective material previously observed in the PR space as well as reduced reflectivity of the dark IS2 and OS2 bands. Similar changes were observed in the total retina with significantly lower intensity at 8 and 12 hours relative to the controls (~38% and ~41% decrease respectively) (Fig.6.13A). As seen in the statistical results, the existence of the LRL at 3 hours did not significantly affect the overall reflectivity of the PR and total retina layer. As the LRL grows to a size almost equal to 50% of the whole PR layer thickness, the OS1 changes from low to high reflectivity leaving the overall PR reflectivity (from ELM to RPE) similar to the control value. On the other hand, as the PR and total retina thickness (Figs.6.12E&A) return to the normal values (control group) at hours 8 and 12 post drug injection, their intensities decrease significantly (Figs.6.13E&A) due to restoration of the OS1 normal apparent reflectivity (low reflective band) as well as the overall reduced IS2 and OS2 contrast (Figs.6.5F&H).

As mentioned before, the three treated animals used for segmentation and statistical analyses were selected based on the less variability in the timing of the changes. However, to confirm the results presented in this study, animals showing the full range of outcomes need to be analyzed statistically.

Although the time points of the measurements in this study and the previous study (chapter 5) were different, a general trend of the changes was observed in close time points. Formation of the LRL and increase reflectivity in the OS1 Band was observed in both studies within the first 6 hours of the treatment. The PR layer appeared similar in OCT tomograms at day 1(chapter 5, long term study) and hour 12 (chapter 6, short term study) where both showed reduced contrast of the high reflective IS2 and OS2 bands.

6.7 Conclusion

In this chapter, the acute effect of sodium iodate on the layered structure of rat retina was observed and studied *in vivo* for the first time, using high speed UHR-OCT. The quantitative statistical analysis of the results showed a significant change in the thickness of total retina, PRL and choroid at 3 hours and significant change in the reflectivity of total retina and PRL at 8 and 12 hours post drug administration. This suggests that thickness and reflectivity measurements could provide useful information about changes in the retina. In other words, when monitoring retina with 3D UHR-OCT, both thickness and intensity could be used as useful markers in detecting local and global abnormalities.

Chapter 7

Discussion and Conclusion

This PhD project had two major goals: a) to improve the axial OCT imaging resolution for retinal imaging applications (human and rodent eye), by investigating the limiting factors to the axial OCT resolution in the rodent and human retina and implementing novel technologies such as novel light sources and detectors; and b) to demonstrate the advantages of UHR-OCT technology for non-invasive imaging and characterization of outer retinal degeneration in an animal model.

Spectral shaping was proposed as a method for improving the axial resolution in the human and rodent retina of UHR-OCT systems designed for the 1060 nm wavelength region and its effectiveness was tested both theoretically through a new computational model, and experimentally, by utilizing a novel, custom-built light source. The results from the theoretical and experimental studies have not only established the theoretical and practical limits to the highest axial OCT resolution achievable for human and small animal retinas in the 1060 nm spectral range, but also can serve as a guideline to other research groups and OCT manufacturers for development of novel light sources for UHR-OCT at 1060 nm.

Although water absorption plays a major role in determining the highest achievable OCT axial resolution in the *in vivo* retinal imaging at the 1 µm region, other factors such as wavelength-dependant detector sensitivity and system components' optical transition properties pose further limitations to the applicable spectral range and therefore to the highest axial resolution achievable with the current technology. Further development of novel detectors and optical components capable of supporting broader spectral range in the future could potentially improve the practical achievable axial resolution in UHR-OCT systems designed for the 1µm wavelength range.

The resolution-improved state-of-the-art, high speed, UHR-OCT system along with the semi-automatic segmentation algorithm were used to visualize, quantify and monitor the structural and reflectivity changes of the rat retina over time in the toxicity-induced rat model of outer retinal degeneration. The long-term as well as acute effect of sodium iodate on the layered structure of rat retina were observed and quantified *in vivo* for the first time using high speed UHR-OCT.

The observations reported in chapters 5 and 6 correlate well with features observed in previous sodium iodate studies conducted with different modalities. Significant reduction and loss of visual acuity was observed within the first 2 hours post drug injection which indicates disruption in the normal retinal function[116]. Degeneration of the RPE basal membrane, loss of RPE apical microvilli, swollen RPE cytoplasmic organelles within 6 hours post injection were reported as the primary effect seen using electron and light mocroscopy[106]. In addition, when horseradish was injected into the blood stream, RPE cells contained much more horseradish in areas damaged by sodium iodate compared to normal areas while horseradish leakage into the space between photoreceptors was evident[120]. ICG showed hyper-fluorescence scattered over the retinal posterior pole 3 hours after injection indicating leakage from the choriocapillaris[119]. Kinetic vitreous fluorophotometry indicated that free diffusion across the choroidal blood retina barrier had been established[120]. Furthermore, the force of adhesion between RPE and the neural retina was reduced significantly 100 min post injection that indicates reduction of RPE adhesion function[122]. All these observations indicate severe damage to the RPE structure and function within the few hours of sodium iodate injection. The timing of appearance of the low reflective layer between RPE and PR layer observed in UHR-OCT tomograms reported in this thesis correspond well with the timing of the choroidal blood retina barrier breakdown, leakage of CC, and penetration of plasma content into the RPE cells and the space between the photoreceptor cells reported in other studies which strengthens the assumption that this layer is composed of fluid accumulated in the sensory retina due to the loos of RPE barrier and active outward transport functions. It is reasonable to hypothesise that the loss of RPE apical microvilli and reduction of the adhesion force between RPE and PR layer make the connection between the OS and the RPE vulnerable and the available fluid leaks into this space causing the detachment of OS from RPE.

As mentioned before, normal PR function depends on the normal RPE function which is severely disrupted in the case of sodium iodate toxicity. The photoreceptor outer segments were reported to be disorganized 6 hours post drug injection [114]. TUNEL positive photoreceptor cells were detected, indicating the beginning of PR cell apoptosis as soon as 6 hours[106]. The UHR-OCT tomograms acquired within the early hours post injection (1-6 hours) presented in chapters 5 and 6 show that as the OS separates from the RPE, the low reflective OS1 band begins to increase in reflectivity and appears darker until it cannot be distinguished from surrounding dark IS2 and OS2 bands. As explained in chapter 6 (Fig.6.1) the OS1 most likely corresponds to the region of the photoreceptor OS containing double lipid membrane discs. These discs have a very high turnover rate and the shed discs must be digested and eliminated by RPE cells to make space for new discs. However, in this case, the attachment between rod OSs and the RPE cells is lost and therefore, the discs cannot be digested and the disposed properly. Hence, it is likely that the increase in the OS1 reflectivity is due to accumulation and disorganization of excess shed membrane discs which leads to increase in light scattering from this region.

As the fluid layer disappears from the retinal space and the retina comes in contact with RPE again in later time points (6-12 hours), the OS1 band resumes to its normal low reflective appearance (Fig.6.3). This effect could potentially be due to a disorganization of the OS due to fluid flow which dissipates as the accumulated fluid layer dissipates. It is also possible that the RPE still has preserved some of its function at this stage and is able to eliminate the fluid from the sub-retinal space and to clear some of the excess discs and hence OS1 regains its almost normal appearance.

Studies using electron and light microscopy showed disorganization of the outer and inner segments of photoreceptors with flattened individual RPE cells devoid of nuclei at 24 hours[107]. RPE cells were replaced by a thin layer of melanin along the Bruch’s membrane in affected areas and TUNEL positive photoreceptor cell count reached its maximum in day 3[106]. Our OCT tomograms acquired at day 3 (Fig5.1C) show disruption of the multilayered structure integrity of the PR layer (i.e. IS1, IS2, OS1 and OS2) and an almost homogeneous high reflective layer is seen in the location of PR layer. The layer is most likely composed of disorganized and degenerating bodies of dead PR cells and possibly some of the high reflective melanin content from the adjacent dead and decomposing RPE cells.

Previous studies showed that the outer and inner photoreceptor segments were significantly shortened and the ONL thickness (photoreceptor nuclei) was reduced at day 7[107]. 18 and 28 days after, no RPE cover was present and patches of melanin clumps appeared along Bruch’s membrane. There were indications that glial cells might contribute to phagocytosis of melanin remains. The OCT tomograms presented in this thesis showed severe disruption and gradual decomposition of the high reflective material in the outer retina from the day 7 of the study onward. At day 7 (Fig.5.1F), both the OPL and the dark PR layers are disrupted and irregular while clumps of highly reflective material can be seen within the outer retinal space. These clumps are most likely decomposing debris of dead PR and RPE cells and perhaps some glial cells that are up-taking and digesting high reflective melanin that is released from degenerated RPE cells. These clumps reduce in optical reflectivity and size over time until they completely disappear 3 months after, leaving the inner retina in contact with the Bruch's membrane. This was confirmed in histological cross-sections reported in this thesis (Fig.5.1K) as well as in other studies[106].

Results presented in this thesis showed that outer retinal damage can be characterized by changes in the layer thickness, shape, integrity and optical properties of different retinal layers. This study succeeded in detecting and monitoring for the first time the formation and dynamic of the fluid accumulation in the outer retina as an acute response to sodium iodate toxicity. The acute and long-term effects of sodium iodate on the rat retina structure and optical reflectivity were studied for the first time *in vivo*.

Furthermore, when statistically comparing the thickness and reflectivity data, especially in the case of short-term changes (chapter 6), it is interesting to notice that the changes could be significant for the intensity values at some time points that showed no significant change in thickness, while the situation was reversed in some other time points. For instance, the overall thickness was significantly increased at 3 hour post injection while it was not different at 8 and 12 hours. On the other hand, the overall intensity data showed no significant change at 3 hours while it showed significant decrease at 8 and 12 hours post drug administration. In this case considering only thickness or reflectivity data would result in false negatives in reporting the presence of abnormalities. Hence, the quantitative statistical analysis suggests that both thickness and reflectivity measurements could be used as valuable complementary indicators in detecting abnormalities in outer retina degeneration

It is worthwhile to mention that the segmentation algorithm used in this study is not able to detect and eliminate blood vessels. This factor could potentially lead to increased variability in the thickness and reflectivity measurements, especially in the case of large surface blood vessels. However, since the images were taken from approximately the same location of retina and since we average the values whose majority are from non-vesseled locations, it is reasonable to assume that the effect of blood vessels on the measurements is effectively reduced. Furthermore, these large retinal blood vessels are at the surface and mainly affect the NFL and IPL and have minimal effect on the outer retina measurements which are the main focus of this study.

Results from this study could potentially improve our understanding of the mechanisms of outer retina degeneration induced by sodium iodate and the interplay between the early changes in the photoreceptor morphology and disrupted RPE metabolic and barrier function. Although the sodium iodate model is not exactly identical to any of the human outer retina degenerative disease, as mentioned previously in chapter 2.3.3, it is a valuable tool to study different aspects and mechanisms similar to such disease such as rod PR apoptosis, retinal detachment, retinal edema, CC leakage and atrophy to name a few. It could also be useful in investigating novel therapeutic interventions such as stem cell and growth factor applications for regenerating RPE and PR cells, blocking the PR apoptosis pathway, use of anti oxidant substances to reduce or prevent the damage to the neuro-sensory retina.

Moreover, these results demonstrated the potential advantage of UHR-OCT imaging in *in vivo*, non-invasive investigation of animal models of retinal disease. Dynamic changes and features that are not detectable in *ex vivo* methods, such as fluid accumulation, are easily detected in *in vivo* UHR-OCT tomograms. In addition, imaging the same location in the same animal over time is possible which could help reduce the effect of inter-animal differences on the study outcome. The number of animals required for the study is also significantly reduced since all animals can be used for all measurements and there is no need for euthanizing a number of animals at each stage.

The UHR-OCT system described here is capable of detecting small changes in the retina structure and optical properties and hence can be used in clinical settings for accurate *in vivo* evaluation of human retina (appendix A). However, volumetric OCT imaging of human retina results in huge amount of data, making it impractical for physicians to review individual B-scans for every patient. Therefore, as presented in this thesis, utilizing simultaneous thickness and reflectivity information from individual retinal layers using suitable segmentation algorithms makes the quantitative evaluation of retinal images possible and reduces the time and cost required for data analysis. Furthermore, this method could also be used to set a quantitative baseline measurement for individual patients for future reference and would potentially improve diagnostic accuracy in retinal abnormalities.

In terms of the future directions of this project, a number of steps can be suggested. To confirm the changes reported here in the study of the long term and short term effect of sodium iodate on the thickness and reflectivity of retinal layers, statistical analysis on the data from single animals (intra-animal variability) must be performed. It would also be helpful to use other OCT methods such as spectroscopic and polarization sensitive OCT to gain more information about the optical property changes occurring in the tissue over time. In addition, monitoring the changes in the retina with a number of *in vivo* modalities such as OCT, FAF and FA and comparing the results would be a necessary next step. OCT provides a high definition cross-sectional image of the retina structure and reflectivity profile. FAF provides real time information about the fluorescence material in the retina, especially the lipofuscin in the RPE which provides information about the RPE function. And, FA provides information about the choroidal blood retina barrier integrity. The combined information regarding retinal tissue morphology, optical properties, RPE function and CC integrity could potentially lead to better understanding of the origin, mechanism and the sequential order of changes which could in turn provide further insight into the nature of outer retina degeneration.

In this thesis, a small 1 mm x 1 mm area was imaged. It would be interesting to look at the changes within a larger area to monitor *in vivo* the drug effect on both central and peripheral retina.

To make more accurate measurements, it is important to image the same location over time. An *en face* camera, eye motion tracker and data registration algorithms can be used to image exact same location in each imaging session. This way, exact B-scans can be compared to gain more precise information about the changes in fine features such as the capillary network in the retina and the choroid.

Further improvements in segmentation algorithms will be an important next step. The segmentation algorithm used in this project is semi automated and still requires the user's guidance in segmenting each B-scan. This procedure makes segmentation of large amount of data very time consuming. A fully automated, high speed layer segmentation algorithm would provide the means for quantifying multiple 3D sets from the same time point acquired from the same animal, more time points within the study and larger number of animals to improve the strength of the statistical analysis.

Appendix A

In Vivo Human Retina Imaging with 5µm Axial Resolution at 92kHz with a 1060nm Spectral Domain Optical Coherence Tomography System

This appendix is based on the following SPIE proceeding:
S. Hariri, P. J. Lee, A. A. Moayed, and K. Bizheva, "In-vivo human retina imaging with 5µm axial resolution, at 92000 A-scans/s with 1µm spectral domain OCT system," Proceedings of SPIE, vol. 7889, no. 1, p. 78890K–78890K–5, Feb. 2011.[21]

The UHR-OCT system used for this study and the human imaging interface was designed and built by Dr. Kostadinka Bizheva. She has also overseen the novel camera implementation and testing, all imaging sessions and the manuscript preparation.

A.A.Moayed assisted with imaging, data processing, 3D reconstruction and revising and proofreading the manuscript.

P. J. Lee assisted with imaging and image processing as well as making modifications to the imaging code (Labview) to be compatible with the novel camera used in this study.

Interfacing the novel camera with the OCT system and characterizing the system performance, assistance with the design and testing of the human imaging interface, participation in imaging session (operating the system), data processing and selection and preparing the manuscript are the author's work.

The author would like to gratefully acknowledge Doug Malchow from Goodrich Corporation for providing the novel CCD camera used in this study, Saad Shakeel and Donghyun Lee for assistance with image processing, Dr. Natalie Hutchings, Dr. Trefford Simpson and Jyotsna Maram from University of Waterloo, school of optometry for participation in the image acquisition sessions as volunteers. This work was supported by NSERC and University of Waterloo Start-up grants.

Overview: A prototype, linear array InGaAs camera and a spectrally reshaped, superluminescent diode based light source were integrated into a 1060 nm spectral domain optical coherence tomography system to achieve 5 µm axial resolution in the human retina in vivo at image acquisition rate of 91,911 A-scans/s. 3 dB sensitivity loss was observed at 92 kHz readout rate (7 µs integration time) of the camera, as compared to similar, commercially available cameras with 47 kHz readout rate (14 µs integration time). The improved image acquisition rate resulted in fewer motion artefacts in volumetric retinal images, while the improved axial resolution allowed for better visualization of fine morphological details such as retinal and choroidal capillaries and individual nerve fiber bundles at the raphe and the optical nerve head.

A.1 Introduction

Recent studies have demonstrated the advantages of ultrahigh resolution optical coherence tomography (UHR-OCT) technology for retinal imaging at 1060 nm, in terms of visualization of the entire choroid[137], [138], [143], [167], [168] and improved image quality in patients with cataract[138]. Other studies have proven the value of 1060nm UHTOCT for measurement of total choroidal thickness in normal and cataract patients[169], [170]. Large scale, high resolution, high density volumetric imaging of the human retina has significant clinical value, however it requires extended acquisition time, which subjects the images to artefacts related to involuntary eye / head motion. Most recent retinal studies with 1060 nm spectral domain OCT (sdOCT) achieved 7µm axial resolution and 47,000 A-scans/s image acquisition rate in the human retina[137],[138],[143],[150][167]. High speed (236,000 A-scans/s) swept source OCT (ssOCT) retinal imaging at 1060nm was also reported[141], however, the achieved axial resolution was limited to 15µm.

Here we present a combination of a prototype InGaAs 1024 pixel, linear array camera with 92 kHz readout rate and a superluminescent diodes (SLD) based light source with spectrally reshaped output, that allows for *in vivo* imaging of the human retina with a 1060 nm sdOCT with 5 µm axial resolution at image acquisition rate of 91,911 A-scans/s.

A.2 Methods

Water absorption in the 1060 nm spectral region limits the maximum available spectral bandwidth useful for retinal imaging and thus, theoretically restricts the maximum achievable axial OCT resolution to ~5.2 µm. By using a computational model (chapter 4) it was demonstrated theoretically, that this limitation can be overcome through the use of spectral shaping. Here, the experimental verification of the model is presented. The output of a commercially available dual SLD light source (Superlum, λc = 1020 nm, $\Delta\lambda$ = 108 nm, P_{out} = 10 mW) was spectrally reshaped to increase the optical power at ~980nm relative to 1060nm by increasing the current to the SLD with spectral output centered at that wavelength. The resulting output spectrum is shown in Fig.A.1A (black line), while the dashed line corresponds to the water absorption profile in the same spectral region[171].

The modified light source was interfaced with a compact, fiber-based sdOCT system[51]. The sample arm of the system was connected to a modified slitlamp biomicroscope. The interference signal was detected with a high performance spectrometer (P&P Optica), outfitted with a prototype linear array, 1024 pixel InGaAs camera (SUI, Goodrich Corp.) with 92 kHz readout rate.

A 25 mm long water cell (corresponding to the average length of a human adult eye) and a mirror were used in the sample arm to measure the effect of water absorption on the spectral output of the modified SLD, resulting in the spectrum shown in Fig.A.1A (grey line). Another 25 mm long water cell was inserted in the reference arm to compensate for the water content in the sample arm (i.e. 25 mm water cell when measuring the spectrum and water content of the human subject when performing OCT imaging).

The system's axial point-spread function (PSF) measured from a mirror reflection in the sample arm is shown in Fig.A.1B. Since the spectrum was measured at the OCT detection end, the effect of system's optical components and the detector were automatically included in the results. The use of the spectrally reshaped light source resulted in 7 µm axial resolution measured in free space, corresponding to ~5µm resolution in the human retina, assuming an average refractive index of 1.38 for retinal tissue. Another method for measuring the axial resolution is to perform cross-correlation of the sample and reference spectra, perform FT on the result and then measure the FWHM of the PSF. This procedure was done on the sample and reference spectra measure after double pass through 25 mm water cells and the axial resolution was measured to be 6.3μm in air (Fig.A.1C) which is within the 10% from the measured value.

The imaging beam diameter was 3 mm at the cornea, which will lead to ~6.9 μm diffraction limited lateral resolution in the human retina for 1020 nm central wavelength.

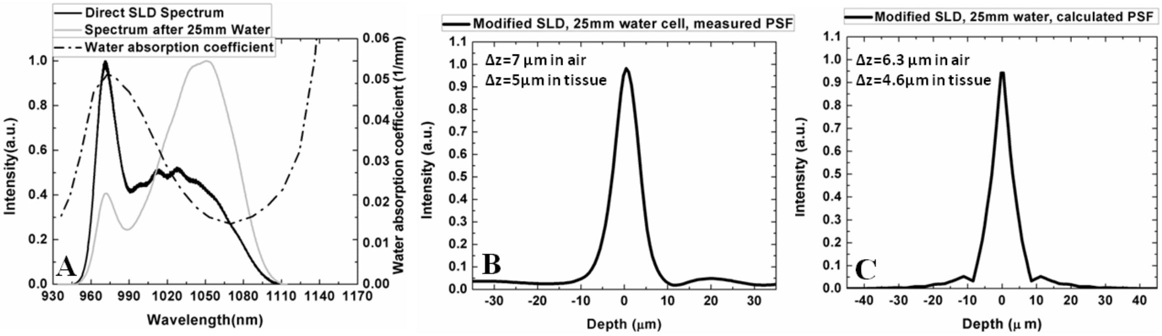

Fig.A.1 SLD spectrum measured directly at the source (black line), after a double pass though a 25mm long water cell (grey line) and the water absorption coefficient (dashed line) (A). Axial PSF of the sdOCT system measured from a mirror reflection with 25mm water cells in the reference and sample arms of the system (B). The axial PSF calculated by cross-correlating the sample and reference arm spectra after double pass through 25mm water cells in sample and reference arms (C). Since the spectra are measured at the OCT detection end, the effect of system's optical components and the detector are automatically included in the results. (Figure reproduced with modifications from [21] with permission from the journal)

A.3 Results and Discussion

To evaluate the effect of the camera integration time on the sensitivity of the sdOCT system, measurements were carried out with integration times of 7 μs (corresponding to 92 kHz readout rate) and 14 μs (corresponding to currently commercially available InGaAs cameras with 47 kHz readout rate). SNR of 95 dB for 7 μs and 98 dB for 14 μs integration time was measured for 1.6 mW optical power of the imaging beam. The loss of 3 dB is consistent with the theoretically expected decrease in sensitivity at the shorter integration time.

To demonstrate the effect of reduced integration time on the sdOCT image contrast, retinal tomograms (512 x 512) were acquired from the fovea of healthy subjects at 92 kHz (7 μs integration time) and 56 kHz (14 μs) readout rate. The imaging power incident on the cornea was set to 1.5 mW, below the 1.9m W ANSI standard limit (for continuous beam viewing for 10 s) for retinal imaging at1060 nm. The imaging procedure was approved by the University of Waterloo Human Ethics committee. Figure 2 shows comparison of two representative tomograms acquired with at 7 µs (A) and 14 µs (B) integration times. Both images were processed with the same grey scale. The retinal tomogram acquired with 7 µs integration time (Fig.A.2A) showed overall lower image contrast and reduced visibility of the choroidal vasculature (dashed arrows), as compared to the tomogram acquired with 14 µs integration time (Fig.A.2B).

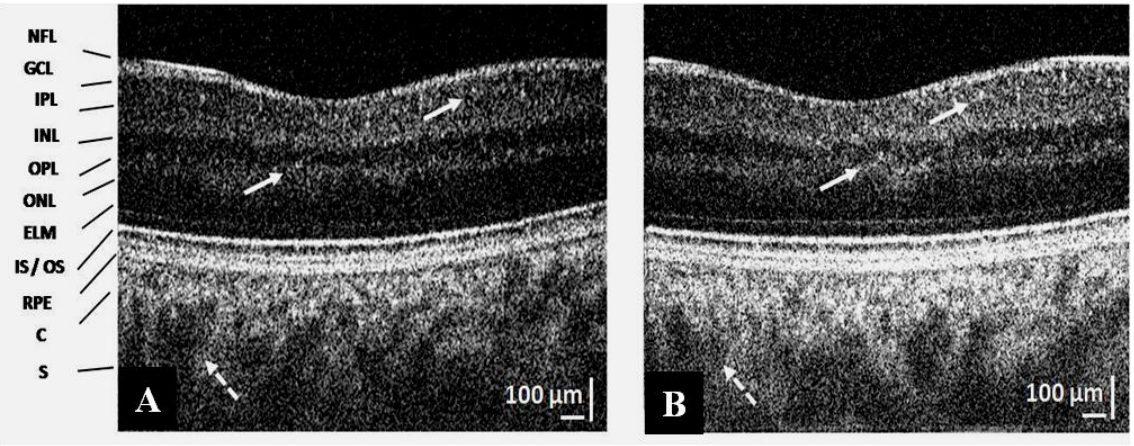

Fig.A.2 Representative cross-sectional retinal tomograms (512 x 512) acquired near the fovea with the fast (7µs, 92kHz) and slow (14µs, 56kHz) settings of the camera. The solid arrows mark capillaries in the inner retina, while the dashed arrows mark choroidal vasculature. (Figure reproduced from[21] with permission from the journal)

The image SNR calculated from the two retinal tomograms showed a difference of ~3dB, consistent with the system SNR measurements. To calculate the SNR of the individual images, a simple Matlab code was written (by the author) to calculate the SNR of all 100 A-scans of the tomogram, and select the maximum value, which would correspond to the A-scan with the highest ratio of the signal/noise variance within a B-scan. The noise variance was measure from the pixels corresponding to the area above the tissue in the A-scan. Regardless of the 3 dB loss in SNR, all retinal layers, the retinal capillaries and the choroidal vasculature are still clearly visible in the tomograms acquired at 92 kHz readout rate.

To demonstrate the effect of the improved axial resolution and high image acquisition speed on the overall image quality, volumetric (512 x 512 x 512) retinal OCT tomograms were acquired from the fovea and optic nerve head of healthy human subjects. Figure 3 is based on the volumetric sets acquired at the fovea (Fig.A.3A) and the optic disk (Fig.A.3B) with the 7 µs integration time of the camera. *En-face* sections from the 3D sets show clear visualization of the raphe (white arrow) in the foveal region with distinct nerve fiber bundles (Fig.A.3A) and the fiber meshwork of the lamina cribrosa in the optic nerve head (Fig.A.3B, white arrow).

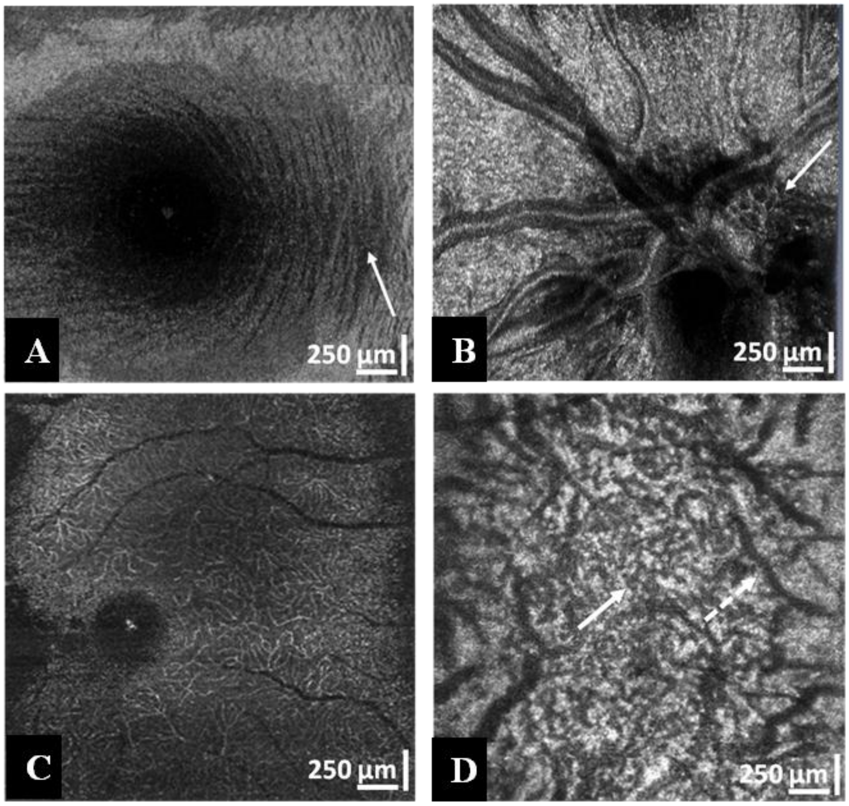

Fig.A.3 *en face* cross-sections acquired from volumetric retinal tomograms from the fovea (A) and the optic nerve head (B). Arrows point at the nerve fiber bundles at the raphe (A) and the lamina cribrosa (B). *En-face* images of the fovea showing the capillaries at the IPL(C) and choroidal vasculature (D), choriocapillaris (solid arrow) and larger choroidal blood vessels (dashed arrow). Image dimensions: 512 x 512 x512 corresponding to 2.5mm x 2.5mm x 1mm. (Figure reproduced from[21] with permission from the journal)

A transverse cross-section at the retinal inner plexiform layer (Fig.A.3C) reveals the intricate network of retinal capillaries near the fovea. A second transverse image (Fig.A.3D) obtained below the retinal pigmented epithelium (RPE) shows clearly individual choriocapillaris in the center (solid arrow) and larger choroidal vessels (dashed arrow) at the edges of the image frame (images were not corrected for the retinal curvature).

Representative 2D cross-sectional scans from the fovea and the optic discs are shown in Fig.A.4A and 4B respectively. The border between the choroid and the sclera (Fig.A.4A, white arrow) and the nerve fibers in the lamina cribrosa (Fig.A.4B, white arrow) at large depths are clearly visible regardless of the 3dB loss of sensitivity due to the higher image acquisition rate.

The effect of the improved axial OCT resolution on the image quality is best observed in the selected *en face* frames from the volumetric images shown in Fig.A.4C-F. Individual nerve fiber bundles in the raphe (Fig.A.4C), an *en face* view of the fovea (Fig.A.4D), a fine network of capillaries (~20µm in diameter) in the retinal outer plexiform layer (Fig.A.4E), the intricate loops of the choriocapillaris (Fig.A.4F) are clearly visible in the en-face images.

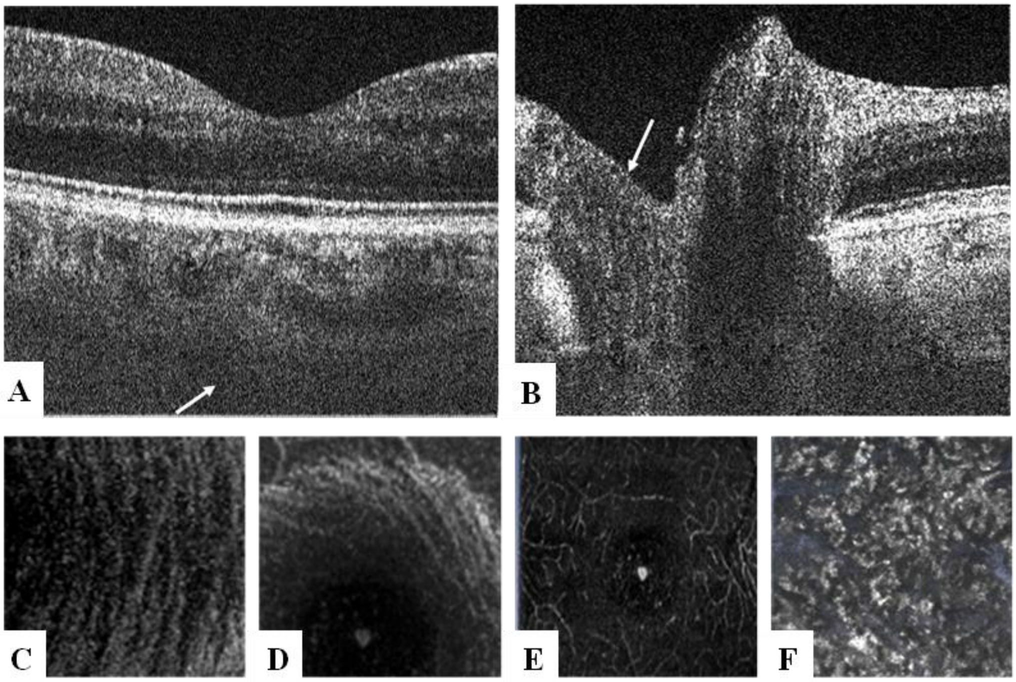

Fig.A.4 Representative cross-sectional images acquired at the fovea (A) and the optic nerve head (B). Arrows mark the choroid-to-sclera border (C) and the nerve fibers at the lamina cribrosa (B). Enlarged *en-face* images of individual nerve fiber bundles at the raphe (C); an *en face* view of the fovea (D); capillaries at the OPL (E); and choriocapillaris (F). (Figure reproduced from[21] with permission from the journal)

A.4 Conclusion

In this study, the *in vivo* imaging of the human retina with 5 µm axial OCT resolution at image acquisition rate of 91,911 A-scans/s with a 1060 nm SD-OCT system were presented for the first time. The improved performance of the imaging system allowed for acquisition of volumetric images of the retina with reduced motion artifacts, as well as better visualization of small morphological details in the retina.

Copyright Permission

1. Journal Permission

from: Sepideh Hariri <sepidhariri@gmail.com>
to: jbo@spie.org
date: Thu, Jan 17, 2013 at 11:10 PM
subject: permission for using paper content in PhD thesis

Hi,

I am a PhD student at University of Waterloo, Canada. I would like to use my newly accepted paper material as a part of my PhD Thesis.

Could you please let me know how to proceed to acquire an official permission from your journal?

My paper information is:

Sepideh Hariri, Man Chun Tam, Donghyun Lee, Denise Hileeto, Alireza Akhlagh Moayed, and Kostadinka Bizheva,"Noninvasive imaging of the early effect of sodium iodate toxicity in a rat model of outer retina degeneration with spectral domain optical coherence tomography",Paper 12591 received Sep. 6, 2012; revised manuscript received Dec. 20, 2012; accepted for publication Jan. 2, 2013.

Please let me know if you can give me the volume and issue number in which the paper will be printed.

Thank you in advance for your kind attention.

Best regards

--

Sepideh Hariri

PhD Candidate

Department of Physics and Astronomy

University of Waterloo

200 University Ave West

Waterloo, Ontario Canada N2L 3G1

(519) 888 4567 ext. 35665
shariri@sciborg.uwaterloo.ca

from: Karen Thomas <karent@spie.org>
to: "sepidhariri@gmail.com" <sepidhariri@gmail.com>
date: Fri, Jan 18, 2013 at 3:38 PM
subject: RE: permission for using paper content in PhD thesis

Dear Sepideh,

Thank you for seeking permission from SPIE to reprint material from our publications. As author, SPIE shares the copyright with you, so you retain the right to reproduce your paper in part or in whole.

Your paper, “Noninvasive imaging of the early effect of sodium iodate toxicity in a rat model of outer retina degeneration with spectral domain optical coherence tomography," will appear in the *Journal of Biomedical Optics*, Feb. 2013. Issue 2, Vol. 18.

Publisher's permission is hereby granted under the following conditions:

(1) the material to be used has appeared in our publication without credit or acknowledgment to another source; and

(2) you credit the original SPIE publication. Include the authors' names, title of paper, volume title, SPIE volume number, and year of publication in your credit statement.

Sincerely,

Karen Thomas for

Eric Pepper, Director of Publications

SPIE

P.O. Box 10, Bellingham WA 98227-0010 USA

360/676-3290 (Pacific Time) eric@spie.org

****

from: Sepideh Hariri <sepidhariri@gmail.com>
to: iostrin@arvo.org
date: Tue, Aug 14, 2012 at 12:34 PM
subject: permission for using paper content in PhD thesis

Hi,

I am a PhD student at University of Waterloo, Canada. I would like to use my paper material as a part of my PhD Thesis.

Could you please let me know how to proceed to acquire an official permission from your journal?

My paper information is:

Hariri S, Moayed AA, Choh V, Bizheva K.,"In vivo assessment of thickness and reflectivity in a rat outer retinal degeneration model with ultrahigh resolution optical coherence tomography.", IOVS, 18;53(4):1982-9. Print 2012 Apr.

Thank you in advance for your kind attention.

Best regards

--

Sepideh Hariri
PhD Candidate

Department of Physics and Astronomy
University of Waterloo
200 University Ave West
Waterloo, Ontario Canada N2L 3G1
(519) 888 4567 ext. 35665
shariri@sciborg.uwaterloo.ca

from: Ilana R. Ostrin <iostrin@arvo.org>
to: Sepideh Hariri <sepidhariri@gmail.com>
date: Tue, Aug 14, 2012 at 1:16 PM
subject: RE: permission for using paper content in PhD thesis

Dr. Hariri,

Congratulations on reaching your thesis. Permission is hereby granted to include your IOVS article in your thesis. A reprint of this material must include a full article citation and acknowledge ARVO as the copyright holder.

Thank you for inquiring.

Best,

Ilana Ostrin

Editorial Assistant

Association for Research in Vision and Ophthalmology (ARVO)

1801 Rockville Pike, Suite 400

Rockville, MD 20852 U.S.A.

Main: +1.240.221.2900 | Direct: +1.240.221.2921 | Fax: +1.240. 221.0370

iostrin@arvo.org

Investigative Ophthalmology & Visual Science

****

from: Sepideh Hariri <sepidhariri@gmail.com>
to: Authorhelp@spie.org
date: Tue, Aug 14, 2012 at 12:57 PM
subject: Proceedings Inquiry

Hi,

I am a PhD student at University of Waterloo, Canada. I would like to use my proceeding material as a part of my PhD Thesis.

Could you please let me know how to proceed to acquire an official permission?

My paper information is:

Sepideh Hariri, Patrick J. Lee, Alireza A. Moayed, and Kostadinka Bizheva,"In-vivo human retina imaging with 5µm axial resolution, at 92000 A-scans/s with 1µm spectral domain OCT system",Proc. SPIE 7889, 78890K (2011)

Thank you in advance for your kind attention.

Best regards

--
Sepideh Hariri
PhD Candidate

Department of Physics and Astronomy
University of Waterloo
200 University Ave West
Waterloo, Ontario Canada N2L 3G1
(519) 888 4567 ext. 35665
shariri@uwaterloo.ca

from: authorhelp <authorhelp@spie.org>
to: Sepideh Hariri <sepidhariri@gmail.com>
date: Wed, Aug 15, 2012 at 8:53 AM
subject: RE: Proceedings Inquiry

You retain the rights to your material. We only ask that the information is cited as part of the Proceedings of SPIE by using the proceedings reference as you indicate.

Regards,
Sandy

Ms. Sandy Hoelterhoff
Conference Programs Coordinator
Conference Programs and Proceedings
+1 360 685 5517 (office)
+1 360 647 1445 (fax)
SandyH@spie.org

SPIE is the international society for optics and photonics
http://SPIE.org
****

from: Sepideh Hariri <sepidhariri@gmail.com>
to: copyright@osa.org
date: Tue, Aug 14, 2012 at 12:46 PM
subject: permission for using paper content in PhD thesis

Hi,

I am a PhD student at University of Waterloo, Canada. I would like to use my paper material as a part of my PhD Thesis.

Could you please let me know how to proceed to acquire an official permission from your journal?

My paper information is:

Sepideh Hariri, Alireza A. Moayed, Aphrodite Dracopoulos, Chulho Hyun, Shelley Boyd and Kostadinka Bizheva ,"Limiting factors to the OCT axial resolution for in-vivo imaging of human and rodent retina in the 1060nm wavelength range" ,Optics Express, Vol. 17, Issue 26, pp. 24304-24316 (2009)

Thank you in advance for your kind attention.

Best regards

--

Sepideh Hariri

PhD Candidate

Department of Physics and Astronomy

University of Waterloo

200 University Ave West

Waterloo, Ontario Canada N2L 3G1

(519) 888 4567 ext. 35665

shariri@uwaterloo.ca

from: pubscopyright <copyright@osa.org>
to: Sepideh Hariri <sepidhariri@gmail.com>
date: Wed, Aug 15, 2012 at 7:06 AM
subject: RE: permission for using paper content in PhD thesis

Dear Sepideh,

Thank you for contacting The Optical Society.

Because you are the author of the source papers from which you wish to reproduce material, OSA considers your requested use of its copyrighted materials to be permissible within the author rights granted in the Copyright Transfer Agreement submitted by the requester on acceptance for publication of his/her manuscript. It is requested that a complete citation of the original material be included in any publication. This permission assumes that the material was not reproduced from another source when published in the original publication.

Please let me know if you have any questions.

Best,

Hannah

Hannah Bembia

August 15, 2012

Authorized Agent, The Optical Society

2. Co-author Permission

from: Sepideh Hariri <sepidhariri@gmail.com>
to: Dida Bizheva <kbizheva@uwaterloo.ca>,
Alireza Akhlagh Moayed <alimoayed@gmail.com>,
Denise Hileeto <denise.hileeto@uwaterloo.ca>,
Dave Lee <ldh0208@hotmail.com>,
mc2tam <mc2tam@uwaterloo.ca>
date: Thu, Jan 10, 2013 at 10:46 PM
subject: permission for reproduction of paper material

Dear co-authors,

Hi,

I would like to ask your permission for using the material from the following publication, in which you are co-authors, in my PhD thesis:

S. Hariri, Man Chun Tam, Donghyun Lee, Denise Hileeto, A. A. Moayed, and K. Bizheva, "Non-invasive imaging of the early effect of sodium iodate toxicity in a rat model of outer retina degeneration with SD-OCT", JBO, accepted 2 Jan 2013.

I sincerely appreciate your kind attention to this matter.

Best regards

--

Sepideh Hariri

PhD Candidate

Department of Physics and Astronomy
University of Waterloo
200 University Ave West
Waterloo, Ontario Canada N2L 3G1
(519) 888 4567 ext. 35665
shariri@sciborg.uwaterloo.ca

from: mc2tam@uwaterloo.ca

to: Sepideh Hariri <sepidhariri@gmail.com>
date: Fri, Jan 11, 2013 at 12:03 AM
subject: Re: permission for reproduction of paper material

Hi Sepideh,

Sure!

Alan

from: Alireza A.Moayed <alimoayed@gmail.com>
to: Sepideh Hariri <sepidhariri@gmail.com>
date: Fri, Jan 11, 2013 at 12:25 AM
subject: Re: permission for reproduction of paper material

Dear Dr.Hariri

Hi

Permission granted.

Wish you the best.

Alireza A.Moayed

Alireza A.Moayed, *PhD*

Postdoctoral Researcher

Department of Bioengineering

University of Washington

Seattle, Washington, USA 98195

alimoayed@gmail.com

from: Dida <kbizheva@uwaterloo.ca>
to: Sepideh Hariri <sepidhariri@gmail.com>
date: Fri, Jan 11, 2013 at 4:43 AM
subject: Re: permission for reproduction of paper material

Hello Sepideh,

You have my permission to use the material from the publication in your thesis.

Best regards,

Dida

Dr. Kostadinka Bizheva
Associate Professor
Department of Physics and Astronomy
University of Waterloo
200 University Ave West
Waterloo, ON N2L 3G1
Canada
Phone: (519) 888 4567 x 37517 (office), x35665 (old lab), x31133 (new lab)
Cell Phone: 519 572 1774
E-mail: kbizheva@uwaterloo.ca

from: Denise Hileeto <denise.hileeto@uwaterloo.ca>
to: Sepideh Hariri <sepidhariri@gmail.com>
date: Fri, Jan 11, 2013 at 6:38 AM
subject: RE: permission for reproduction of paper material
to me

Hi Sepideh,

Sure you can use anything you need to!

Good luck!

Denise

****

from: Sepideh Hariri <sepidhariri@gmail.com>
to: Dida Bizheva <kbizheva@uwaterloo.ca>
date: Sun, Sep 16, 2012 at 10:08 AM
subject: permission for reproduction of paper material

Dear Proff. Kostadinka Bizheva,

I would like to ask your permission for using the material from the following publications, in which you are the senior co-author, in my PhD thesis:

S. Hariri, A. A. Moayed, A. Dracopoulos, C. Hyun, S. Boyd, and K. Bizheva, "Limiting factors to the OCT axial resolution for in-vivo imaging of human and rodent retina in the 1060 nm wavelength range," *Opt Express*, vol. 17, no. 26, pp. 24304–24316, Dec. 2009.
S. Hariri, A. A. Moayed, V. Choh, and K. Bizheva, "In vivo assessment of thickness and reflectivity in a rat outer retinal degeneration model with ultrahigh resolution optical coherence tomography," *Invest. Ophthalmol. Vis. Sci.*, vol. 53, no. 4, pp. 1982–1989, Apr. 2012.

S. Hariri, P. J. Lee, A. A. Moayed, and K. Bizheva, "In-vivo human retina imaging with 5μm axial resolution, at 92000 A-scans/s with 1μm spectral domain OCT system," Proceedings of SPIE, vol. 7889, no. 1, p. 78890K–78890K–5, Feb. 2011.

I sincerely appreciate your kind attention to this matter.
Best regards
--
Sepideh Hariri
PhD Candidate

Department of Physics and Astronomy
University of Waterloo
200 University Ave West
Waterloo, Ontario Canada N2L 3G1
(519) 888 4567 ext. 35665
shariri@sciborg.uwaterloo.ca

from: Dida <kbizheva@uwaterloo.ca>
to: Sepideh Hariri <sepidhariri@gmail.com>
date: Sun, Sep 16, 2012 at 10:19 AM
subject: Re: permission for reproduction of paper material

Hi Sepideh,

You have my permission to reproduce the information from the publications listed below in your PhD thesis.

Best regards,

Dida

--
Dr. Kostadinka Bizheva

Associate Professor
Department of Physics and Astronomy
University of Waterloo
200 University Ave West
Waterloo, ON N2L 3G1
Canada
Phone: (519) 888 4567 x 37517 (office), x35665 (old lab), x31133 (new lab)
Cell Phone: 519 572 1774
E-mail: kbizheva@uwaterloo.ca

****

from: Sepideh Hariri <sepidhariri@gmail.com>
to: Vivian <vchoh@uwaterloo.ca>
cc: Dida Bizheva <kbizheva@uwaterloo.ca>
date: Sun, Sep 16, 2012 at 9:42 AM
subject: permission for reproduction of paper material

Dear Dr. Vivian Choh,

I would like to ask your permission for using the material from the following publication, in which you are one of the co-authors, in my PhD thesis:

S. Hariri, A. A. Moayed, V. Choh, and K. Bizheva, “In vivo assessment of thickness and reflectivity in a rat outer retinal degeneration model with ultrahigh resolution optical coherence tomography,” *Invest. Ophthalmol. Vis. Sci.*, vol. 53, no. 4, pp. 1982–1989, Apr. 2012.

I sincerely appreciate your kind attention to this matter.
Best regards
--
Sepideh Hariri
PhD Candidate

Department of Physics and Astronomy
University of Waterloo
200 University Ave West
Waterloo, Ontario Canada N2L 3G1
(519) 888 4567 ext. 35665
shariri@sciborg.uwaterloo.ca

from: Vivian Choh <vchoh@uwaterloo.ca>
to: Sepideh Hariri <sepidhariri@gmail.com>
date: Sun, Sep 16, 2012 at 2:22 PM
subject: Re: permission for reproduction of paper material

Dear Sepideh,

You have my permission

Viv
Associate Professor
Room 260, School of Optometry
University of Waterloo
Tel: 1 (519) 888-4567 x35005
email: vchoh@uwaterloo.ca

****

from: Sepideh Hariri <sepidhariri@gmail.com>
to: Shelley Boyd <boyds@smh.toronto.on.ca>,
Shelley Boyd <Boyds@smh.ca>
cc: Dida Bizheva <kbizheva@uwaterloo.ca>
date: Sun, Sep 16, 2012 at 9:22 AM
subject: permission for reproduction of paper material

Dear Dr. Shelley Boyd,
I would like to ask your permission for using the material of the following publication ,in which you are one of the co-authors, in my PhD thesis:

S. Hariri, A. A. Moayed, A. Dracopoulos, C. Hyun, S. Boyd, and K. Bizheva, “Limiting factors to the OCT axial resolution for in-vivo imaging of human and rodent retina in the 1060 nm wavelength range,” *Opt Express*, vol. 17, no. 26, pp. 24304–24316, Dec. 2009.

I sincerely appreciate your kind attention to this matter.
Best regards
--
Sepideh Hariri
PhD Candidate

Department of Physics and Astronomy
University of Waterloo
200 University Ave West

Waterloo, Ontario Canada N2L 3G1
(519) 888 4567 ext. 35665
shariri@sciborg.uwaterloo.ca

-------- Original Message --------
Subject:permission to reproduce images
Date: Thu, 25 Oct 2012 18:37:17 +0000
From: Shelley Boyd <Boyds@smh.ca>
To: 'kbizheva@uwaterloo.ca' <kbizheva@uwaterloo.ca>

Hi Dida,

good speaking, albeit briefly, yesterday.

Please give my congratulations to Sepideh and Ali for their successful PhD defenses!

This email officially confirms that both Sepideh Haririr and Alireza Moayod have permission to reproduce images and text from our publications in their theses.

If you require any additional documentation, please let me know.

Best wishes,

Shelley

****

from: Sepideh Hariri <sepidhariri@gmail.com>
to: darylhyun@gmail.com
cc: Dida Bizheva <kbizheva@uwaterloo.ca>
date: Sun, Sep 16, 2012 at 9:30 AM
subject: permission for reproduction of paper material

Dear Mr. Daryl Hyun,

I would like to ask your permission for using the material of the following publication ,in which you are one of the co-authors, in my PhD thesis:

S. Hariri, A. A. Moayed, A. Dracopoulos, C. Hyun, S. Boyd, and K. Bizheva, “Limiting factors to the OCT axial resolution for in-vivo imaging of human and rodent retina in the 1060 nm wavelength range,” *Opt Express,* vol. 17, no. 26, pp. 24304–24316, Dec. 2009.

I sincerely appreciate your kind attention to this matter.
Best regards

--
Sepideh Hariri
PhD Candidate

Department of Physics and Astronomy
University of Waterloo
200 University Ave West
Waterloo, Ontario Canada N2L 3G1
(519) 888 4567 ext. 35665
shariri@sciborg.uwaterloo.ca

from: Daryl Chulho Hyun <darylhyun@gmail.com>
to: Sepideh Hariri <sepidhariri@gmail.com>
date: Sun, Sep 16, 2012 at 8:54 PM
subject: Re: permission for reproduction of paper material

Hi Sepideh,

Yes. Of course you can use the material. And, congratulations to you and Ali for PhD defense. I talked to Dida when I visited, and heard you guys are going to Seattle. Let's keep in touch.

Best wishes to you, Ali and your future,
daryl

--
Daryl Chulho Hyun
BSc in Honours Physics, Co-op, Applied Physics Specialization
Research Assistant II, Imaging Unit, Integrative Oncology Department
BC Cancer Research Centre, BC Cancer Agency
Cell Phone: 1 778 873 0469
E-mail: darylhyun@gmail.com or dhyun@bccrc.ca

****

from: Sepideh Hariri <sepidhariri@gmail.com>
to: Patrick Lee <patricklee235@gmail.com>
cc: Dida Bizheva <kbizheva@uwaterloo.ca>
date: Sun, Sep 16, 2012 at 9:38 AM
subject: permission for reproduction of paper material

Dear Mr. Patrick Lee,

I would like to ask your permission for using the material from the following publication, in which you are one of the co-authors, in my PhD thesis:

S. Hariri, P. J. Lee, A. A. Moayed, and K. Bizheva, "In-vivo human retina imaging with 5μm axial resolution, at 92000 A-scans/s with 1μm spectral domain OCT system," Proceedings of SPIE, vol. 7889, no. 1, p. 78890K–78890K–5, Feb. 2011.

I sincerely appreciate your kind attention to this matter.
Best regards
--
Sepideh Hariri
PhD Candidate

Department of Physics and Astronomy
University of Waterloo
200 University Ave West
Waterloo, Ontario Canada N2L 3G1
(519) 888 4567 ext. 35665
shariri@sciborg.uwaterloo.ca

****

from: Sepideh Hariri <sepidhariri@gmail.com>
to: aphrodite.dracopoulos@gmail.com
date: Sun, Sep 16, 2012 at 2:16 PM
subject: permission for reproduction of paper material
Dear Mrs. Aphrodite Dracopoulos,

I would like to ask your permission for using the material from the following publication, in which you are a co-author, in my PhD thesis:

S. Hariri, A. A. Moayed, A. Dracopoulos, C. Hyun, S. Boyd, and K. Bizheva, "Limiting factors to the OCT axial resolution for in-vivo imaging of human and rodent retina in the 1060 nm wavelength range," *Opt Express*, vol. 17, no. 26, pp. 24304–24316, Dec. 2009.

I sincerely appreciate your kind attention to this matter.
Best regards
--
Sepideh Hariri
PhD Candidate

Department of Physics and Astronomy
University of Waterloo
200 University Ave West
Waterloo, Ontario Canada N2L 3G1
(519) 888 4567 ext. 35665
shariri@sciborg.uwaterloo.ca

from:	Aphrodite Dracopoulos-Stavropoulos <aphrodite.dracopoulos@gmail.com>
to:	Sepideh Hariri <sepidhariri@gmail.com>
date:	Sun, Sep 16, 2012 at 3:18 PM
subject:	Re: permission for reproduction of paper material

Dear Mrs. Hariri,
I, Aphrodite Dracopoulos, grant you permission to use the material from the following publication, in which I was co-author, in your PhD thesis:
S. Hariri, A. A. Moayed, A. Dracopoulos, C. Hyun, S. Boyd, and K. Bizheva, “Limiting factors to the OCT axial resolution for in-vivo imaging of human and rodent retina in the 1060 nm wavelength range,” *Opt Express*, vol. 17, no. 26, pp. 24304–24316, Dec. 2009.

Thank you,
Aphrodite Dracopoulos
--
Aphrodite (Dracopoulos) Stavropoulos, MSc, HBSc/BA
PhD Candidate
Glaucoma Research Group
Flanagan Lab, Toronto Western Hospital
Collaborative Program in Biomedical Toxicology
Institute of Medical Science, University of Toronto
(416) 603-5800 Office (x2365)
Cell (416) 209-1042
Fax (416) 603-5126

Bibliography

[1] W. Drexler and J. G. Fujimoto, Eds., *Optical Coherence Tomography: Technology and Applications*, 2008th ed. Springer, 2008.

[2] J. G. Fujimoto, S. De Silvestri, E. P. Ippen, C. A. Puliafito, R. Margolis, and A. Oseroff, “Femtosecond optical ranging in biological systems,” *Opt. Lett.*, vol. 11, no. 3, pp. 150–152, Mar. 1986.

[3] R. C. Youngquist, S. Carr, and D. E. N. Davies, “Optical coherence-domain reflectometry: a new optical evaluation technique,” *Opt. Lett.*, vol. 12, no. 3, pp. 158–160, Mar. 1987.

[4] A. F. Fercher, K. Mengedoht, and W. Werner, “Eye-length measurement by interferometry with partially coherent light,” *Opt. Lett.*, vol. 13, no. 3, pp. 186–188, Mar. 1988.

[5] E. A. Swanson, D. Huang, M. R. Hee, J. G. Fujimoto, C. P. Lin, and C. A. Puliafito, “High-speed optical coherence domain reflectometry,” *Opt. Lett.*, vol. 17, no. 2, pp. 151–153, Jan. 1992.

[6] B. Bouma, Ed., *Handbook of Optical Coherence Tomography*, 1st ed. Informa Healthcare, 2001.

[7] B. Sander, U. Christensen, M. Larsen, and T. M. Jørgensen, “Quantification of the Outer Retinal Layers: Correlation to Visual Acuity in Healthy Subjects and Patients with Central Serous Chorioretinopathy,” in *Optical Coherence Tomography and Coherence Techniques III*, 2007, vol. 6627, p. 6627_46.

[8] D. Huang, E. A. Swanson, C. P. Lin, J. S. Schuman, W. G. Stinson, W. Chang, M. R. Hee, T. Flotte, K. Gregory, C. A. Puliafito, and A. Et, “Optical coherence tomography,” *Science*, vol. 254, no. 5035, pp. 1178–1181, Nov. 1991.

[9] R. Leitgeb, C. Hitzenberger, and A. Fercher, “Performance of fourier domain vs. time domain optical coherence tomography,” *Opt. Express*, vol. 11, no. 8, pp. 889–894, Apr. 2003.

[10] M. Choma, M. Sarunic, C. Yang, and J. Izatt, “Sensitivity advantage of swept source and Fourier domain optical coherence tomography,” *Opt. Express*, vol. 11, no. 18, pp. 2183–2189, 2003.

[11] J. F. de Boer, B. Cense, B. H. Park, M. C. Pierce, G. J. Tearney, and B. E. Bouma, “Improved signal-to-noise ratio in spectral-domain compared with time-domain optical coherence tomography,” *Opt. Lett.*, vol. 28, no. 21, pp. 2067–2069, Nov. 2003.

[12] M. Wojtkowski, A. Kowalczyk, R. Leitgeb, and A. F. Fercher, “Full range complex spectral optical coherence tomography technique in eye imaging,” *Opt. Lett.*, vol. 27, no. 16, pp. 1415–1417, 2002.

[13] R. A. Leitgeb, C. K. Hitzenberger, A. F. Fercher, and T. Bajraszewski, “Phase-shifting algorithm to achieve high-speed long-depth-range probing by frequency-domain optical coherence tomography,” *Opt. Lett.*, vol. 28, no. 22, pp. 2201–2203, Nov. 2003.

[14] S. Yun, G. Tearney, J. de Boer, and B. Bouma, “Removing the depth-degeneracy in optical frequency domain imaging with frequency shifting,” *Opt. Express*, vol. 12, no. 20, pp. 4822–4828, Oct. 2004.

[15] M. Sarunic, M. A. Choma, C. Yang, and J. A. Izatt, “Instantaneous complex conjugate resolved spectral domain and swept-source OCT using 3x3 fiber couplers,” *Opt. Express*, vol. 13, no. 3, pp. 957–967, Feb. 2005.

[16] M. Wojtkowski, V. J. Srinivasan, T. H. Ko, J. G. Fujimoto, A. Kowalczyk, and J. S. Duker, “Ultrahigh-resolution, high-speed, Fourier domain optical coherence tomography and methods for dispersion compensation,” *Optics Express*, vol. 12, no. 11, p. 2404, 2004.

[17] S. R. Chinn, E. A. Swanson, and J. G. Fujimoto, “Optical coherence tomography using a frequency-tunable optical source,” *Opt. Lett.*, vol. 22, no. 5, pp. 340–342, Mar. 1997.

[18] L. An, P. Li, T. T. Shen, and R. Wang, “High speed spectral domain optical coherence tomography for retinal imaging at 500,000 A‐ lines per second,” *Biomedical Optics Express*, vol. 2, no. 10, p. 2770, Sep. 2011.

[19] W. Choi, B. Baumann, J. J. Liu, A. C. Clermont, E. P. Feener, J. S. Duker, and J. G. Fujimoto, “Measurement of pulsatile total blood flow in the human and rat retina with ultrahigh speed spectral/Fourier domain OCT,” *Biomedical Optics Express*, vol. 3, no. 5, p. 1047, Apr. 2012.

[20] B. Potsaid, I. Gorczynska, V. J. Srinivasan, Y. Chen, J. Jiang, A. Cable, and J. G. Fujimoto, “Ultrahigh speed Spectral / Fourierdomain OCT ophthalmic imaging at70,000 to 312,500 axial scans per second,” *Opt. Express*, vol. 16, no. 19, pp. 15149–15169, 2008.

[21] S. Hariri, P. J. Lee, A. A. Moayed, and K. Bizheva, “In-vivo human retina imaging with 5μm axial resolution, at 92000 A-scans/s with 1μm spectral domain OCT system,” *Proceedings of SPIE*, vol. 7889, no. 1, p. 78890K–78890K–5, Feb. 2011.

[22] K. Bizheva, N. Hutchings, L. Sorbara, A. A. Moayed, and T. Simpson, “In vivo volumetric imaging of the human corneo-scleral limbus with spectral domain OCT,” *Biomedical Optics Express*, vol. 2, no. 7, p. 1794, Jun. 2011.

[23] R. K. Wang and L. An, “Multifunctional imaging of human retina and choroid with 1050-nm spectral domain optical coherence tomography at 92-kHz line scan rate,” *J Biomed Opt*, vol. 16, no. 5, p. 050503, May 2011.

[24] B. Grajciar, Y. Lehareinger, A. F. Fercher, and R. A. Leitgeb, “High sensitivity phase mapping with parallel Fourier domain optical coherence tomography at 512 000 A-scan/s,” *Opt. Express*, vol. 18, no. 21, pp. 21841–21850, Oct. 2010.

[25] V. J. Srinivasan, D. C. Adler, Y. Chen, I. Gorczynska, R. Huber, J. S. Duker, J. S. Schuman, and J. G. Fujimoto, “Ultrahigh-Speed Optical Coherence Tomography for Three-Dimensional and En Face Imaging of the Retina and Optic Nerve Head,” *Invest Ophthalmol Vis Sci*, vol. 49, no. 11, pp. 5103–5110, Nov. 2008.

[26] B. Potsaid, B. Baumann, D. Huang, S. Barry, A. E. Cable, J. S. Schuman, J. S. Duker, and J. G. Fujimoto, “Ultrahigh speed 1050nm swept source / Fourier domain OCT retinal and anterior segment imaging at 100,000 to 400,000 axial scans per second,” *Opt Express*, vol. 18, no. 19, pp. 20029–20048, Sep. 2010.

[27] T. Klein, W. Wieser, C. M. Eigenwillig, B. R. Biedermann, and R. Huber, “Megahertz OCT for ultrawide-field retinal imaging with a 1050nm Fourier domain mode-locked laser,” *Optics Express*, vol. 19, no. 4, p. 3044, Feb. 2011.

[28] W. Drexler, U. Morgner, F. X. Kärtner, C. Pitris, S. A. Boppart, X. D. Li, E. P. Ippen, and J. G. Fujimoto, “In vivo ultrahigh-resolution optical coherence tomography,” *Opt. Lett.*, vol. 24, no. 17, pp. 1221–1223, 1999.

[29] B. Cense, N. A. Nassif, T. C. Chen, M. C. Pierce, S.-H. Yun, B. H. Park, B. E. Bouma, G. J. Tearney, and J. F. de Boer, “Ultrahigh-resolution high-speed retinal imaging using spectral-domain optical coherence tomography,” *Optics Express*, vol. 12, no. 11, p. 2435, 2004.

[30] A. Fercher, C. Hitzenberger, M. Sticker, R. Zawadzki, B. Karamata, and T. Lasser, “Numerical dispersion compensation for Partial Coherence Interferometry and Optical Coherence Tomography,” *Opt. Express*, vol. 9, no. 12, pp. 610–615, Dec. 2001.

[31] Y. Wang, J. Nelson, Z. Chen, B. Reiser, R. Chuck, and R. Windeler, “Optimal wavelength for ultrahigh-resolution optical coherence tomography,” *Opt. Express*, vol. 11, no. 12, pp. 1411–1417, Jun. 2003.

[32] C. K. Hitzenberger, “Optical measurement of the axial eye length by laser Doppler interferometry.,” *IOVS*, vol. 32, no. 3, pp. 616–624, Mar. 1991.

[33] E. A. Swanson, J. A. Izatt, M. R. Hee, D. Huang, C. P. Lin, J. S. Schuman, C. A. Puliafito, and J. G. Fujimoto, “In vivo retinal imaging by optical coherence tomography,” *Opt. Lett.*, vol. 18, no. 21, pp. 1864–1866, Nov. 1993.

[34] A. F. Fercher, C. K. Hitzenberger, W. Drexler, G. Kamp, and H. Sattmann, “In vivo optical coherence tomography,” *Am. J. Ophthalmol.*, vol. 116, no. 1, pp. 113–114, Jul. 1993.

[35] W. Drexler, “Ultrahigh-resolution optical coherence tomography,” *Journal of Biomedical Optics*, vol. 9, p. 47, 2004.

[36] W. Drexler, U. Morgner, R. K. Ghanta, F. X. Kartner, J. S. Schuman, and J. G. Fujimoto, “Ultrahigh-resolution ophthalmic optical coherence tomography,” *Nature medicine*, vol. 7, no. 4, pp. 502–506, 2001.

[37] W. Drexler, H. Sattmann, B. Hermann, T. H. Ko, M. Stur, A. Unterhuber, C. Scholda, O. Findl, M. Wirtitsch, J. G. Fujimoto, and A. F. Fercher, “Enhanced visualization of macular pathology with the use of ultrahigh-resolution optical coherence tomography,” *Arch. Ophthalmol.*, vol. 121, no. 5, pp. 695–706, May 2003.

[38] J. G. F. Wolfgang Drexler, “State-of-the-art retinal optical coherence tomography.,” *Progress in retinal and eye research*, vol. 27, no. 1, pp. 45–88, 2008.

[39] M. L. Gabriele, G. Wollstein, H. Ishikawa, L. Kagemann, J. Xu, L. S. Folio, and J. S. Schuman, “Optical coherence tomography: history, current status, and laboratory work,” *Invest. Ophthalmol. Vis. Sci.*, vol. 52, no. 5, pp. 2425–2436, Apr. 2011.

[40] M. Figurska, J. Robaszkiewicz, and J. Wierzbowska, “Optical coherence tomography in imaging of macular diseases,” *Klin Oczna*, vol. 112, no. 4–6, pp. 138–146, 2010.

[41] C. Scholda, M. Wirtitsch, B. Hermann, A. Unterhuber, E. Ergun, H. Sattmann, T. H. Ko, J. G. Fujimoto, A. F. Fercher, M. Stur, U. Schmidt-Erfurth, and W. Drexler, “Ultrahigh resolution optical coherence tomography of macular holes,” *Retina (Philadelphia, Pa.)*, vol. 26, no. 9, pp. 1034–1041, Dec. 2006.

[42] H. Fujimoto, F. Gomi, T. Wakabayashi, M. Sawa, M. Tsujikawa, and Y. Tano, “Morphologic changes in acute central serous chorioretinopathy evaluated by fourier-domain optical coherence tomography,” *Ophthalmology*, vol. 115, no. 9, pp. 1494–1500, 1500.e1–2, Sep. 2008.

[43] Y. Chen, L. N. Vuong, J. Liu, J. Ho, V. J. Srinivasan, I. Gorczynska, A. J. Witkin, J. S. Duker, J. Schuman, and J. G. Fujimoto, “Three-dimensional ultrahigh resolution optical coherence tomography imaging of age-related macular degeneration,” *Opt Express*, vol. 17, no. 5, pp. 4046–4060, Mar. 2009.

[44] G. Wollstein, L. A. Paunescu, T. H. Ko, J. G. Fujimoto, A. Kowalevicz, I. Hartl, S. Beaton, H. Ishikawa, C. Mattox, O. Singh, J. Duker, W. Drexler, and J. S. Schuman, “Ultrahigh-Resolution

Optical Coherence Tomography in Glaucoma," *Ophthalmology*, vol. 112, no. 2, pp. 229–237, Feb. 2005.

[45] H. W. van Dijk, F. D. Verbraak, P. H. B. Kok, M. Stehouwer, M. K. Garvin, M. Sonka, J. H. DeVries, R. O. Schlingemann, and M. D. Abràmoff, "Early neurodegeneration in the retina of type 2 diabetic patients," *Invest. Ophthalmol. Vis. Sci.*, vol. 53, no. 6, pp. 2715–2719, May 2012.

[46] C. V. Regatieri, L. Branchini, J. Carmody, J. G. Fujimoto, and J. S. Duker, "Choroidal thickness in patients with diabetic retinopathy analyzed by spectral-domain optical coherence tomography," *Retina (Philadelphia, Pa.)*, vol. 32, no. 3, pp. 563–568, Mar. 2012.

[47] M. G. Wirtitsch, E. Ergun, B. Hermann, A. Unterhuber, M. Stur, C. Scholda, H. Sattmann, T. H. Ko, J. G. Fujimoto, and W. Drexler, "Ultrahigh resolution optical coherence tomography in macular dystrophy," *Am. J. Ophthalmol.*, vol. 140, no. 6, pp. 976–983, Dec. 2005.

[48] E. Ergun, B. Hermann, M. Wirtitsch, A. Unterhuber, T. H. Ko, H. Sattmann, C. Scholda, J. G. Fujimoto, M. Stur, and W. Drexler, "Assessment of Central Visual Function in Stargardt's Disease/Fundus Flavimaculatus with Ultrahigh-Resolution Optical Coherence Tomography," *IOVS*, vol. 46, no. 1, pp. 310–316, Jan. 2005.

[49] T. H. Ko, A. J. Witkin, J. G. Fujimoto, A. Chan, A. H. Rogers, C. R. Baumal, J. S. Schuman, W. Drexler, E. Reichel, and J. S. Duker, "Ultrahigh-resolution optical coherence tomography of surgically closed macular holes," *Arch. Ophthalmol.*, vol. 124, no. 6, pp. 827–836, Jun. 2006.

[50] V. J. Srinivasan, T. H. Ko, M. Wojtkowski, M. Carvalho, A. Clermont, S.-E. Bursell, Q. H. Song, J. Lem, J. S. Duker, J. S. Schuman, and J. G. Fujimoto, "Noninvasive volumetric imaging and morphometry of the rodent retina with high-speed, ultrahigh-resolution optical coherence tomography," *Invest. Ophthalmol. Vis. Sci.*, vol. 47, no. 12, pp. 5522–5528, Dec. 2006.

[51] P. Puvanathasan, P. Forbes, Z. Ren, D. Malchow, S. Boyd, and K. Bizheva, "High-speed, high-resolution Fourier-domain optical coherence tomography system for retinal imaging in the 1060 nm wavelength region," *Opt Lett*, vol. 33, no. 21, pp. 2479–2481, Nov. 2008.

[52] G. Huber, S. Heynen, C. Imsand, F. vom Hagen, R. Muehlfriedel, N. Tanimoto, Y. Feng, H.-P. Hammes, C. Grimm, L. Peichl, M. W. Seeliger, and S. C. Beck, "Novel Rodent Models for Macular Research," *PLoS ONE*, vol. 5, no. 10, p. e13403, Oct. 2010.

[53] M. D. Fischer, G. Huber, S. C. Beck, N. Tanimoto, R. Muehlfriedel, E. Fahl, C. Grimm, A. Wenzel, C. E. Remé, S. A. van de Pavert, J. Wijnholds, M. Pacal, R. Bremner, and M. W. Seeliger, "Noninvasive, in vivo assessment of mouse retinal structure using optical coherence tomography," *PLoS ONE*, vol. 4, no. 10, p. e7507, 2009.

[54] G. Huber, S. C. Beck, C. Grimm, A. Sahaboglu-Tekgoz, F. Paquet-Durand, A. Wenzel, P. Humphries, T. M. Redmond, M. W. Seeliger, and M. D. Fischer, “Spectral domain optical coherence tomography in mouse models of retinal degeneration,” *Invest. Ophthalmol. Vis. Sci.*, vol. 50, no. 12, pp. 5888–5895, Dec. 2009.

[55] M. V. Sarunic, A. Yazdanpanah, E. Gibson, J. Xu, Y. Bai, S. Lee, H. U. Saragovi, and M. F. Beg, “Longitudinal study of retinal degeneration in a rat using spectral domain optical coherence tomography,” *Opt Express*, vol. 18, no. 22, pp. 23435–23441, Oct. 2010.

[56] B. Povazay, B. Hofer, C. Torti, B. Hermann, A. R. Tumlinson, M. Esmaeelpour, C. A. Egan, A. C. Bird, and W. Drexler, “Impact of enhanced resolution, speed and penetration on three-dimensional retinal optical coherence tomography,” *Opt. Express*, vol. 17, no. 5, pp. 4134–4150, Mar. 2009.

[57] J. Thaung and J. Sjöstrand, “Integrated light scattering as a function of wavelength in donor lenses,” *J Opt Soc Am A Opt Image Sci Vis*, vol. 19, no. 1, pp. 152–157, Jan. 2002.

[58] W. M. Irvine and J. B. Pollack, “Infrared optical properties of water and ice spheres,” *Icarus*, vol. 8, no. 1–3, pp. 324–360, Jan. 1968.

[59] G. M. Hale and M. R. Querry, “Optical Constants of Water in the 200-nm to 200-μm Wavelength Region,” *Appl. Opt.*, vol. 12, no. 3, pp. 555–563, Mar. 1973.

[60] A. N. S. Institute, “Safe use of lasers,ANSI Z136.1–2000.” American National Standards Institute, 2007.

[61] G. Lutty, J. Grunwald, A. B. Majji, M. Uyama, and S. Yoneya, “Changes in choriocapillaris and retinal pigment epithelium in age-related macular degeneration,” *Mol. Vis.*, vol. 5, p. 35, Nov. 1999.

[62] B. Povazay, B. Hermann, A. Unterhuber, B. Hofer, H. Sattmann, F. Zeiler, J. E. Morgan, C. Falkner-Radler, C. Glittenberg, S. Blinder, and W. Drexler, “Three-dimensional optical coherence tomography at 1050 nm versus 800 nm in retinal pathologies: enhanced performance and choroidal penetration in cataract patients,” *J Biomed Opt*, vol. 12, no. 4, p. 041211, Aug. 2007.

[63] K. Bizheva, R. Pflug, B. Hermann, B. Povazay, H. Sattmann, P. Qiu, E. Anger, H. Reitsamer, S. Popov, J. R. Taylor, A. Unterhuber, P. Ahnelt, and W. Drexler, “Optophysiology: depth-resolved probing of retinal physiology with functional ultrahigh-resolution optical coherence tomography,” *Proc. Natl. Acad. Sci. U.S.A.*, vol. 103, no. 13, pp. 5066–5071, Mar. 2006.

[64] A. Akhlagh Moayed, S. Hariri, V. Choh, and K. Bizheva, “Correlation of visually evoked intrinsic optical signals and electroretinograms recorded from chicken retina with a combined

functional optical coherence tomography and electroretinography system," *J Biomed Opt*, vol. 17, no. 1, p. 016011, Jan. 2012.

[65] A. A. Moayed, S. Hariri, V. Choh, and K. Bizheva, "In vivo imaging of intrinsic optical signals in chicken retina with functional optical coherence tomography," *Opt. Lett.*, vol. 36, no. 23, pp. 4575–4577, Dec. 2011.

[66] B. Masters, "Three-dimensional confocal microscopy of the human optic nerve in vivo," *Opt. Express*, vol. 3, no. 10, pp. 356–359, Nov. 1998.

[67] A. Roorda, "Applications of adaptive optics scanning laser ophthalmoscopy," *Optometry and vision science: official publication of the American Academy of Optometry*, vol. 87, no. 4, p. 260, 2010.

[68] D. T. Miller, O. P. Kocaoglu, Q. Wang, and S. Lee, "Adaptive optics and the eye (super resolution OCT)," *Eye (Lond)*, vol. 25, no. 3, pp. 321–330, Mar. 2011.

[69] R. J. Zawadzki, S. M. Jones, S. Pilli, S. Balderas-Mata, D. Y. Kim, S. S. Olivier, and J. S. Werner, "Integrated adaptive optics optical coherence tomography and adaptive optics scanning laser ophthalmoscope system for simultaneous cellular resolution in vivo retinal imaging," *Biomed. Opt. Express*, vol. 2, no. 6, pp. 1674–1686, Jun. 2011.

[70] Y. Zhang and A. Roorda, "Evaluating the lateral resolution of the adaptive optics scanning laser ophthalmoscope," *J Biomed Opt*, vol. 11, no. 1, p. 014002, Feb. 2006.

[71] R. J. Zawadzki, S. S. Choi, A. R. Fuller, J. W. Evans, B. Hamann, and J. S. Werner, "Cellular resolution volumetric in vivo retinal imaging with adaptive optics–optical coherence tomography," *Optics Express*, vol. 17, no. 5, p. 4084, Mar. 2009.

[72] A. G. Podoleanu and R. B. Rosen, "Combinations of techniques in imaging the retina with high resolution," *Prog Retin Eye Res*, vol. 27, no. 4, pp. 464–499, Jul. 2008.

[73] S. Schmitz-Valckenberg, F. G. Holz, A. C. Bird, and R. F. Spaide, "Fundus autofluorescence imaging: review and perspectives," *Retina (Philadelphia, Pa.)*, vol. 28, no. 3, pp. 385–409, Mar. 2008.

[74] R. C. Eagle Jr, A. C. Lucier, V. B. Bernardino Jr, and M. Yanoff, "Retinal pigment epithelial abnormalities in fundus flavimaculatus: a light and electron microscopic study," *Ophthalmology*, vol. 87, no. 12, pp. 1189–1200, Dec. 1980.

[75] J. J. Weiter, F. C. Delori, G. L. Wing, and K. A. Fitch, "Retinal pigment epithelial lipofuscin and melanin and choroidal melanin in human eyes," *Invest. Ophthalmol. Vis. Sci.*, vol. 27, no. 2, pp. 145–152, Feb. 1986.

[76] A. von Rückmann, F. W. Fitzke, and A. C. Bird, “Distribution of fundus autofluorescence with a scanning laser ophthalmoscope,” *Br J Ophthalmol*, vol. 79, no. 5, pp. 407–412, May 1995.

[77] J. J. Jorzik, A. Bindewald, S. Dithmar, and F. G. Holz, “Digital simultaneous fluorescein and indocyanine green angiography, autofluorescence, and red-free imaging with a solid-state laser-based confocal scanning laser ophthalmoscope,” *Retina (Philadelphia, Pa.)*, vol. 25, no. 4, pp. 405–416, Jun. 2005.

[78] L. A. Yannuzzi, “Indocyanine green angiography: a perspective on use in the clinical setting,” *Am. J. Ophthalmol.*, vol. 151, no. 5, pp. 745–751.e1, May 2011.

[79] J. J. Wang, E. Rochtchina, A. J. Lee, E.-M. Chia, W. Smith, R. G. Cumming, and P. Mitchell, “Ten-year incidence and progression of age-related maculopathy: the blue Mountains Eye Study,” *Ophthalmology*, vol. 114, no. 1, pp. 92–98, Jan. 2007.

[80] M. L. Klein, F. L. Ferris III, J. Armstrong, T. S. Hwang, E. Y. Chew, S. B. Bressler, and S. R. Chandra, “Retinal Precursors and the Development of Geographic Atrophy in Age-Related Macular Degeneration,” *Ophthalmology*, vol. 115, no. 6, pp. 1026–1031, Jun. 2008.

[81] U. E. K. Wolf-Schnurrbusch, V. Enzmann, C. K. Brinkmann, and S. Wolf, “Morphologic changes in patients with geographic atrophy assessed with a novel spectral OCT-SLO combination,” *Invest. Ophthalmol. Vis. Sci.*, vol. 49, no. 7, pp. 3095–3099, Jul. 2008.

[82] S. Schmitz-Valckenberg, M. Fleckenstein, A. P. Göbel, T. C. Hohman, and F. G. Holz, “Optical coherence tomography and autofluorescence findings in areas with geographic atrophy due to age-related macular degeneration,” *Invest. Ophthalmol. Vis. Sci.*, vol. 52, no. 1, pp. 1–6, Jan. 2011.

[83] A. P. Göbel, M. Fleckenstein, S. Schmitz-Valckenberg, C. K. Brinkmann, and F. G. Holz, “Imaging geographic atrophy in age-related macular degeneration,” *Ophthalmologica*, vol. 226, no. 4, pp. 182–190, 2011.

[84] S. A. Yaylali, A. A. Akcakaya, H. H. Erbil, B. Candemir, C. Mesci, and H. Acar, “The relationship between optical coherence tomography patterns, angiographic parameters and visual acuity in age-related macular degeneration,” *Int Ophthalmol*, vol. 32, no. 1, pp. 25–30, Feb. 2012.

[85] A. J. Witkin, L. N. Vuong, V. J. Srinivasan, I. Gorczynska, E. Reichel, C. R. Baumal, A. H. Rogers, J. S. Schuman, J. G. Fujimoto, and J. S. Duker, “High-speed ultrahigh resolution optical coherence tomography before and after ranibizumab for age-related macular degeneration,” *Ophthalmology*, vol. 116, no. 5, pp. 956–963, May 2009.

[86] P. K. Kaiser, D. S. Boyer, R. Garcia, Y. Hao, M. S. Hughes, N. M. Jabbour, P. K. Kaiser, W. Mieler, J. S. Slakter, M. Samuel, M. J. Tolentino, D. Roth, T. Sheidow, and H. A. Strong,

"Verteporfin photodynamic therapy combined with intravitreal bevacizumab for neovascular age-related macular degeneration," *Ophthalmology*, vol. 116, no. 4, pp. 747–755, 755.e1, Apr. 2009.

[87] A. H. Milam, Z. Y. Li, and R. N. Fariss, "Histopathology of the human retina in retinitis pigmentosa," *Prog Retin Eye Res*, vol. 17, no. 2, pp. 175–205, Apr. 1998.

[88] T. Wakabayashi, M. Sawa, F. Gomi, and M. Tsujikawa, "Correlation of fundus autofluorescence with photoreceptor morphology and functional changes in eyes with retinitis pigmentosa," *Acta Ophthalmol*, vol. 88, no. 5, pp. e177–183, Aug. 2010.

[89] Y. Wen, M. Klein, D. C. Hood, and D. G. Birch, "Relationships among multifocal electroretinogram amplitude, visual field sensitivity, and SD-OCT receptor layer thicknesses in patients with retinitis pigmentosa," *Invest. Ophthalmol. Vis. Sci.*, vol. 53, no. 2, pp. 833–840, 2012.

[90] P. Eversole-Cire, F. A. Concepcion, M. I. Simon, S. Takayama, J. C. Reed, and J. Chen, "Synergistic effect of Bcl-2 and BAG-1 on the prevention of photoreceptor cell death," *Invest. Ophthalmol. Vis. Sci.*, vol. 41, no. 7, pp. 1953–1961, Jun. 2000.

[91] Y. Murakami, Y. Ikeda, Y. Yonemitsu, M. Onimaru, K. Nakagawa, R. Kohno, M. Miyazaki, T. Hisatomi, M. Nakamura, T. Yabe, M. Hasegawa, T. Ishibashi, and K. Sueishi, "Inhibition of nuclear translocation of apoptosis-inducing factor is an essential mechanism of the neuroprotective activity of pigment epithelium-derived factor in a rat model of retinal degeneration," *Am. J. Pathol.*, vol. 173, no. 5, pp. 1326–1338, Nov. 2008.

[92] A. Wenzel, C. Grimm, M. Samardzija, and C. E. Remé, "Molecular mechanisms of light-induced photoreceptor apoptosis and neuroprotection for retinal degeneration," *Prog Retin Eye Res*, vol. 24, no. 2, pp. 275–306, Mar. 2005.

[93] D. T. Organisciak and D. K. Vaughan, "Retinal light damage: mechanisms and protection," *Prog Retin Eye Res*, vol. 29, no. 2, pp. 113–134, Mar. 2010.

[94] A. Boretsky, M. Motamedi, B. Bell, and F. van Kuijk, "Quantitative evaluation of retinal response to laser photocoagulation using dual-wavelength fundus autofluorescence imaging in a small animal model," *Invest. Ophthalmol. Vis. Sci.*, vol. 52, no. 9, pp. 6300–6307, Aug. 2011.

[95] T. Fukuchi, K. Takahashi, K. Shou, and M. Matsumura, "Optical coherence tomography (OCT) findings in normal retina and laser-induced choroidal neovascularization in rats," *Graefes Arch. Clin. Exp. Ophthalmol.*, vol. 239, no. 1, pp. 41–46, Jan. 2001.

[96] S. Fauser, J. Luberichs, and F. Schüttauf, "Genetic animal models for retinal degeneration," *Surv Ophthalmol*, vol. 47, no. 4, pp. 357–367, Aug. 2002.

[97] K. H. Kim, M. Puoris'haag, G. N. Maguluri, Y. Umino, K. Cusato, R. B. Barlow, and J. F. de Boer, "Monitoring mouse retinal degeneration with high-resolution spectral-domain optical coherence tomography," *J Vis*, vol. 8, no. 1, pp. 17.1–11, 2008.

[98] J. W. B. Bainbridge, M. H. Tan, and R. R. Ali, "Gene therapy progress and prospects: the eye," *Gene Therapy*, vol. 13, no. 16, pp. 1191–1197, 2006.

[99] A. Otani, M. I. Dorrell, K. Kinder, S. K. Moreno, S. Nusinowitz, E. Banin, J. Heckenlively, and M. Friedlander, "Rescue of retinal degeneration by intravitreally injected adult bone marrow–derived lineage-negative hematopoietic stem cells," *Journal of Clinical Investigation*, vol. 114, no. 6, pp. 765–774, Sep. 2004.

[100] G. Q. Chang, Y. Hao, and F. Wong, "Apoptosis: final common pathway of photoreceptor death in rd, rds, and rhodopsin mutant mice," *Neuron*, vol. 11, no. 4, pp. 595–605, Oct. 1993.

[101] J. M. Noel, J. P. Fernandez de Castro, P. J. Demarco Jr, L. M. Franco, W. Wang, E. V. Vukmanic, X. Peng, J. H. Sandell, P. A. Scott, H. J. Kaplan, and M. A. McCall, "Iodoacetic acid, but not sodium iodate, creates an inducible swine model of photoreceptor damage," *Exp. Eye Res.*, vol. 97, no. 1, pp. 137–147, Apr. 2012.

[102] Y. H. Yoon and M. F. Marmor, "Retinal pigment epithelium adhesion to Bruch's membrane is weakened by hemicholinium-3 and sodium iodate," *Ophthalmic Res.*, vol. 25, no. 6, pp. 386–392, 1993.

[103] C. H. Chon, X. Y. Yao, R. Dalal, A. Takeuchi, R. Y. Kim, and M. F. Marmor, "An experimental model of retinal pigment epithelial and neurosensory serous detachment," *Retina (Philadelphia, Pa.)*, vol. 16, no. 2, pp. 139–144, 1996.

[104] A. Tsubura, K. Yoshizawa, M. Kuwata, and N. Uehara, "Animal models for retinitis pigmentosa induced by MNU; disease progression, mechanisms and therapeutic trials," *Histol. Histopathol.*, vol. 25, no. 7, pp. 933–944, Jul. 2010.

[105] G. E. Korte, R. W. Bellhorn, and M. S. Burns, "Urethane-induced rat retinopathy. Plasticity of the blood-retinal barrier in disease.," *IOVS*, vol. 25, no. 9, pp. 1027–1034, Sep. 1984.

[106] K. Kiuchi, K. Yoshizawa, N. Shikata, K. Moriguchi, and A. Tsubura, "Morphologic characteristics of retinal degeneration induced by sodium iodate in mice," *Curr. Eye Res.*, vol. 25, no. 6, pp. 373–379, Dec. 2002.

[107] A. Machalińska, W. Lubiński, P. Kłos, M. Kawa, B. Baumert, K. Penkala, R. Grzegrzółka, D. Karczewicz, B. Wiszniewska, and B. Machaliński, "Sodium iodate selectively injuries the posterior

pole of the retina in a dose-dependent manner: morphological and electrophysiological study," *Neurochem. Res.*, vol. 35, no. 11, pp. 1819–1827, Nov. 2010.

[108] L. Mecklenburg and U. Schraermeyer, "An Overview on the Toxic Morphological Changes in the Retinal Pigment Epithelium After Systemic Compound Administration," *Toxicol Pathol*, vol. 35, no. 2, pp. 252–267, Feb. 2007.

[109] A. Sorsby, "EXPERIMENTAL PIGMENTARY DEGENERATION OF THE RETINA BY SODIUM IODATE," *Br J Ophthalmol*, vol. 25, no. 2, pp. 58–62, Feb. 1941.

[110] O. Textorius, E. Welinder, and S. E. Nilsson, "Combined effects of DL-alpha-aminoadipic acid with sodium iodate, ethyl alcohol, or light stimulation on the ERG c-wave and on the standing potential of albino rabbit eyes," *Doc Ophthalmol*, vol. 60, no. 4, pp. 393–400, Oct. 1985.

[111] F. Yamamoto, J. Kiryu, and K. Hiroi, "Effects of iodate on intraretinal b and c waves of the cat electroretinogram," *Ophthalmologica*, vol. 206, no. 3, pp. 152–157, 1993.

[112] S. Sasaki, H. Yamashita, K. Yagi, Y. Iwaki, and M. Kimura, "Full-field ERGs obtained using a contact lens electrode with built-in high intensity white light-emitting diodes in beagle dogs can be applied to toxicological assessments," *Toxicol. Lett.*, vol. 166, no. 2, pp. 115–121, Oct. 2006.

[113] S. E. Nilsson, B. Knave, and H. E. Persson, "Changes in ultrastructure and function of the sheep pigment epithelium and retina induced by sodium iodate. II. Early effects," *Acta Ophthalmol (Copenh)*, vol. 55, no. 6, pp. 1007–1026, Dec. 1977.

[114] M. Tanaka, S. Machida, K. Ohtaka, Y. Tazawa, and J. Nitta, "Third-order neuronal responses contribute to shaping the negative electroretinogram in sodium iodate-treated rats," *Curr. Eye Res.*, vol. 30, no. 6, pp. 443–453, Jun. 2005.

[115] A. Mizota and E. Adachi-Usami, "Functional recovery of retina after sodium iodate injection in mice," *Vision Res.*, vol. 37, no. 14, pp. 1859–1865, Jul. 1997.

[116] W. S. Redfern, S. Storey, K. Tse, Q. Hussain, K. P. Maung, J.-P. Valentin, G. Ahmed, A. Bigley, D. Heathcote, and J. S. McKay, "Evaluation of a convenient method of assessing rodent visual function in safety pharmacology studies: Effects of sodium iodate on visual acuity and retinal morphology in albino and pigmented rats and mice," *Journal of Pharmacological and Toxicological Methods*, vol. 63, no. 1, pp. 102–114, Jan. 2011.

[117] V. Enzmann, B. W. Row, Y. Yamauchi, L. Kheirandish, D. Gozal, H. J. Kaplan, and M. A. McCall, "Behavioral and anatomical abnormalities in a sodium iodate-induced model of retinal pigment epithelium degeneration," *Exp. Eye Res.*, vol. 82, no. 3, pp. 441–448, Mar. 2006.

[118] L. Hosoda, E. Adachi-Usami, A. Mizota, T. Hanawa, and T. Kimura, “Early effects of sodium iodate injection on ERG in mice,” *Acta Ophthalmol (Copenh)*, vol. 71, no. 5, pp. 616–622, Oct. 1993.

[119] T. Kohno, T. Miki, K. Shiraki, and M. Matsushita, “Choriocapillary changes and hyperfluorescence on indocyanine green angiography,” *Graefes Arch. Clin. Exp. Ophthalmol.*, vol. 236, no. 2, pp. 122–131, Feb. 1998.

[120] B. Anstadt, N. P. Blair, M. Rusin, J. G. Cunha-Vaz, and M. O. Tso, “Alteration of the blood-retinal barrier by sodium iodate: kinetic vitreous fluorophotometry and horseradish peroxidase tracer studies,” *Exp. Eye Res.*, vol. 35, no. 6, pp. 653–662, Dec. 1982.

[121] H. A. Sen, B. A. Berkowitz, N. Ando, and E. de Juan Jr, “In vivo imaging of breakdown of the inner and outer blood-retinal barriers,” *Invest. Ophthalmol. Vis. Sci.*, vol. 33, no. 13, pp. 3507–3512, Dec. 1992.

[122] F. S. Ashburn Jr, A. R. Pilkerton, N. A. Rao, and G. E. Marak, “The effects of iodate and iodoacetate on the retinal adhesion,” *Invest. Ophthalmol. Vis. Sci.*, vol. 19, no. 12, pp. 1427–1432, Dec. 1980.

[123] M. V. Miceli, M. R. Liles, and D. A. Newsome, “Evaluation of oxidative processes in human pigment epithelial cells associated with retinal outer segment phagocytosis,” *Exp. Cell Res.*, vol. 214, no. 1, pp. 242–249, Sep. 1994.

[124] L. M. Franco, R. Zulliger, U. E. K. Wolf-Schnurrbusch, Y. Katagiri, H. J. Kaplan, S. Wolf, and V. Enzmann, “Decreased visual function after patchy loss of retinal pigment epithelium induced by low-dose sodium iodate,” *Invest. Ophthalmol. Vis. Sci.*, vol. 50, no. 8, pp. 4004–4010, Aug. 2009.

[125] G. E. Korte, V. Reppucci, and P. Henkind, “RPE destruction causes choriocapillary atrophy,” *Invest. Ophthalmol. Vis. Sci.*, vol. 25, no. 10, pp. 1135–1145, Oct. 1984.

[126] S. Okisaka and T. Kuwabara, “Selective destruction of the pigmented epithelium in the ciliary body of the eye,” *Science*, vol. 184, no. 4143, pp. 1298–1299, Jun. 1974.

[127] T. Kuwabara, Y. Ishikawa, and M. I. Kaiser-Kupfer, “Experimental model of gyrate atrophy in animals,” *Ophthalmology*, vol. 88, no. 4, pp. 331–335, Apr. 1981.

[128] G. E. Eldred, “Lipofuscin fluorophore inhibits lysosomal protein degradation and may cause early stages of macular degeneration,” *Gerontology*, vol. 41 Suppl 2, pp. 15–28, 1995.

[129] N. L. Mata, R. T. Tzekov, X. Liu, J. Weng, D. G. Birch, and G. H. Travis, “Delayed dark-adaptation and lipofuscin accumulation in abcr+/- mice: implications for involvement of ABCR in

age-related macular degeneration," *Invest. Ophthalmol. Vis. Sci.*, vol. 42, no. 8, pp. 1685–1690, Jul. 2001.

[130] M. A. Zarbin, "Age-related macular degeneration: review of pathogenesis," *Eur J Ophthalmol*, vol. 8, no. 4, pp. 199–206, Dec. 1998.

[131] K. Ohtaka, S. Machida, T. Ohzeki, M. Tanaka, D. Kurosaka, T. Masuda, and T. Ishii, "Protective effect of hepatocyte growth factor against degeneration of the retinal pigment epithelium and photoreceptor in sodium iodate-injected rats," *Curr. Eye Res.*, vol. 31, no. 4, pp. 347–355, Apr. 2006.

[132] W. Chen, M. Yu, Y. Wang, Y. Peng, X. Li, D. M.-K. Lam, X. Chen, and X. Liu, "Non-mitogenic human acidic fibroblast growth factor reduces retinal degeneration induced by sodium iodate," *J Ocul Pharmacol Ther*, vol. 25, no. 4, pp. 315–320, Aug. 2009.

[133] L. Gong, Q. Wu, B. Song, B. Lu, and Y. Zhang, "Differentiation of rat mesenchymal stem cells transplanted into the subretinal space of sodium iodate-injected rats," *Clin. Experiment. Ophthalmol.*, vol. 36, no. 7, pp. 666–671, Oct. 2008.

[134] S. Hariri, A. A. Moayed, A. Dracopoulos, C. Hyun, S. Boyd, and K. Bizheva, "Limiting factors to the OCT axial resolution for in-vivo imaging of human and rodent retina in the 1060 nm wavelength range," *Opt Express*, vol. 17, no. 26, pp. 24304–24316, Dec. 2009.

[135] A. Mishra, A. Wong, K. Bizheva, and D. A. Clausi, "Intra-retinal layer segmentation in optical coherence tomography images," *Opt Express*, vol. 17, no. 26, pp. 23719–23728, Dec. 2009.

[136] B. Povazay, K. Bizheva, B. Hermann, A. Unterhuber, H. Sattmann, A. Fercher, W. Drexler, C. Schubert, P. Ahnelt, M. Mei, R. Holzwarth, W. Wadsworth, J. Knight, and P. S. J. Russell, "Enhanced visualization of choroidal vessels using ultrahigh resolution ophthalmic OCT at 1050 nm," *Opt. Express*, vol. 11, no. 17, pp. 1980–1986, 2003.

[137] A. Unterhuber, B. Povazay, B. Hermann, H. Sattmann, A. Chavez-Pirson, and W. Drexler, "In vivo retinal optical coherence tomography at 1040 nm - enhanced penetration into the choroid," *Opt. Express*, vol. 13, no. 9, pp. 3252–3258, May 2005.

[138] E. C. Lee, J. F. de Boer, M. Mujat, H. Lim, and S. H. Yun, "In vivo optical frequency domain imaging of human retina and choroid," *Opt Express*, vol. 14, no. 10, pp. 4403–4411, May 2006.

[139] J. Zhang, Q. Wang, B. Rao, Z. Chen, and K. Hsu, "Swept laser source at 1 μm for Fourier domain optical coherence tomography," *Applied Physics Letters*, vol. 89, no. 7, pp. 073901–073901–3, Aug. 2006.

[140] Y. Yasuno, Y. Hong, S. Makita, M. Yamanari, M. Akiba, M. Miura, and T. Yatagai, “In vivo high-contrast imaging of deep posterior eye by 1-um swept source optical coherence tomography andscattering optical coherence angiography,” *Opt. Express*, vol. 15, no. 10, pp. 6121–6139, May 2007.

[141] R. Huber, D. C. Adler, V. J. Srinivasan, and J. G. Fujimoto, “Fourier domain mode locking at 1050 nm for ultra-high-speed optical coherence tomography of the human retina at 236,000 axial scans per second,” *Opt. Lett.*, vol. 32, no. 14, pp. 2049–2051, Jul. 2007.

[142] D. M. de Bruin, D. L. Burnes, J. Loewenstein, Y. Chen, S. Chang, T. C. Chen, D. D. Esmaili, and J. F. de Boer, “In vivo three-dimensional imaging of neovascular age-related macular degeneration using optical frequency domain imaging at 1050 nm,” *Invest. Ophthalmol. Vis. Sci.*, vol. 49, no. 10, pp. 4545–4552, Oct. 2008.

[143] Y. Yasuno, M. Miura, K. Kawana, S. Makita, M. Sato, F. Okamoto, M. Yamanari, T. Iwasaki, T. Yatagai, and T. Oshika, “Visualization of sub-retinal pigment epithelium morphologies of exudative macular diseases by high-penetration optical coherence tomography,” *Invest. Ophthalmol. Vis. Sci.*, vol. 50, no. 1, pp. 405–413, Jan. 2009.

[144] Y. Chen, D. L. Burnes, M. de Bruin, M. Mujat, and J. F. de Boer, “Three-dimensional pointwise comparison of human retinal optical property at 845 and 1060 nm using optical frequency domain imaging,” *J Biomed Opt*, vol. 14, no. 2, p. 024016, Apr. 2009.

[145] V. J. Srinivasan, M. Wojtkowski, J. G. Fujimoto, and J. S. Duker, “In vivo measurement of retinal physiology with high-speed ultrahigh-resolution optical coherence tomography,” *Opt. Lett.*, vol. 31, no. 15, pp. 2308–2310, 2006.

[146] X.-C. Yao, A. Yamauchi, B. Perry, and J. S. George, “Rapid optical coherence tomography and recording functional scattering changes from activated frog retina,” *Appl Opt*, vol. 44, no. 11, pp. 2019–2023, Apr. 2005.

[147] J. G. Fujimoto, M. E. Brezinski, G. J. Tearney, S. A. Boppart, B. Bouma, M. R. Hee, J. F. Southern, E. A. Swanson, and others, “Optical biopsy and imaging using optical coherence tomography,” *Nature medicine*, vol. 1, no. 9, pp. 970–972, 1995.

[148] A. F. Fercher, C. K. Hitzenberger, G. Kamp, and S. Y. El-Zaiat, “Measurement of intraocular distances by backscattering spectral interferometry,” *Optics Communications*, vol. 117, no. 1–2, pp. 43–48, May 1995.

[149] G. Häusler, “‘Coherence Radar’ and ‘Spectral Radar’—New Tools for Dermatological Diagnosis,” *Journal of Biomedical Optics*, vol. 3, no. 1, p. 21, Jan. 1998.

[150] B. Povazay, B. Hermann, V. Kaji?, B. Hofer, and W. Drexler, “High Speed, Spectrometer Based Optical Coherence Tomography at 1050 nm for Isotropic 3-D OCT Imaging and Visualization of Retinal and Choroidal Vasculature,” in *Biomedical Optics*, 2008, p. BMB5.

[151] R. Tripathi, N. Nassif, J. S. Nelson, B. H. Park, and J. F. de Boer, “Spectral shaping for non-Gaussian source spectra in optical coherence tomography,” *Opt. Lett.*, vol. 27, no. 6, pp. 406–408, Mar. 2002.

[152] R. F. Spaide and C. A. Curcio, “Anatomical correlates to the bands seen in the outer retina by optical coherence tomography: literature review and model,” *Retina (Philadelphia, Pa.)*, vol. 31, no. 8, pp. 1609–1619, Sep. 2011.

[153] Y. Geng, K. P. Greenberg, R. Wolfe, D. C. Gray, J. J. Hunter, A. Dubra, J. G. Flannery, D. R. Williams, and J. Porter, “In Vivo Imaging of Microscopic Structures in the Rat Retina,” *IOVS*, vol. 50, no. 12, pp. 5872–5879, Dec. 2009.

[154] S. Hariri, A. A. Moayed, V. Choh, and K. Bizheva, “In vivo assessment of thickness and reflectivity in a rat outer retinal degeneration model with ultrahigh resolution optical coherence tomography,” *Invest. Ophthalmol. Vis. Sci.*, vol. 53, no. 4, pp. 1982–1989, Apr. 2012.

[155] M. Hammer, D. Schweitzer, E. Thamm, and A. Kolb, “Optical properties of ocular fundus tissues determined by optical coherence tomography,” *Optics Communications*, vol. 186, no. 1–3, pp. 149–153, Dec. 2000.

[156] H.-C. Cheng and Y.-C. Liu, “Simultaneous measurement of group refractive index and thickness of optical samples using optical coherence tomography,” *Appl. Opt.*, vol. 49, no. 5, pp. 790–797, Feb. 2010.

[157] P. Lee, W. Gao, and X. Zhang, “Performance of single-scattering model versus multiple-scattering model in the determination of optical properties of biological tissue with optical coherence tomography,” *Appl Opt*, vol. 49, no. 18, pp. 3538–3544, Jun. 2010.

[158] G. Farhat, A. Mariampillai, V. X. D. Yang, G. J. Czarnota, and M. C. Kolios, “Detecting apoptosis using dynamic light scattering with optical coherence tomography,” *J Biomed Opt*, vol. 16, no. 7, p. 070505, Jul. 2011.

[159] F. J. van der Meer, D. J. Faber, M. C. G. Aalders, A. A. Poot, I. Vermes, and T. G. van Leeuwen, “Apoptosis- and necrosis-induced changes in light attenuation measured by optical coherence tomography,” *Lasers Med Sci*, vol. 25, no. 2, pp. 259–267, Mar. 2010.

[160] J. Xu, L. L. Molday, R. S. Molday, and M. V. Sarunic, “In vivo imaging of the mouse model of X-linked juvenile retinoschisis with fourier domain optical coherence tomography,” *Invest. Ophthalmol. Vis. Sci.*, vol. 50, no. 6, pp. 2989–2993, Jun. 2009.

[161] A. A. Moayed, S. Hariri, C. Hyun, B. Doran, T. W. Kraft, S. Boyd, and K. Bizheva, “Combined optical coherence tomography and electroretinography system for in vivo simultaneous morphological and functional imaging of the rodent retina,” *J Biomed Opt*, vol. 15, no. 4, p. 040506, Aug. 2010.

[162] S. Hariri, M. C. Tam, D. Lee, D. Hileeto, A. Akhlagh Moayed, and K. Bizheva, “Noninvasive imaging of the early effect of sodium iodate toxicity in a rat model of outer retina degeneration with spectral domain optical coherence tomography,” *Journal of Biomedical Optics*, vol. 18, no. 2, Feb. 2013.

[163] R. Thar and M. Kühl, “Propagation of electromagnetic radiation in mitochondria?,” *J. Theor. Biol.*, vol. 230, no. 2, pp. 261–270, Sep. 2004.

[164] Johnsen and Widder, “The physical basis of transparency in biological tissue: ultrastructure and the minimization of light scattering,” *J. Theor. Biol.*, vol. 199, no. 2, pp. 181–198, Jul. 1999.

[165] A. Brunsting and P. F. Mullaney, “Differential Light Scattering from Spherical Mammalian Cells,” *Biophys J*, vol. 14, no. 6, pp. 439–453, Jun. 1974.

[166] V. V. Tuchin, “Tissue optics: light scattering methods and instruments for medical diagnosis,” 2007.

[167] S. Makita, T. Fabritius, and Y. Yasuno, “Full-range, high-speed, high-resolution 1-?m spectral-domain optical coherence tomography using BM-scan for volumetric imaging of the human posterior eye,” *Opt. Express*, vol. 16, no. 12, pp. 8406–8420, Jun. 2008.

[168] B. Povazay, B. Hermann, B. Hofer, V. Kajić, E. Simpson, T. Bridgford, and W. Drexler, “Wide-field optical coherence tomography of the choroid in vivo,” *Invest. Ophthalmol. Vis. Sci.*, vol. 50, no. 4, pp. 1856–1863, Apr. 2009.

[169] M. Esmaeelpour, B. Povazay, B. Hermann, B. Hofer, V. Kajic, K. Kapoor, N. J. L. Sheen, R. V. North, and W. Drexler, “Three-dimensional 1060-nm OCT: choroidal thickness maps in normal subjects and improved posterior segment visualization in cataract patients,” *Invest. Ophthalmol. Vis. Sci.*, vol. 51, no. 10, pp. 5260–5266, Oct. 2010.

[170] Y. Ikuno, K. Kawaguchi, T. Nouchi, and Y. Yasuno, “Choroidal Thickness in Healthy Japanese Subjects,” *IOVS*, vol. 51, no. 4, pp. 2173–2176, Apr. 2010.

[171] S. G. Warren, “Optical constants of ice from the ultraviolet to the microwave,” *Applied Optics*, vol. 23, no. 8, p. 1206, Apr. 1984.